CAPILLARY ABSORPTION AS AN AUDIBLE NOISE REDUCTION SCHEME FOR UHV TRANSMISSION LINES

by

David Woo-Sang Tong

B.S., University of Pennsylvania
(1968)

M.S., Massachusetts Institute of Technology
(1971)

E.E., Massachusetts Institute of Technology
(1972)

SUBMITTED IN PARTIAL FULFILLMENT OF THE

REQUIREMENTS FOR THE DEGREE OF

DOCTOR OF PHILOSOPHY

at the

MASSACHUSETTS INSTITUTE OF TECHNOLOGY

June, 1975

Signature of Author..
Department of Electrical Engineering & Computer Science, May 23, 1975

Certified by..
Thesis Supervisor

Accepted by..
Chairman, Departmental Committee on Graduate Students

CAPILLARY ABSORPTION AS AN AUDIBLE NOISE REDUCTION SCHEME FOR UHV TRANSMISSION LINES

by

David Woo-Sang Tong

Submitted to the Department of Electrical Engineering and Computer Science on May 23, 1975 in partial fulfillment of the requirements for the Degree of Doctor of Philosophy.

ABSTRACT

Audible noise generated from water drops collected on the transmission line conductor surface during foul weather is a major concern in UHV (ultrahigh voltage) transmission line design. Although the noise can be kept to an acceptable level by maintaining a surface electric gradient below 15 to 17 kV/cm, this alternative is quite costly since it would mean having larger conductor bundles and hence larger support towers as well. Several noise-reduction methods have previously been tried but none gave sufficiently satisfactory results.

A novel noise-reduction method is proposed in which capillary action is used to absorb the surface water drops into the field-free conductor interior. A high degree of surface wettability is a crucial ingredient in the absorption approach. Saturation places a theoretical limit to the effectiveness of this method during rain, but gravity-induced flow of the absorbed water helps to keep the conductor at an unsaturated state. Electrically shielded wicks can be placed at various points on the transmission line span to siphon off the draining water.

Fog and after-rain tests on several absorbent conductor designs demonstrated the effectiveness of the absorption scheme in reducing foul weather corona activity. Significant reduction in audible noise was achieved even at a surface electric gradient of 22 kV/cm. Degradation of surface wettability was found in the laboratory.

A quasi-one-dimensional model of viscosity-dominated, free surface flow is studied and laboratory experiments show that it is a useful representation of flow in an unsaturated conductor. It predicts that at the upper parts of the transmission line span, the flow tends to be uniform with a velocity linearly dependent on the conductor flow permeability and angle of incline. At the horizontal midsection, the flow is shown to be diffusional in nature and must be promoted via the use of wicks.

Optimization of conductor geometry with respect to permeability is desirable since it minimizes the number of wicks needed per span. Sample calculations show that a near optimal design will require 5 to 7 wicks per span to prevent saturation in a continuous light rain fall.

Thesis Supervisor: Gerald L. Wilson
Title: Associate Professor of Electrical Engineering

ACKNOWLEDGEMENTS

The author wishes to thank the following people:

Professor G.L. Wilson who supervised this thesis work and provided continual encouragement;

Professors J.R. Melcher and C.M. Cooke for their many helpful comments and suggestions;

Professor Inge Johansen for his cooperation during one of my most fruitful years of thesis research;

Mr. Joseph Cairns whose advice and help were invaluable in the making of the test conductors;

Messrs. Anthony Caloggero and Harold Atlas for their help in constructing experimental equipment;

Ms. Cha Mei Tang for our many useful discussions, for her assistance with the thesis preparations, and for putting up with me as her office mate;

Misses Barbara Smith and Susan Johnson for the professional tuping of this thesis;

Miss Jamie Eng who helped in drawing the illustrations;

members of the Electric Power Systems Engineering Laboratory who made life tolerable during moments of frustration.

This work was supported by American Electric Power Service Corp.

TABLE OF CONTENTS

Page

TITLE PAGE 1

ABSTRACT 2

ACKNOWLEDGEMENTS 4

TABLE OF CONTENTS 5

LIST OF FIGURES 9

LIST OF TABLES 13

GLOSSARY OF SYMBOLS 14

CHAPTER 1 THE STATE OF THE AUDIBLE NOISE PROBLEM 16

CHAPTER 2 THE MECHANISM OF AUDIBLE NOISE GENERATION ON HV TRANSMISSION LINES 22

- 2.1 Introduction 22
- 2.2 Drop Formation 22
  - 2.2.1 Surface Tension and Contact Angle 23
  - 2.2.2 Effect of Weather 26
- 2.3 Electrohydrodynamic Instability 27
- 2.4 Drop-Corona Interactions 29
  - 2.4.1 Zero Flow Rate 30
  - 2.4.2 Nonzero Flow Rate 39
- 2.5 Corona-Noise Transduction 41
- 2.6 Proposed Noise Reduction Methods and Other Possibilities 43
  - 2.6.1 Insulation 45
  - 2.6.2 dc Bias 46
  - 2.6.3 "Ultra-Corona" 46
  - 2.6.4 Control of Surface Wettability 47
  - 2.6.5 Geometry Options 48
  - 2.6.6 Capillary Absorption 49
  - 2.6.7 Other Possibilities 49

Page

CHAPTER 3 THE CAPILLARY ABSORPTION METHOD 51

3.1 The Basic Scheme 51
3.2 Capillary Absorption 51
3.3 Design of an Absorbent Conductor 53

3.3.1 Absorption Capability 53
3.3.2 Likelihood of Saturation 55
3.3.3 Drainage Efficiency 56

3.3.3.1 Random Porous Matrix 57
3.3.3.2 Regular Channel Structure 59
3.3.3.3 Wicking 63

CHAPTER 4 EXPERIMENTAL INVESTIGATIONS OF THE CAPILLARY ABSORPTION METHOD 64

4.1 Aims 64
4.2 Description of Test Setup 64
4.3 Early Experimental Designs 67
4.4 The Grooved Stranded Conductor 73
4.5 Summary of Test Results 83

CHAPTER 5 A QUASI-ONE-DIMENSIONAL FLOW MODEL OF THE ABSORBENT CONDUCTOR 86

5.1 General Discussion 86
5.2 Description of Model 88
5.3 An Alternative Approach 98
5.4 Theoretical Case Studies 98

5.4.1 Hydrostatic Limit 99

5.4.1.1 Uniform Flow 99
5.4.1.2 Steady State Drainage 99

5.4.1.2.1 $q'=0$; α Constant 100
5.4.1.2.2 $\alpha=0$, q' Constant 103

5.4.1.3 Transient Drainage 104

5.4.2 $\kappa \geq 1$ 106

Page

CHAPTER 6 EXPERIMENTAL CASE STUDIES OF FLOW IN A STRANDED BUNDLE 109

6.1 Aims 109
6.2 Experimental Setup 109
6.3 Measurement of Permeability 110
6.4 Gravity Flow 115
6.5 Wicking and Horizontal Drainage 128
6.6 Transient Drainage 130
6.7 Summary 136

CHAPTER 7 DESIGNING AN ABSORBENT CONDUCTOR 138

7.1 Design Considerations 138
7.2 Optimization of Conductor Geometry 138
7.3 Requirement on Transverse Permeability 143
7.4 Wick Design 144
7.5 Placement of Wicks 146
7.6 Evaluating Absorption Capability 148

CHAPTER 8 CONCLUSIONS AND SUGGESTIONS FOR FUTURE RESEARCH 150

APPENDIX A BEHAVIOR OF PENDENT DROPS OF LOW SURFACE TENSION UNDER ELECTRIC STRESS 153

A.1 Discussion 153
A.2 Experimental Setup 154
A.3 Drop Behavior as a Function of Surface Tension and Conductivity 154

A.3.1 Positive dc 154
A.3.2 Negative dc 156

A.4 Description of Jets 156

A.4.1 Positive Jet 156
A.4.2 Negative Jets 160

A.5 Formation of Jets at High Electric Gradients 160

Page

APPENDIX B CALCULATION OF FOG CONDENSATION RATES 163

B.1 Condensation by Droplet Settling 163
B.2 Droplet Impingement by Wind 164
B.3 Fog Droplet Collection by Electric Dipolar Attraction 165
B.4 Laboratory Measurements 168

APPENDIX C SURFACE TREATMENTS OF THE GROOVED CONDUCTOR 170

C.1 Electropolishing 170
C.2 Anodizing 170
C.3 Maintaining Surface Wettability 171

APPENDIX D REYNOLD'S NUMBER ESTIMATION FOR THE ABSORBENT CONDUCTOR 172

REFERENCES 174

BIOGRAPHICAL SKETCH 177

LIST OF FIGURES

		page
Fig. 2.1	Contact angle at a three phase boundary	25
Fig. 2.2	Illustration of contact angle hysteresis	25
Fig. 2.3	Shadowgraphs of pendent drops under electric stress	31
Fig. 2.4	Typical current waveforms from the positively stressed pendent drop	32
Fig. 2.5	Visual corona from the positively and the negatively stressed water drop	33
Fig. 2.6	a) Consecutive frames in high speed film of the tip portion of the positively stressed water drop (current trace superimposed)	35
	b) Scope current trace	
Fig. 2.7	Typical current waveforms from the negatively stressed pendent drop	36
Fig. 2.8	Consecutive frames in high speed film of the tip portion of the negatively stressed water drop	38
Fig. 2.9	Current waveforms of water drop under ac stress	40
Fig. 2.10	Conductor with insulating tubing	48
Fig. 3.1	A simple capillary tube	52
Fig. 3.2	Schematic of an unsaturated porous matrix	52
Fig. 3.3	A stranded bundle at successive stages of saturation	60
Fig. 3.4	Illustration of wicking	60
Fig. 4.1	Diagram of EPSEL test chamber	65
Fig. 4.2	Noise performance of wire-wound absorbent conductor	68
Fig. 4.3	Noise performance of porous conductor in fog and in rain	69
Fig. 4.4	Draining the porous conductor with a wick	70
Fig. 4.5	Noise performance of porous conductor after rain and after fog	71

page

Fig. 4.6 Cross-sectional view of stranded conductor 75

Fig. 4.7 Fogging test results (at EPSEL) of smooth conductor 76

Fig. 4.8 After-rain test results (at EPSEL) 77

Fig. 4.9 Noise performance of smooth vs. grooved conductors in fog (Ohio Brass) 80

Fig. 4.10 Noise spectrum of smooth vs. grooved conductors after 1 hr. 20 min. of fogging, test voltage: 160 kV 81

Fig. 4.11 Noise performance of smooth vs. grooved conductors in light rain (Ohio Brass), test voltage: 160 kV 82

Fig. 4.12 Comparison of visual corona from the smooth and the grooved conductors 84

Fig. 5.1 Discrete modeling of parallel flow channels 87

Fig. 5.2 Continuum model of an absorbent conductor 89

Fig. 5.3 A stranded bundle at an intermediate level of saturation 89

Fig. 5.4 Control volume (dotted box) for integration 93

Fig. 5.5 Possible flow patterns with or without liquid addition 93

Fig. 5.6 Diagram of drainage with nonzero angle of incline 101

Fig. 5.7 Profiles of uniform flow with a saturated end condition 102

Fig. 5.8 Horizontal drainage by wicking 101

Fig. 5.9 A hypothetical transient flow profile 101

Fig. 5.10 Calculated profiles showing the effect of varying K_x (q', $\alpha = 0$) 107

Fig. 6.1 Cross-sectional diagram of test bundle showing position of manometer 111

Fig. 6.2 Diagram of flow experiments 112

Fig. 6.3 Diagram of apparatus for permeability measurements 113

Fig. 6.4 Approximating the interstice as a cylindrical pore 116

page

Fig. 6.5 Profile of h_m for $\theta = 2°$ 118

Fig. 6.6 Profile of h_m for $\theta = 4°$ 119

Fig. 6.7 Profile of h_m for $\theta = 6°$ 120

Fig. 6.8 Profile of h_m for $\theta = 8°$ 121

Fig. 6.9 Graph of h_m of uniform flow vs. flow rate 123

Fig. 6.10 Graph of maximum flow rate vs. angle of incline 123

Fig. 6.11 Apparent hysteresis in the flow profile 124

Fig. 6.12 Theoretical profile near a wick (hydrostatic limit) 125

Fig. 6.13 A possible flow situation 127

Fig. 6.14 Diagram of air-liquid interface in nonuniform flow 127

Fig. 6.15 Diagram of a wick 127

Fig. 6.16 Dependence of h_m adjacent to wick on flow rate 131

Fig. 6.17 Drainage profile for L = 120cm 132

Fig. 6.18 Drainage profile for L = 60cm 132

Fig. 6.19 Drainage profile for L = 15cm 133

Fig. 6.20 Horizontal drainage rates 133

Fig. 6.21 Plot of $t_{1/2}$ vs. distance from upper end of bundle 135

Fig. 6.22 Dependence of drainage velocity on angle of incline 135

Fig. 7.1 Another absorbent conductor design 140

Fig. 7.2 Dependence of flow capacity on channel size 140

Fig. 7.3 Increasing the permeability with nonconcentric arrangement 140

Fig. 7.4 Diagram of flow in wicking 145

Fig. 7.5 Diagram of wick placement on transmission line span 147

Fig. A.1 Apparatus for observation of jet modes 155

Fig. A.2 Visual appearance of steady and unsteady jet modes (1% photoflo) 157

page

Fig. A.3 Dependence of pendent drop behavior on surface tension and conductivity 158

Fig. A.4 Three consecutive frames in high speed film of positive jet 159

Fig. A.5 a) Consecutive frames in high speed film of negative jet 161

b) Scope current trace

Fig. B.1 Electric dipolar attraction of fog droplets 166

Fig. B.2 Fog condensation by wind 166

Fig. B.3 Measured fog condensation rates in laboratory chamber 166

LIST OF TABLES

Table No.		Page
3.1	Permeability of Some Materials	58
6.1	Table of Measured Permeabilities (in cc-sec/gm)	114
7.1	Calculated Wick Spacing	149
B.1	Estimated Fog Collection Rates	168

Glossary of Commonly Used Symbols

A, A_c	cross-sectional area of conductor
A_w	contact area between wick and conductor
A_s	area of flow at saturation
E, E_s, E_r	electric field gradient
f	friction factor
g	gravity
h	height of liquid column, height of flow
h_m	height of liquid column in manometer (see Fig. 6.1)
h_o	height of conductor, height of flow structure
h_s	height of flow at saturation (may or may not be equal to h_o)
k	permeability
k_c	channel permeability (related to available flow area)
K	permeability (related to total cross-sectional area and includes liquid viscosity: $K = \frac{n_e k_c}{\mu}$)
n_e	pore volume ratio, pore area ratio
p	pressure
p_b	liquid pressure at the bottom of the flow structure
p_c	capillary pressure (determined by the curvature of meniscus)
p_o	atmospheric pressure
p^*	averaged pressure

Q	flow rate (in conductor)
q'	influx rate, condensation rate (cc/cm^2-sec)
Q'	influx rate, condensation rate (cc/cm-sec)
Q_{max}	flow rate when conductor is completely filled
Q_s	flow rate when conductor is saturated (Q_s may or may not equal Q_{max})
r_o, r_c	characteristic dimension of flow channel
R_c	radius of conductor
v, V_s, v_o, V_o	velocity
w, w_{eff}	width
α	$\sin\theta$
β	$\cos\theta$
γ	surface tension coefficient
θ	conductor (flow structure) angle of incline
ϕ	contact angle
ρ	density
ε_o	electric permittivity of air
μ	viscosity

CHAPTER 1

THE STATE OF THE AUDIBLE NOISE PROBLEM

Corona generated radio and television interference and power losses have continually been annoying problems associated with high voltage overhead transmission lines. The usual practice in designing the conductors has been to keep the maximum surface electric field strength below 70% of dry corona threshold. The advent of extra-high voltage (EHV) transmission systems (500 kV - 750 kV), resulted in efforts, for economic reasons, to minimize conductor sizes with the effect of increasing the maximum field so that it more nearly approaches the dry corona threshold. For example, American Electric Power's 765kV system is designed to have a maximum field strength at about 80% of threshold.(1) At these levels of field strength, corona-generated audible noise during periods of foul weather becomes increasingly significant compared to the other corona-associated problems. Complaints from people residing near UHV lines have grown into court cases. In view of the recently developing consciousness of environmental pollution, audible noise reduction is considered by system planners to be critical in the design of UHV transmission lines.

Two types of corona phenomena on transmission lines are distinguished. Fair weather corona is usually associated with attached foreign particles. So far, the electromagnetic and acoustic disturbance created by this type of corona has been insignificant compared with the accompanying power losses. Foul weather corona, on the other hand, is associated with water drops or forms of solid precipitation which adhere to the conductor surface and greatly intensify corona activity. Power losses in foul weather, though substantial, are not considered serious since wet weather occurs only during a small percentage of the time. The other corona-associated problems cause much more concern. On a subjective basis, audible noise is more annoying than radio or TV interference since it is readily detected by the human ear.

The introduction of EHV and later of UHV (ultra-high voltage) transmission systems focused a great deal of attention on acoustic noise generation during foul weather. The reported work can be classified into two categories. One is concerned with clarifying the basic mechanism of noise generation and has the goal of finding noise reduction methods that are more economical than existing means. The other is concerned mainly with the empirical study of noise generation with emphasis placed on the characterization of the noise and its psychological effects. Much of the reported work in this latter category deals with measuring the dependence of noise on various system parameters including weather conditions, applied voltage, conductor bundle and subconductor (one of the conductors in a multiconductor bundle) sizes. The goal of these empirical studies is to establish design criteria using known techniques; e.g., manipulation of conductor geometry.

Early research work on audible noise focused on the behavior of the water drops and the associated corona characteristics. In 1964, Tsunoda and Arai(2) and later Akazaki(3) made experimental studies of corona from single water sites. In their experiments, water was dripped periodically onto an energized cylindrical conductor. Measurement of the current wave forms revealed that the corona modes were positive streamer pulses(4) for positive imposed voltage and Trichel pulses(4) for negative imposed voltage. Two types of noise, described as crackling and hissing, were detected depending respectively on whether the drop was emitting water or not.

About the same time Boulet and Jakubczyk(5) also studied this problem. The same kinds of corona waveform were recorded. Although the investigators recognized that the water drops caused local field intensification, they did not delve into the details of the process. Wettability of the conductor surface was also recognized as having an effect. An attempt was made to eliminate the surface drops by using a nonwetting surface, but no improvement was found.

Research on audible noise dwindled during the late 1960's until further interest was revived with the introduction of UHV transmission at about the turn of the decade. In the United States, a group of audible noise related papers appeared in which American Electric Power and Westinghouse(6,7) and Project UHV of General Electric(8,9) were the primary contributors. Much of this research concentrated on developing the ability to predict the noise performance of a given conductor configuration. The same kind of work was pursued in Canada(10) as well as in Europe(11) where UHV transmission was also anticipated.

At the Massachusetts Institute of Technology effort was continued toward developing further understanding of audible noise generation. Hoburg and Melcher(12) studied the electrohydrodynamics of a single pendent drop with applied voltage and flow rate as controlled parameters. They found that the drop behavior could be classified into three distinct modes characterized by the drop motions and by the attendant corona. This work represents the first time that flow rate was recognized as a significant factor in noise generation.

At our laboratory, the Electric Power Systems Engineering Laboratory of M.I.T., the noise spectra of single corona sites and corona-to-noise transduction mechanisms were investigated. With the very regular corona pulse patterns generated by metallic protrusions, a close correlation was found between the current pulse frequency and the noise spectral peaks(13). Noise spectra were measured for the various modes of behavior as described by Hoburg and Melcher. These were in general quite flat in the audible region above 1 kHz with positive corona noise noticeably higher than negative corona noise. Impulsive heating by streamers and field-induced space charge motions were investigated by Bosack(14) as noise transduction mechanisms. These appear to be respectively responsible for the high and low frequency parts of the noise spectrum as measured in the field.

Various noise reduction schemes were proposed and tested. The ones considered in this thesis exclude the simple but costly enlargement of the conductor sizes to reduce the surface electric gradient. These schemes can be categorized into several types which include insulation coverings, control of surface wettability, variation of conductor geometry, and the so-called "ultra-corona" method. Each of these met with various degrees of success while most introduce associated problems.

Without a suitable noise reduction method on hand, the power industry is preparing to accept, at least for the time being, the presence of corona as a necessary evil. Conductor bundle sizes are simply chosen to be large enough so that the audible noise is kept to an acceptable level. For the projected levels of 1500 kV, the constraint of noise performance may well be impossible to meet economically with sufficiently large conductor bundles. A low cost and effective noise reduction method may yet have critical bearing on the feasibility of UHV overhead transmission lines and would be an economizing means for lower voltage lines.

This thesis continues the effort to gain understanding of the noise generation process and develops a new reduction method. Although previous research has shed light on various aspects of the process, the total picture is not yet complete. For example, the very complex two-way interaction of water drop and corona still remain unclear. Also surface wettability has not been considered in more than very simple qualitative terms.

In Chapter 2, the process of foul weather audible noise generation is discussed at length. The overall process is broken down into distinct steps from the formation of surface drops to the actual generation of acoustic sound. An attempt is made to combine previously reported work as well as new information into a coherent overall picture. At the end of the chapter proposed noise reduction schemes are reviewed and their potential evaluated in light of the overall picture.

The theme of this thesis is presented in Chapter 3, where the idea of capillary absorption is discussed, first on general terms, and then more specifically as applied to audible noise reduction. The effectiveness of this method under various weather conditions is also considered.

Experimental evaluation of the capillary absorption method is described in Chapter 4. Results of tests on several absorbent conductor designs are presented, most of which were performed in the small test chamber at our laboratory using 6 ft. long conductors. A 24 ft. long conductor of one particular design was tested at the Ohio Brass indoor HV test facility. The results show that this method is quite effective in reducing noise even at very high surface electric gradients. Surface wettability is brought out as the single most important factor in the efficacy of this scheme.

An obvious limitation to the absorption method is the possibility of saturation. Estimates show that saturation can be reached even in light rain of average duration. Fortunately, flow is promoted inside the absorbent structure by the action of gravity, thus tending to maintain an unsaturated state. The water collected at the lower midspan region can be siphoned off using wicks which are electrostatically shielded. In order to understand quantitatively the internal flow and the wicking process, a theoretical flow model is developed in Chapter 5, and flow experiments are described in Chapter 6. Comparison of experimental and theoretical results show that the theoretical model is a useful representation of a capillary flow structure in the unsaturated state. In addition to predicting the flow capability of a given absorbent structure, the model also predicts the existence of a limit on wicking efficiency.

Using the material developed in the previous chapters, Chapter 7 illustrates the designing of a sample porous conductor having real transmission line dimensions. The conductor geometry is optimized with respect to absorbency and flow capacity; design considerations of the wick are discussed; and the positioning of wicks on the line is calculated for a light rain condition.

CHAPTER 2

THE MECHANISM OF AUDIBLE NOISE GENERATION ON HV TRANSMISSION LINES

2.1 Introduction

Water drops on the surface of high voltage conductors have long been known to affect corona production. As early as 1915 Peek(15) showed that the corona threshold of a conductor is lowered by the presence of moisture and included a correction factor in his well-known formula of corona onset. Since that time, the subject of electrically stressed water drops has been investigated in the disciplines of electrohydrodynamics and corona discharges. It is now possible to piece together a fairly complete picture of the foul weather audible noise generation.

The process begins with the formation of water drops on the surface of the conductor during foul weather. At a critical combination of drop size, shape, and surface electric gradient, the drop becomes unstable. The deformation of the drop grows rapidly and in such a way as to increase the field intensification. This leads, under atmospheric conditions, to localized corona and thus to the problems of radio and TV interference, audible noise, and power losses. The observed overall behavior of the water drop is the complex interaction between the drop surface and corona space charge via local electric field distortions. In the following sections, each step of the drop formation-instability-corona-noise process is discussed in detail.

2.2 Drop Formation

The first step in the process of foul weather corona generation has been given relatively little attention. Wettability is known to affect drop behavior and also noise generation. Water tends to spread out over an aged conductor surface and to collect as drops only at the bottom. In contrast, water tends to bead on a new conductor due to a thin film of lubricant from the manufacturing process. The lower noise levels recorded from aged conductors has been attributed to there being fewer corona sites. The wetting character of aged conductors prevails however only after prolonged exposure to a humid atmosphere or after thorough drenching in rain. Drop formation in fog has hardly been investigated and noise measurements in fog have been largely neglected because of the irreproducibility of the data.

In this section, the effect of wettability is discussed using surface chemistry concepts. Drop formation is shown to be dependent on both surface and weather conditions.

2.2.1 Surface Tension and Contact Angle

Surface tension is commonly known as a force per unit length associated with a surface dividing two homogeneous media. The analogy to a rubber membrane is often made. Unlike a rubber membrane, surface tension is not derived from elastic energy of the medium; rather it results from molecules at a surface experiencing a net attraction toward the interior. Thus surface tension is more correctly considered as an energy per unit area. For practical purposes the concept of force per unit length is easier to visualize and leads to correct results. Although effects of surface tension are most commonly observed on deformable liquid-gas interfaces, surface energy is also associated with solid-liquid and solid-gas interfaces.

When a drop comes in contact with a solid surface, a three phase boundary separating solid, liquid, and air results as shown in Fig. 2.1. The contact angle ϕ is a measure of the wettability of the liquid on the solid. A 0^{o} or 180^{o} contact angle indicates respectively perfect wettability or perfect nonwettability. The angle of 90^{o} roughly separates the wettable, or hydrophilic if water is involved, and the nonwettable, or hydrophobic, regimes. The Young-Dupre equation(16), derived from simple force balance,

$$\gamma_{sg}-\gamma_{sL}-\gamma_{Lg}\cos\phi = 0 \tag{2.1}$$

gives the relationship between ϕ and the surface tension coefficients which are in fact the surface forces per unit length.

Since surface tension involves only the top most layers of molecules at the surface, contamination can occur quite easily. A single layer of foreign molecules on the surface can drastically change the surface tension. For example, water on glass has a 0^{o} contact angle if the glass surface is carefully cleaned. The fact that one commonly observes water beading on glass is evidence of the ease of contamination.

In physical situations a complicating effect known as contact angle hysteresis is usually manifest to some degree; the apparent contact angle can assume any value within a finite range depending on the way the system arrived at the final configuration. This phenomenon is best illustrated by a drop resting on an inclined plane as shown in Fig. 2.2. On the lower side where the liquid is advancing onto dry surface, the contact angle is larger and is referred to as the advancing angle. On the upper side where the liquid is advancing onto wetted surface, the contact angle is referred

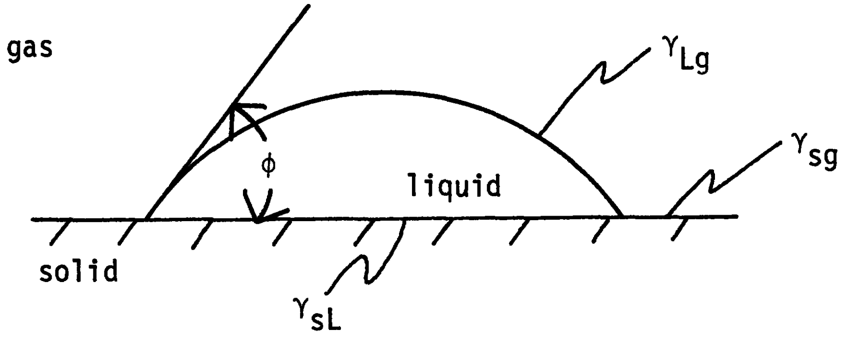

Fig. 2.1 Contact angle at a three phase boundary

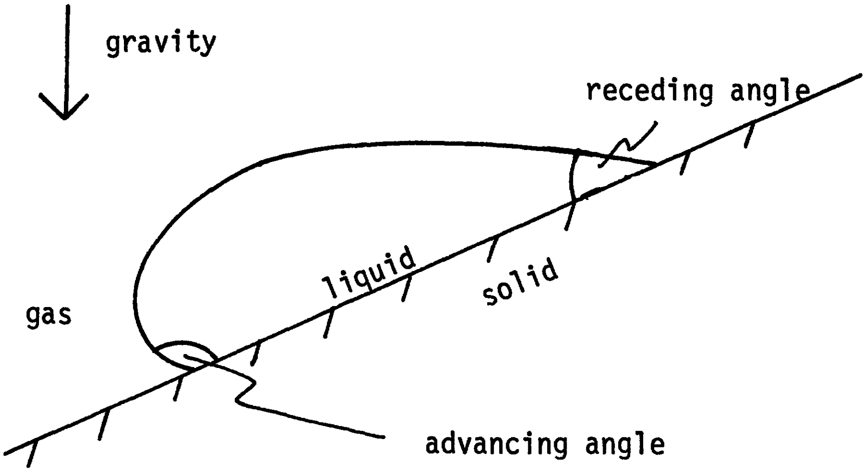

Fig. 2.2 Illustration of contact angle hysteresis

to as the receding angle. The difference in the two contact angles can easily be 40 or 50 degrees. Another example is paraffin and water; the contact angle differs significantly depending on whether the paraffin surface is initially dry or has been soaking in water for some time. Because of hysteresis, a discussion of wettability must include the history of the wetting process.

There are three possible explanations for the occurrence of hysteresis(16). First, contamination of the surface results in an apparent value of the surface tension. As the liquid moves over the solid, dissolution of the contaminant changes the apparent surface tension. Second, surface irregularity can cause apparent hysteresis even though, on the microscopic level, the true contact angle exists. An extreme example of this is the three phase boundary that occurs at an edge of the solid; the boundary behaves as if it is pinned there. Third, adsorption of liquid molecules on a solid-gas interface changes the surface tension there.

2.2.2 Effect of Weather

The hysteresis phenomenon can explain the differences in surface drop formation in fog versus rain. During fog, microscopic-sized water droplets impinge on the conductor surface by the action of wind, gravity, or electric dipolar attraction. Some percentage of the impinging droplets adhere to the surface and these conglomerate eventually into visible surface drops. The originally dry conductor surface is covered by randomly arranged wet and dry patches. The drops which occupy the wet regions grow and expand into the dry regions so that the observed contact angle is predominantly the advancing angle. The three phase boundary might be viewed as an energy barrier which prevents spreading even though the spread-out configuration may be energetically stable. Upon continued water condensation, the wet regions ultimately spread over all of the surface and the receding contact angle applies everywhere. If the receding angle is near zero, then a water film covers the entire surface. Of course if both the receding and the advancing angles are large, then the water continues to be concentrated as surface drops.

The situation in rain is somewhat different. When a rain drop impinges on the surface, there is sufficient mechanical energy to overcome the spreading barrier. Also, the rate of water deposition is greater than that in fog by orders of magnitude, and the entire surface can be very quickly wetted.

From this discussion, variability in fog tests is not too surprising. In addition to surface contamination and contact angle hysteresis, temperature gradients, fog parameters, and wind can all affect drop formation during fogging. In rain, all these effects are overwhelmed by the heavy flow rate. The much more consistent results for rain tests make them generally preferable over fog tests as a measure of noise performance of a given conductor geometry.

2.3 Electrohydrodynamic Instability

When a liquid surface is subjected to normal electric stress, the surface deforms in order to achieve force balance at the surface. Since the surface in general places a boundary condition on the electric field, its deformation leads in turn to a rearrangement of the field pattern. Thus the problem of determining the surface configuration involves strong coupling between the electric field and the surface geometry and is usually very difficult to solve analytically or even numerically.

Qualitatively, the general behavior of electrically stressed liquid surfaces is well established. For sufficiently low field gradients, the surface attains a stable configuration in which an exact balance exists between electric forces and mechanical forces, which include here the internal pressure and surface tension. As the applied electric field is increased, a well defined critical point can be reached when the equilibrium is no longer stable. The system configuration then undergoes continuous motion or settles at another equilibrium point.

As early as 1887 Lord Raleigh(17) calculated the critical charge that a free drop can support.

$$Q^2_{crit} = 16\pi\varepsilon\, r_0^3\gamma \quad \text{(mks)} \tag{2.2}$$

where ε is the permittivity of the surrounding medium, r_0 the drop radius, and γ the surface tension coefficient. This particular configuration is relatively simple to analyze because the equilibrium shape remains spherical up to the point of instability. Later, the stability problem of a free drop, either charged or uncharged, situated in a uniform electric field was investigated by Zeleny(18), Macky(19), Taylor(20), and others. This problem is analytically more difficult since the equilibrium shape changes with the applied field. Wilson and Taylor(21), experimenting with soap bubbles, and later Macky(19) with water drops showed that the critical electric field strength is given approximately by

$$E_{crit} = (485 \text{ volts/dyne}^{1/2})\sqrt{\gamma/r_0} \quad \text{(cgs)} \tag{2.3}$$

Thus the critical gradient for instability increases with decreasing drop radius.

Dudley(22) investigated the threshold of instability for pendent drops both theoretically and experimentally. He considered the 0^o and the 90^o contact angle cases under atmospheric pressure. His results showed that similar to Eq. (2.3) the threshold gradient increased with decreasing drop size. For both contact angles, the critical gradient for drops as small as 1 mm in height (as measured from the electrode surface to the drop tip at zero voltage) is about 15 kV/cm.

The concurrent appearance of corona with drop instability raises the question as to which one occurs first, corona or instability. Corona onset is known to be a strong function of ambient pressure(4), whereas instability is totally independent of it. Working with drops of radii 1 mm or less, English(23) and Dawson(24) showed that the voltage at which corona appeared was independent of the ambient pressure until the pressure was well below atmospheric. Also, in the pressure-independent range, this critical voltage was polarity-independent. Considering Eq. (2.3) there is little doubt that for the much larger pendent drops of interest, instability is the cause and corona appearance is the effect.

2.4 Drop-Corona Interactions

Existing high voltage transmission lines usually have a surface electric gradient exceeding 16 kV/cm which surpasses the critical gradient of instability of visible surface drops. What is observed then is the behavior of the drops beyond the initial instability. For pure water drops in atmospheric conditions, the deformation always leads to corona. The rate of water addition and the surface electric gradient are the most important factors affecting drop behavior; contact angle appears to have little effect after instability. In this section single pendent drops on a perfectly wetting surface are considered.

2.4.1 Zero Flow Rate

At instability, the drop either emits some water first or abruptly assumes a sharply pointed conical shape as shown in Fig. 2.3. This shape was reported numerous times in the literature(5,18). Intrigued by its common occurrence, Taylor(20) investigated the forces for an exact conical surface and found that, with gravity neglected, force balance is indeed possible, but only if the semivertical angle of the cone is 49.3°. The stability of the configuration as well as force balance at the singular tip remain unclear. For the pendent drop in air, the cone shape can be quite stable while corona issues from the tip. High speed movies of the tip region show that it is undergoing rapid oscillations (several hundred hertz) which correspond exactly with periodicities on the corona current waveform. The corona waveforms for the two polarities will be discussed separately.

a. Positive Polarity

The corona waveform is typically as shown in Fig. 2.4 where two distinct periods are apparent. Pulse groups occur with a period of about 2 msec while pulses of each group occur with a period of about .1 msec. The number of pulses in each group is at least two and increases with increasing voltage until the groups merge into continuous pulses. The fast rise time (on the order of 50 nsec) indicates the presence of streamer corona which is further substantiated by time explosure photos of the luminosity showing the characteristic bright thin core and diffuse envelope of streamers (see Fig. 2.5).

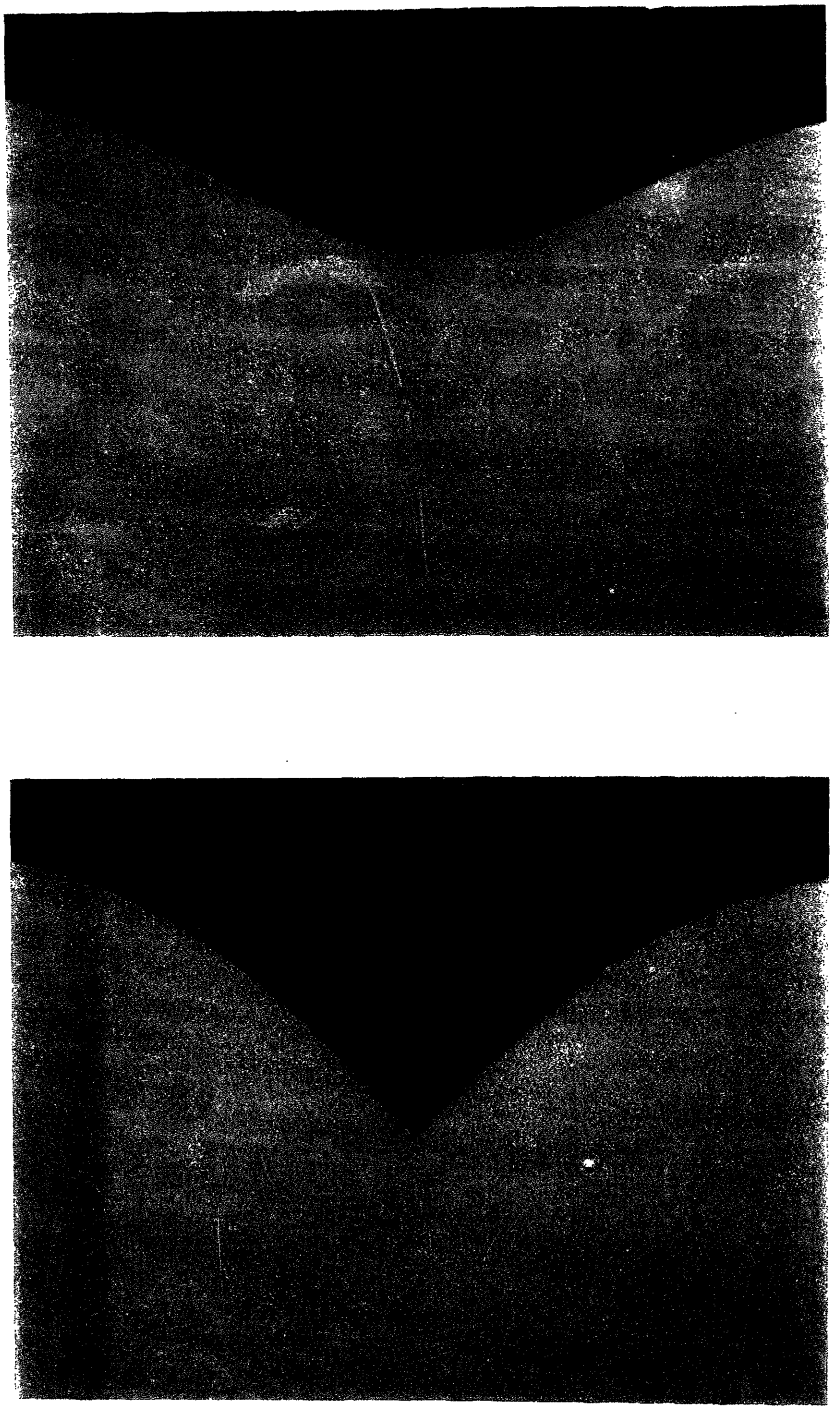

just before instability

after instability

Fig. 2.3 Shadowgraphs of pendent drops under electric stress

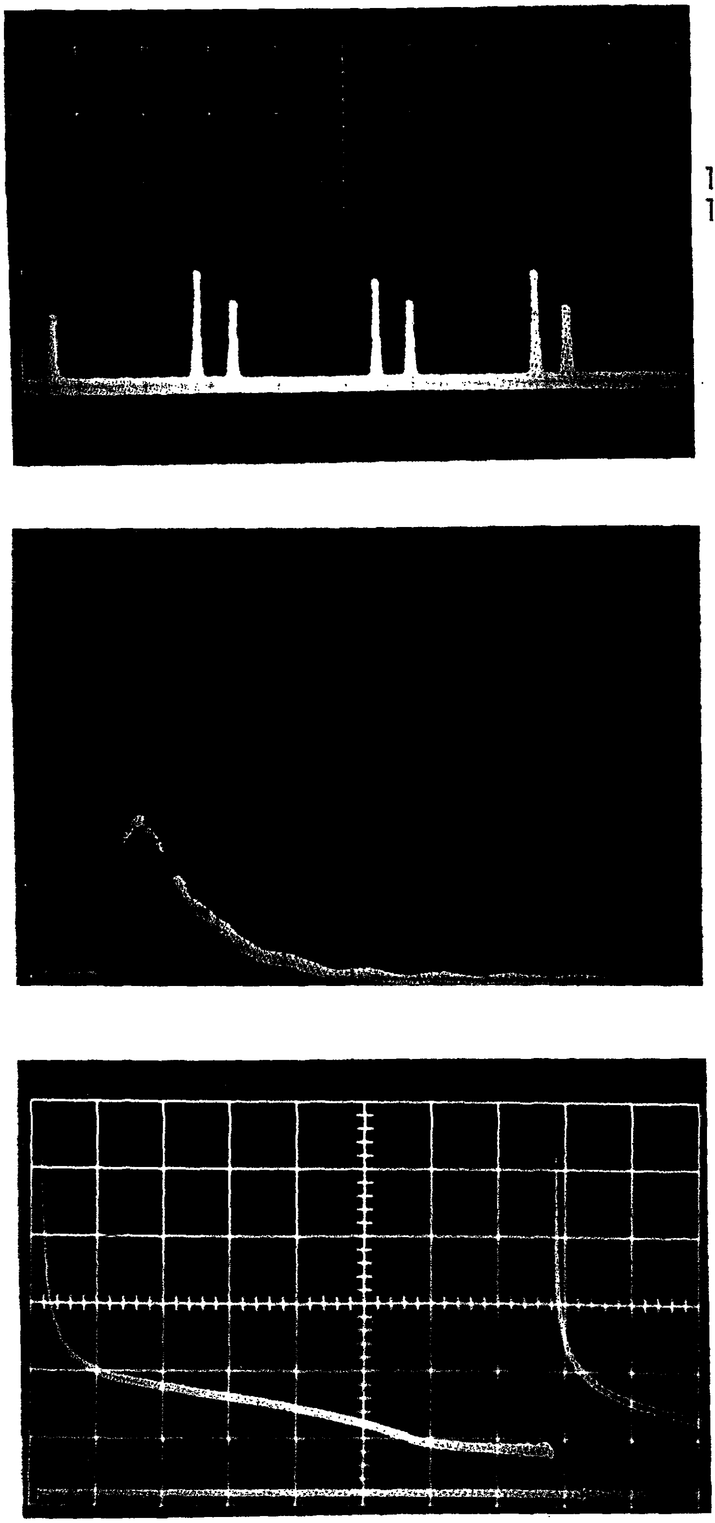

1msec/sq
10V/sq (10kΩ resistance)
(a)

.1μsec/sq
.5V/sq (100Ω series resistance)
(b)

50μsec/sq
.005V/sq (1kΩ series resistance)
(c)

Fig. 2.4 Typical current waveforms from the positively stressed pendent drop

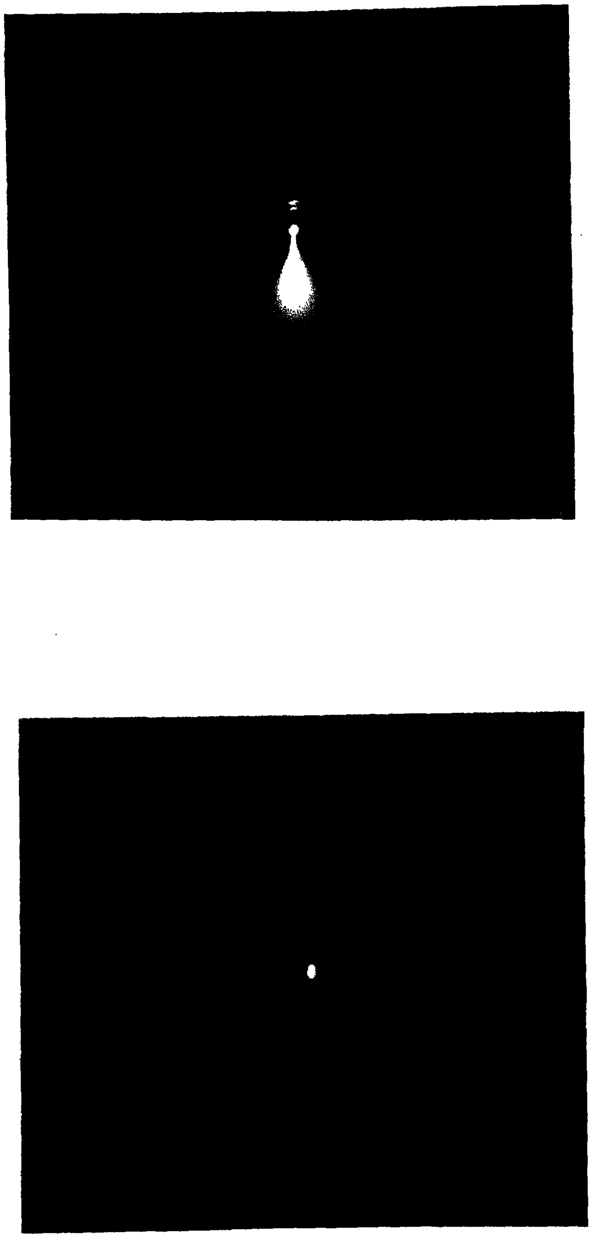

positive

negative

Fig. 2.5 Visual corona from the positively and the negatively stressed water drop

It is known that streamer frequency is governed by space charge clearing time(4). For an ion mobility in air of about 2.5 cm^2/V-sec, a 2 cm gap and an average field strength of 10 kV/cm, a clearing time can in fact be estimated on the order of .1 msec. The low amplitude tail following each pulse shown in Fig. 2.4c could be the result of drifting ions. The pulse waveform of Fig. 2.4.b is very similar in character to that measured by Akazaki(3) and Boulet and Jakubczyk(5) except for the difference in peak amplitudes which can be ascribed to the difference in surface gradients and electrode sizes.

Figure 2.6 shows a section of the high speed movie containing one oscillation of the drop tip region. The superimposed current trace moves from left to right for increasing current. A long decay time was introduced by the measurement circuit so that the current waveform is now as shown in Fig. 2.6b. Thus each jump in the current trace in the movie indicates that a streamer pulse has just taken place. During each cycle of oscillation, the drop tip sharpens under the influence of the electric field until the appearance of the first streamer. Then either from space charge shielding or from streamer generated pressure wave, the net surface stress reverses the tip motion. For a while as the tip recedes, conditions are still favorable for the formation of additional streamers. Finally all corona pulses cease; the electric stresses again predominate; and the entire process is repeated. It is noted that the first pulse of each cycle takes place, with little variation, when the tip reaches a certain degree of sharpness.

b. Negative Polarity

As Fig. 2.7 shows, the negative corona also consists of groups of

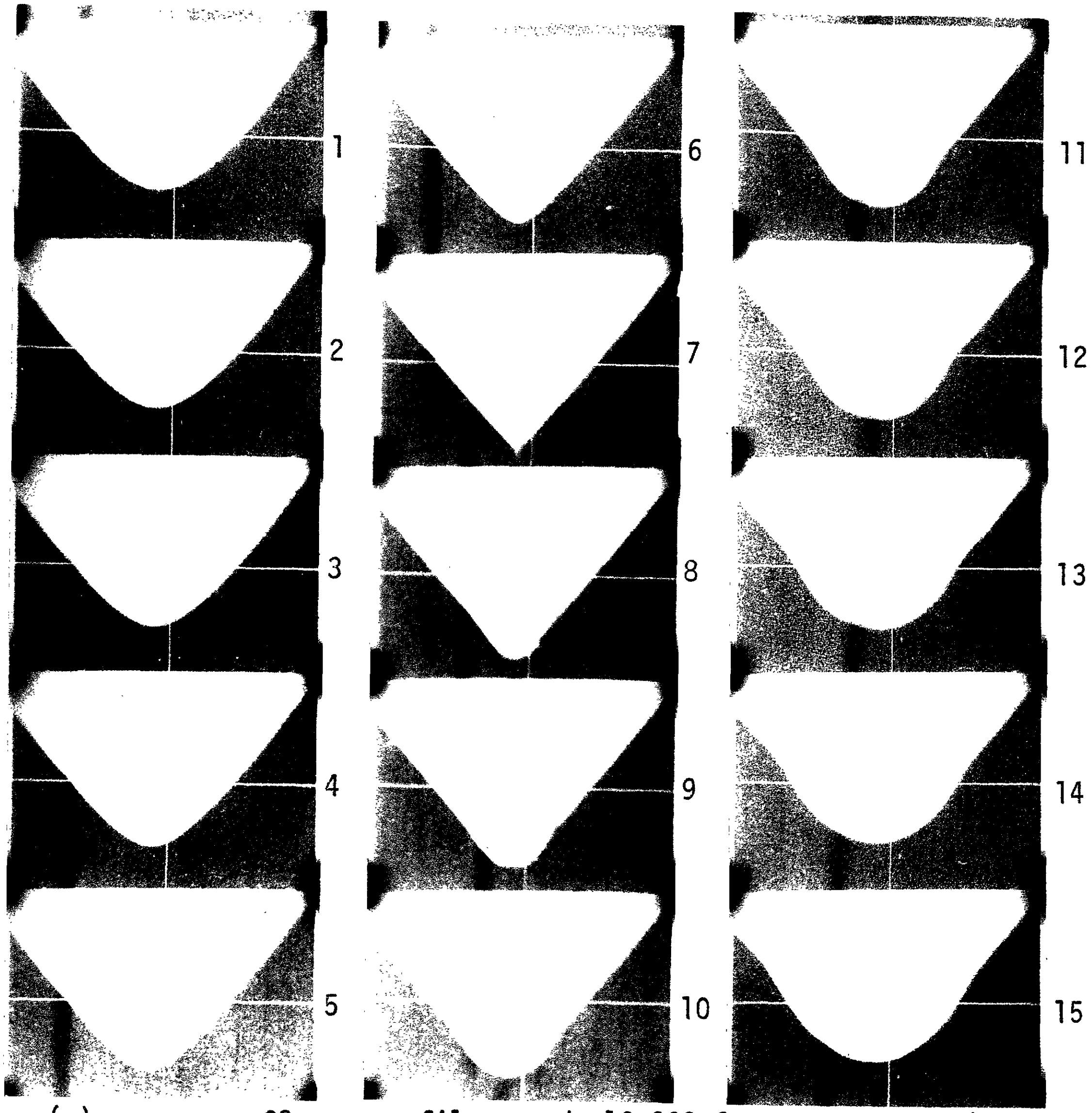

(a) mag.: 32x film speed: 10,000 frames per second

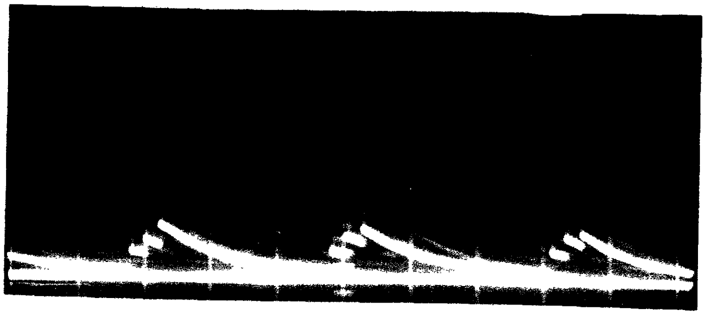

.5msec/sq

(b)

.1mA/sq

Fig. 2.6 a) Consecutive frames in high speed film of the tip portion of the positively stressed water drop (current trace superimposed)

b) Scope current trace

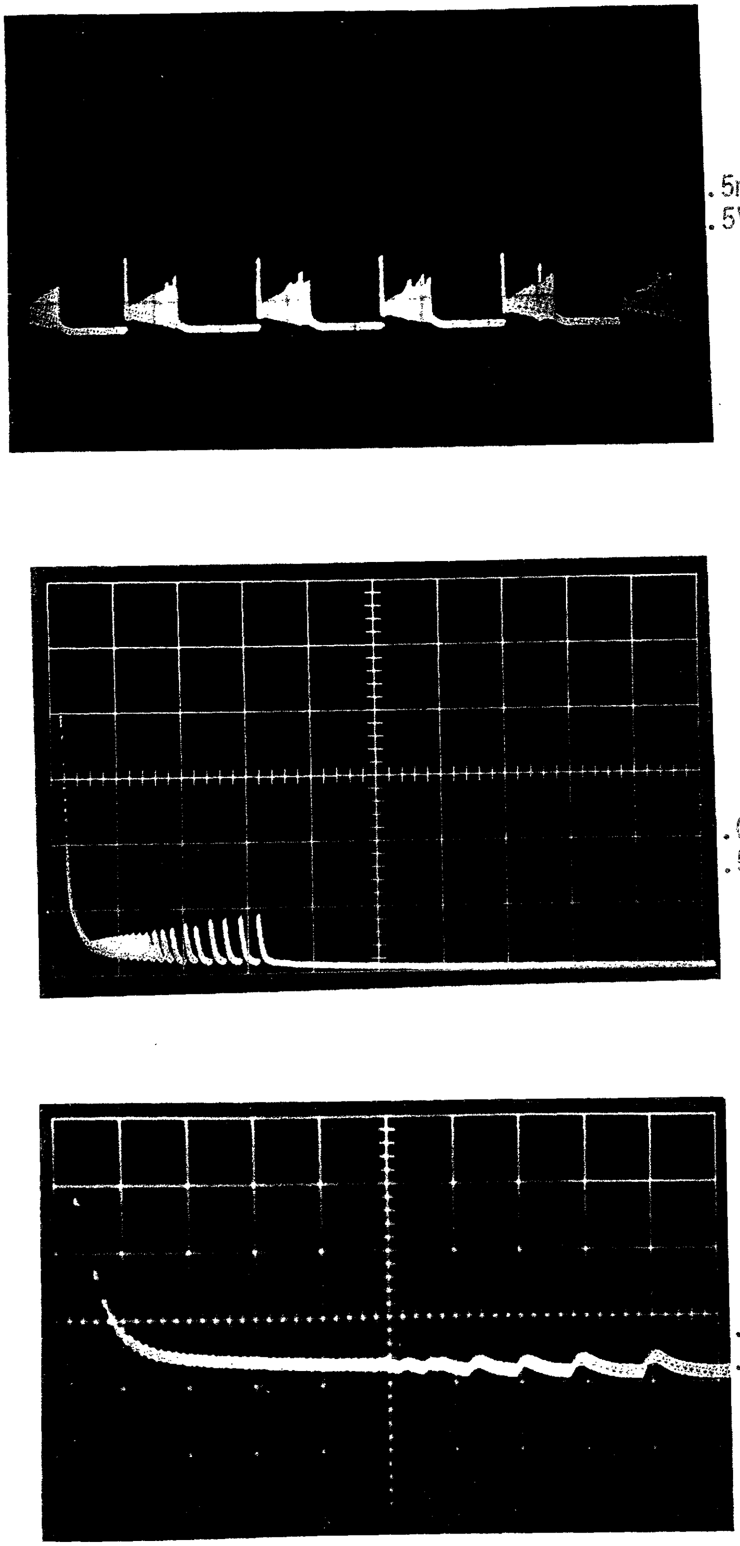

.5msec/sq
.5V/sq (10kΩ series
resistance)
(a)

.02msec/sq
.5V/sq (10kΩ series
resistance)
(b)

.1μsec/sq
.1V/sq (1kΩ series
resistance)
(c)

Fig. 2.7 Typical current waveforms from the negatively stressed pendent drop pulses which are similar in character to Trichel pulses. The period between groups is lower than that in the positive case by about an order of magnitude. Each pulse group begins with a large amplitude pulse, followed by lower amplitude pulses which increase in amplitude and decrease in frequency. Trichel pulses from a metallic electrode are known to increase in amplitude and decrease in frequency when the field strength is decreased. Accordingly, it may be deduced that the pulses are occurring as the drop tip is receding. The first pulse has the largest amplitude probably because it occurs without space charge inhibition.

As in the positive case, the number of pulses in each group increases with applied potential. However, the pulses never completely fill the entire period so that groups are always distinguishable.

A section from high speed movies taken of the magnified drop tip is shown in Fig. 2.8. Although the current trace is not included, there is little doubt that the current pulse groups are synchronized with the tip oscillations. This sequence of pictures shows no evidence of any water emission, in contrast to the observation of English(23) on a negatively stressed water point. English argued that since a water surface is unlikely to support negative corona, the corona he observed must be positive corona emanating from emitted droplets. The results here refute that argument.

c. AC Applied Voltage

The addition of a forced 120 Hz oscillation complicates the drop dynamics. A point of instability exists, similar to the dc cases, which in fact corresponds closely to the dc threshold if the rms value of the voltage is used(22). Beyond instability, sharpending of the point again

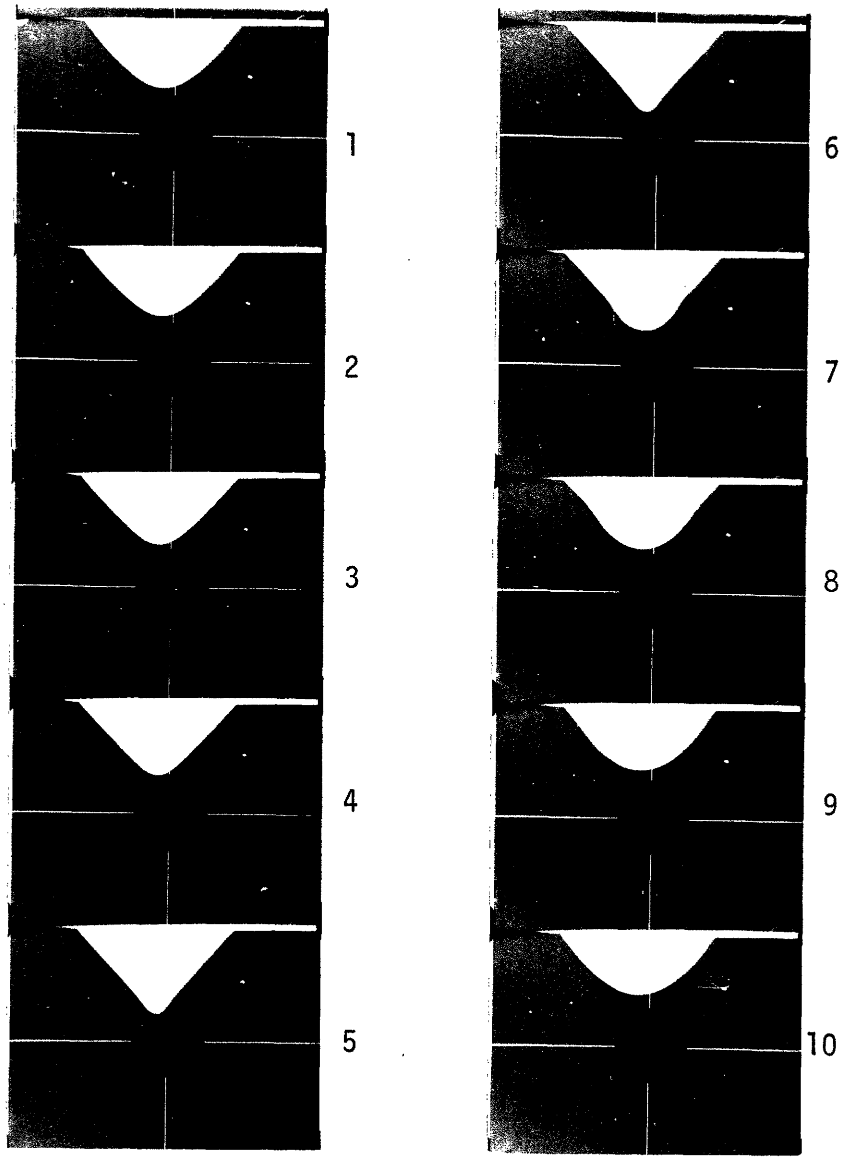

mag.: 32x
film speed: 10,000 frames per second

Fig. 2.8 Consecutive frames in high speed film of the tip portion of the negatively stressed water drop (see Fig. 2.7 for current trace) occurs, leading to positive streamer activity in the positive half cycle and to Trichel pulses in the negative half cycle. However, the regular pulse grouping of the dc cases is no longer present.

As shown in Fig. 2.9,a limited but distinct range of voltage exists in which only Trichel pulses are present without any observed positive streamer. This concurs with previous observations(13,25) that negative corona threshold is somewhat lower than the positive corona threshold for a fine point electrode in atmospheric pressure.

2.4.2 Nonzero Flow Rate

In a series of experiments where flow rate and voltage gradient were controlled, Hoburg and Melcher(12) observed that the drop behavior for both dc and ac excitation could be classified into three distinct modes. For low flow rates and gradients, mode I occurs where the drop periodically grows until disruption takes place. Some droplets are released each cycle with minor corona activity. In mode II, the regular drop disruption is replaced by a somewhat steady elongation of the drop with water emitting from the tip periodically at few tens of Hz. Much greater corona activity is present which produces a crackling noise. Current waveforms show that positive streamers and Trichel pulses are the corona modes present. Finally, for still higher flow rates and gradients, the drop tip elongates into a steady jet which terminates in a fine spray forming a conical pattern. Corona occurs at a short distance above the jet-spray transition point. The current is steady, thus indicating glow corona, with possibly some superimposed pulses, and the attendant noise is much lower than in mode II. For the range of voltage gradients tested (up to 16 kV/cm), the flow rate necessary to maintain mode III is greater than 10 cc/min which

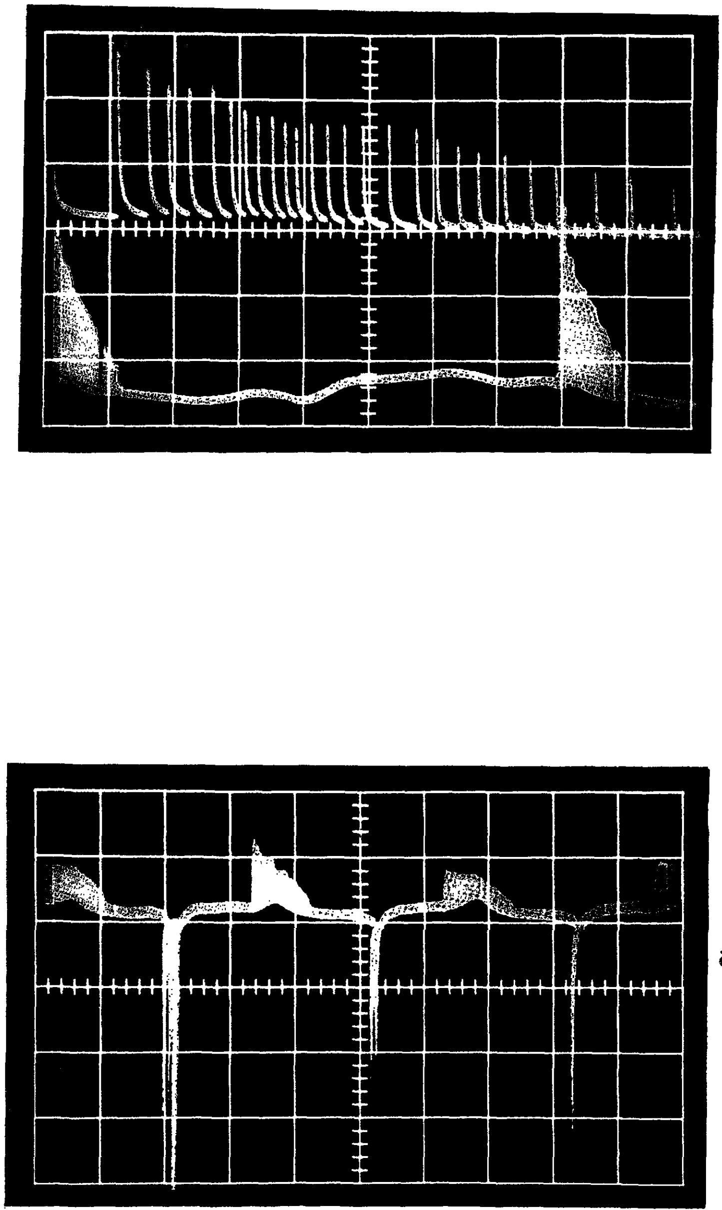

.07 ma/sq

.2ms/sq (upper trace)
2ms/sq (lower trace)

applied gradient:
22 kV/cm

(a)

.3ma/sq
5ms/sq

applied gradient:
33 kV/cm

(b)

Fig. 2.9 Current waveforms of water drop under ac stress
a) voltage just beyond onset (only Trichel pulses showing)
b) voltage far beyond onset

is very large compared with the flow rates encountered in most foul weather conditions.

These experiments may be compared with those by Akazaki(3), where water was dripped onto the conductor instead of being continuously fed. With the dripping scheme, the drop assumes more than one mode of behavior as water is periodically added and then depleted by emission. Mode III was not observed by Akazaki probably because the method used did not allow steady jet formation.

2.5 Corona-Noise Transduction

Having shown how corona comes about and the types of corona associated with the surface of water drops, we now consider the possible transduction mechanisms which convert electric energy into sound waves. These mechanisms account for several major characteristics of foul weather audible noise which are apparent from field and laboratory measurements (see for example, ref. (7)):

1) The noise spectrum includes a relatively flat (white noise) region above several hundred Hz, a pronounced peak at 120 Hz, and other peaks at the harmonic frequencies of 60 Hz (hum).
2) The amplitude of the noise increases with the surface electric gradient.
3) The amplitude of the noise increases with the size of the conductor for the same surface electric gradient. This is equivalent to having a higher applied voltage or a smaller value of $|\partial E/\partial r|$ at the surface.

Two likely mechanisms can be proposed. One involves the inhomogeneous heating of the air from energy dissipation and the other is the induced air movements by the motion of ions in the applied electric field. In any given situation, both of these mechanisms act simultaneously.

Ianna, et.al.(13), investigated the noise spectrum above 1 kHz from single corona sites. For both metallic protrusions and water drops, the acoustic energy was well spread out in the audible range. Metallic protrusions produced pulses with fairly steady frequencies and noise spectral peaks could be detected at these frequencies and their harmonics. In contrast, corona pulses from water drops were sufficiently randomized by the drop motion that the noise spectrum contained no significant peaking above 1 kHz. With either type of corona source, the noise amplitude increased with increasing applied voltage, positive corona noise being always much greater than negative corona noise. Based on these observations the following explanations can be made:

1) Noise increases with voltage since positive streamer amplitude and frequency increase with voltage.
2) Noise increases with conductor size for the same surface gradient since positive streamer amplitude also increases with conductor size. Experimental measurements employing metal electrodes showed that streamers can vary in amplitude from .3 mA for thin needles to 250 mA for a .8 cm diameter hemisphere(4).

From signal theory, a completely random train of pulses gives an exactly flat, white noise, spectrum even if the signal is modulated by a 60 Hz wave. Thus, based on randomly occurring corona pulses, the hum component in the transmission line noise spectrum cannot be explained. The ion drag mechanism, on the other hand, does offer an explanation. When there are many adjacent corona sites, their combined corona activity creates sheaths of ions in the vicinity of the conductor surface. The coordinated motion of the ion sheaths under the applied electric field sets up pressure waves which are detected as sound. Since ions of both polarities are generated, the dominant frequency component is 120 Hz. With the ion drag mechanism, the average generated space charge governs noise amplitude. Hence the smaller amplitude but higher frequency Trichel pulses could be equal in importance to the large amplitude, low frequency, positive streamers.

The complex nature of corona phenomena makes quantitative study of the noise generating mechanisms difficult. At our laboratory Bosack(14) tackled this problem with some limited success. He investigated theoretically and experimentally two simple cases, a single breakdown streamer site and a long thin conductor in essentially uniform ac corona, and showed that the impulsive heating mechanism is dominant in the former case and the ion drag mechanism in the latter case. However, before such a theory can be applied to predicting noise on actual transmission lines, more details on the overall corona activity must be known. In particular, quantitative knowledge of the surrounding ion cloud is totally lacking at present.

2.6 Proposed Noise Reduction Methods and Other Possibilities

The foregoing discussion points out that audible noise generation includes very complex processes that remain only superficially understood. Yet with the available information, we can still make an assessment, though perhaps qualitative, of the various proposed noise reduction methods and develop as yet untried avenues. An appreciation of the following requires first some quantitative knowledge about existing HV transmission line conditions and the associated noise.

In HV transmission line design, the primary constraint on conductor size is surface electric gradient; the dry corona threshold must not be exceeded. As the transmission voltage increase, conductor sizes must increase to meet this constraint. For voltages exceeding a few hundred kilovolts, each phase of the transmission line consists of a bundle of separate cables called subconductors, rather than a single conductor. For example, the existing 765 kV system of American Electric Power uses bundles of four 1.1" diameter ACSR conductors with a maximum surface gradient of 22 kV/cm.

Acoustic noise is measured in terms of the pressure of the generated sound wave. Because of the large range of variation in detectable sound pressure levels (SPL), the magnitude is usually expressed in logarithmic form.

$$\mathrm{SPL} = 20 \log(p/p_0) \qquad (2.4)$$

where p is the pressure amplitude of the sound wave; p_0 is a standard pressure of 2×10^{-5} N/m^2 (the threshold of hearing at 1 kHz); and the result is in units of decibels (db). The SPL of severe foul weather audible noise at 100 ft. from the transmission line is on the order of 60 to 70 db. In comparing noise performance of conductors, a difference of greater than 5 db is considered significant. However, other system parameters such as weather conditions, conductor size, and surface gradient must be considered as well since the SPL difference may depend strongly on them.

Although measurement of the entire audible spectrum is most informative about the character of the noise, quite often a simpler measurement is made of the sum of the various frequency components which are weighted in some fashion. In this way the noise is characterized by only one magnitude, making comparison of conductor noise performance much more straightforward. Standard weighting networks, designated A, B, or C(37), are available with the A-scale measurement being widely used in audible noise work since it closely resembles the response of the human ear.

On psychological terms, the nature of the noise is as important as its magnitude. The noise during fog or after rain is more annoying than that during rain because of the difference in ambient noise levels. Hum could be much more important than the higher frequency noise not only because of its psychological effects, but also because it attenuates less through air or other solid materials.

2.6.1 Insulation

A thin dielectric coating on the conductor has proved ineffective since the capacitive current alone is more than sufficient to sustain the corona current. Noise reduction does result if the insulating layer is thick enough to keep the drops in a region of substantially reduced gradient, but this is equivalent to enlarging the conductor.

Even for dc transmission systems, this scheme is questionable. Reduction of field gradient at the water drop surface can be accomplished only by increasing the voltage drop across the insulation layer. This results from the accumulation of surface charge which in turn results from some initial corona discharges. For example, suppose that an insulating layer 1mm thick is used to reduce the surface gradient of a 765 kV conductor by 5%. Then the layer must sustain a voltage difference of approximately 40 kV which is equivalent to 1 kV/mil. This value is comparable to the breakdown strength of most known insulating materials(38). In addition to the likelihood of breakdown, aging and heat dissipation problems may be severe with this approach.

2.6.2 dc Bias

Since positive streamers are known to be much noisier than Trichel pulses, the application of a negative dc bias voltage should reduce audible noise generation by the reduction of streamer activity. Some success was reported at GE's Project UHV using this approach.

Aside from the fact that implementation of this approach in the large scale is technically difficult, there are possible intrinsic limitations in its effectiveness. First, the accumulation of a negative space charge cloud, whose magnitude depends on the density of corona sites, tends to cancel the effect of the voltage bias. In heavy rain when the sites are numerous, no noise improvement was recorded.(39)

Second, although Trichel pulses contribute relatively little high frequency noise, they contribute heavily to the space charge sheath. Hence the hum component may not be reduced by this approach. Finally, increasing the negative peak gradient may bring on negative breakdown streamers. The investigators at Project UHV did find a critical value of the negative peak voltage above which the audible noise increased.(39)

2.6.3 "Ultra-Corona"

"Ultra-corona" was used initially to represent glow corona. Here it refers to the generation of relatively noise-free corona along the conductor so that the space charge produced would suppress the noisier corona modes. Boulet and Jakubczyk(5) were the first to try this method by wrapping around the conductor a 1mm diameter wire at an average pitch of 3cm. They found that both radio noise and corona losses increased. Implementing this method with regularly spaced points, Lecat(26) of Belgium maintained that with an optimized point geometry, a noise improvement of more than 10db was achieved in the frequency range above 1 kHz.

The power industry is rather skeptical of this method because of the continuous corona losses and other possible side effects such as ozone generation. If the ion drag mechanism is indeed important, then the continuously generated space charge would likely result in an unacceptable hum level in both fair and foul weather.

2.6.4 Control of Surface Wettability

Surfaces can be made to become more, or less, wettable. In reality there are few perfectly wetting surfaces (and these are easily subject to contamination, as discussed earlier), and no known perfectly nonwetting surface for water. Experiments have generally been made with surfaces that came as close as possible to the theoretical limits.

The number of corona sites are reduced on a wetting surface since drops spread into a film over most of the surface. This is the reason ascribed to the better noise performance of an aged conductor over a new conductor. The remaining water drops which hang from the bottom of the conductor limit the noise improvement to only a few db.

Boulet and Jakubczyk(5) tested the effect of a nonwetting coating; Paraffin (contact angle 105°) was the hydrophobic substance applied to the conductor surface. Negligible improvement resulted since a few small droplets remaining on the top of the conductor were in vigorous corona activity. The failure of this attempt is certainly not conclusive evidence that a perfectly nonwetting surface will not work. The problem is that no known material is nonwetting enough; even one of the best known nonwetting materials, Teflon (polytetrafluoroethylene), has a contact angle of only 108°. A material could conceivably be found with a sufficient degree of hydrophobicity, and if it successfully withstands aging, then this method could be technically quite feasible.

2.6.5 Geometry Options

Noise reduction is possible by designing the conductor bundles such that water drops tend to form away from the high surface gradient areas. This idea was pursued with some success by Comber and Zafanella(9) using multiconductor bundles. Based on the tendency of water drops to form only on the bottom of a wetting conductor, the bundle was designed asymmetrically such that the surface gradient at the bottom of each conductor is minimized. The reported noise improvmeent was on the order of 6 to 10 db for a maximum surface gradient of approximately 17 kV/cm.

A similar idea, also tested by Comber and Zafanella, is to place insulating tubing over the conductor as shown in Fig. 2.10. The diameter of the tubing is equal to the diameter of a normal conductor used for comparison. Provided drops do not form on the top and sides of the tubing, where the field is high, a noise reduction of several db results since the bottom drops experience a reduced gradient.

Both of these schemes depend critically on the near perfect wettability of the surface; otherwise drops would form all over the conductor surface.

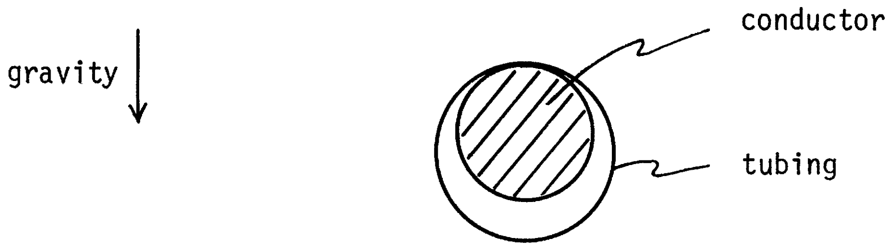

Figure 2.10 Conductor with Insulating Tubing

In the reported tests, the condition used was after-rain when the surface was already completely wetted. The requirement of wettability in fog would be much more stringent. Since some surface drops always remain, corona activity can be reduced only to a limited extent. In fact, the asymmetrical bundle test results showed no improvements at the surface gradient of 20 kV/cm.

2.6.6 Capillary Absorption

By absorbing the surface drops into the field-free interior of the conductor, corona and all the associated problems can be theoretically totally eliminated. Laboratory results have demonstrated the efficiency of this method in reducing noise. Practicality of the method has yet to be shown and the method depends critically on surface wettability which is at present insufficiently understood. The remainder of this thesis deals with the various aspects of the absorption method.

2.6.7 Other Possibilities

The methods presented above are ones that appear most practical and have all been tested experimentally. Heating and the use of surfactant coatings were two ideas considered but set aside in favor of the absorption method; their potential and practicality have not been thoroughly investigated.

The idea of heating is motivated by the field observation that a conductor carrying large currents exhibits less corona activity. This is expected since a surface with a higher temperature than the ambient is thermodynamically less favorable for water condensation and would promote a higher evaporation rate of collected moisture. In the laboratory, surface drops take noticeably longer to appear on a conductor heated to 50°C in a heavy fog. With reasonable heating levels, however, little effect is expected in rain. The power lost in heating the conductor would be prohibitively high unless heating currents can be controlled. Practicality and reliability of the control scheme is thus likely to determine the usefulness of this idea.

A surfactant coating which releases controlled amounts of a surface active substance, thereby lowering the surface tension of the collected water drops, could affect corona generation. This idea differs from the control of surface wettability in that the primary objective here is to lower γ_{Lg} (see Fig. 2.1). In general, when a solute is added to the water drop, it affects also γ_{sg} and hence wettability as well. Appendix A discusses the experimental observation that drops of low surface tension under electric stress tend to form jets. Besides having less acoustic noise, the jet mode also increases water emission rate. Unfortunately, with ac excitation, the forced 120 Hz motion of the drop interrupts the jet (unlike mode III of Hoburg and Melcher where the high flow rate is sufficient to maintain the jet even with ac excitation) and corona pulses remain with little reduction in noise. This method deserves further attention for HVDC transmission lines.

CHAPTER 3

THE CAPILLARY ABSORPTION METHOD

3.1 The Basic Scheme

Just as a sponge absorbs water, a conductor can also be made to do so. Since high voltage conductor size is more constrained by corona threshold than by current carrying capability, a reasonable percentage of the conductor volume can be used to store moisture. By absorbing the surface drops into the field-free conductor interior, the cause for foul weather corona is removed. Saturation, of course, places a limit on the absorbency. Fortunately, gravity can be used to effect drainage of the stored liquid, thus countering the effect of saturation to some extent. Before discussing how an absorbent conductor might be designed, the concept of absorption must first be understood.

3.2 Capillary Absorption

A curved liquid surface supports a pressure difference across the surface according to the Young-Laplace equation(16),

$$\Delta p = \gamma\left(\frac{1}{R_1} + \frac{1}{R_2}\right) \tag{3.1}$$

where γ is the liquid-air surface tension coefficient and R_1 and R_2 are the radii of curvature in two perpendicular directions at a given point on the surface. This effect forms the basis of capillary absorption and can be illustrated by a simple capillary tube. In Fig. 3.1, the pressure difference across the meniscus exactly balances the pressure head of the liquid column. If the meniscus is small, it can be approximated as part of a spherical surface of radius $R/\cos\phi$ where ϕ is the contact angle, and the following relationship applies.

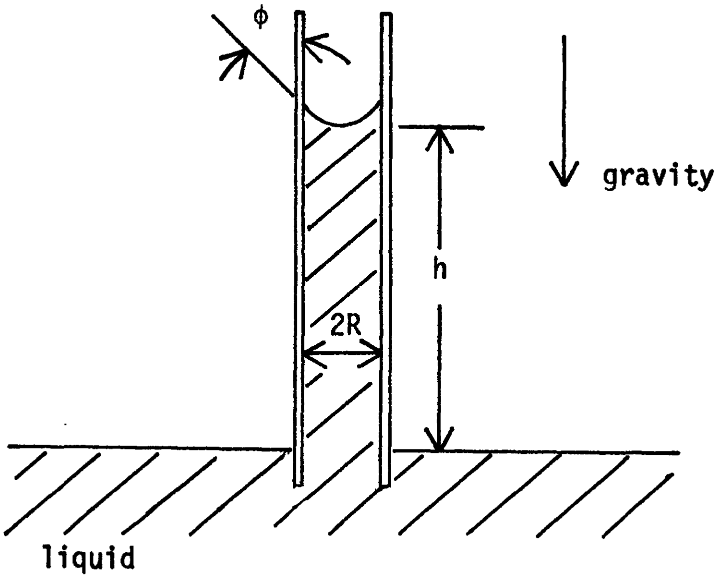

Fig. 3.1 A Simple Capillary Tube

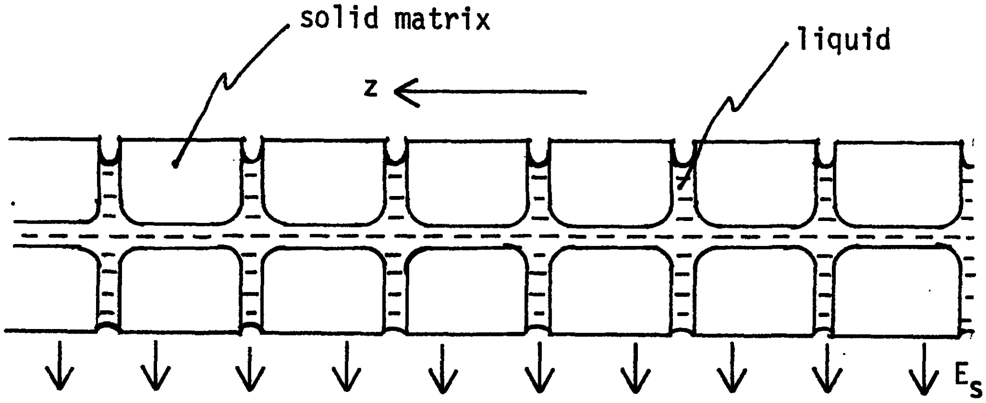

Fig. 3.2 Schematic of an Unsaturated Porous Matrix

$$\frac{2\gamma}{R} \cos \phi = \rho g h \tag{3.2}$$

Thus, the more wetting the walls are and the smaller the capillary diameter, the greater the liquid rise.

In a similar way, any structure that allows the formation of menisci will be able to absorb to a degree dependent on the curvature of the menisci formed. A simple example is any porous medium which is wetted by water. Although the absorption phenomenon is obscured in a porous medium by the random size and configuration of the pores and the presence of air spaces, the capillary tube analogy is in principle correct and is often used as an analytical model. In porous media literature the ability of the medium to absorb is often expressed in terms of a pore pressure(27), also variously represented as capillary pressure or suction pressure. Depending on whether the liquid wets the porous material, the pore pressure may be negative, with the medium tending to absorb the liquid, or positive, with the medium tending to exclude the liquid.

3.3 Design of an Absorbent Conductor

Several major questions need to be considered when capillary absorption is applied to HV conductor design. First, is it possible for the capillary forces to absorb all the surface drops by overcoming gravity and electric stresses? Second, can a large enough pore volume be made available such that saturation is not reached during most foul weather conditions? And third, if saturation is likely and gravity drainage must be facilitated to remove moisture, what kind of drainage efficiency can be expected?

3.3.1 Absorption Capability

Absorption capability can most simply be discussed by assuming that the absorbent conductor is perforated with vertical cylindrical pores. Equation (3.2) shows that absorbency can be increased by decreasing the pore size. Here the degree of absorbency is measured by the height of water rise in the porous matrix if its bottom surface is placed in contact with a reservoir. For example, if the pore walls were perfectly wetting, then from Eq. (3.1) with γ = 73 dynes/cm, a pore radius of .5mm is sufficient to support a water column 3cm in height and a conductor of that height will completely fill before saturation (saturation defined here as the point when the liquid pressure at the bottom becomes equal to the atmospheric pressure).

For any real solid porous matrix, its outer surface consists of pores leading into the interior as well as solid surface. Some water could conceivably remain on the solid portions instead of being absorbed through the pores and defeat the purpose of having absorption capability. Thus a sufficiently high density of surface pores is necessary.

For the transmission line problem capillarity is opposed by gravity and electric stresses. The relative magnitude of these forces can be estimated for a typical unsaturated condition as shown in Fig. 3.2. For generality, the vertical pores are shown to be interconnected by horizontal pores. With r_o = .5mm, h = 2cm, and E_s = 30 kV/cm (near the breakdown strength of air) and ignoring the possibility of instability for the moment, the important stresses can be estimated:

capillary pressure = $2\gamma/r_o$ = 3000 dynes/cm^2

gravitational head = ρgh = 2000 dynes/cm^2

electric stress = $\varepsilon_o E^2/2$ = 400 dynes/cm^2

Thus the capillary force has to contend mainly with gravitational pull and easily overwhelms the electric surface stress.

The existence of an instability of the liquid surface at the bottom porous matrix-air interface, similar to the Raleigh-Taylor instability in hydrodynamics, is certainly a possibility. At saturation, the liquid surface goes unstable due to the gravitational field alone. However, at low saturation levels, instability is not likely because of the stabilizing effect of the menisci formed at the lower surface. As shown in Fig. 3.2, the upper menisci have a fixed curvature as dictated by the contact angle so that the pressure of the liquid there is fixed, say at p_c. The lower menisci will assume whatever curvature is necessary so that the liquid pressure there is $p_c + \rho gh$. If $p_c + \rho gh$ is less than p_0, the atmospheric pressure, then the lower menisci are concave inward. Suppose the equilibrium state is disturbed so that some of the lower menisci reduce their curvatures. To satisfy conservation of mass, some neighboring menisci must correspondingly increase their curvatures. The resulting perturbation in the electric stresses will tend to increase the disturbance while the imbalance in pressure will tend to restore equilibrium. Because of the small pore size and the recessing of the liquid surface, the electric field perturbation at the liquid surface will be small compared to the pressure imbalance, and the system tends to be stable. Experiments described in the next chapter give conclusive evidence that for an unsaturated absorbent conductor, no such instability exists below dry corona threshold gradients.

3.3.2 Likelihood of Saturation

Evaluation of the possible storage volume requires some knowledge on the condensation rates during foul weather. For the following calculations, the conductor is assumed to have a radius of 1.5cm and a pore volume equal to 20% of the total conductor volume.

The condensation rate in rain can be easily calculated using rain fall data, assuming that all impinging drops get absorbed and neglecting evaporation. With a 3cm exposed surface width and a pore volume of 1.4cc/cm, saturation can be expected for rainfalls greater than .47cm or .18". Meterological data of the Boston area shows that this would occur for roughly 20% of the days in a year.

The condensation rate in fog is much more difficult to estimate because of the variability of many relevant factors and the sketchy fog data available. Three mechanisms of fog condensation are possible: 1) settling of fog droplets similar to the falling of rain drops; 2) impingement of fog droplets carried by wind; and 3) dipolar attraction of fog droplets by the action of the strong electric field. Appendix B calculates the possible condensation rates for these mechanisms and shows that in each case, the condensation rate is heavily dependent on fog droplet size. According to the calculations, saturation is not expected except in the worst cases; this conclusion is supported by field observations that visible surface droplets do not appear on conventional conductors until one to two hours after fog begins.

3.3.3 Drainage Efficiency

When saturation occurs, an absorbent conductor would not perform many better than a nonabsorbent one with a wetting surface unless there is some means of reducing the saturation level. The natural answer is gravity drainage since most of an overhead transmission line span has a nonzero angle of incline. Steady axial flow would result from a balance between the gravitational force and the viscous drag force, and the flow capacity would depend on the angle of incline and on the size of the axially directed pores. Since the angle of incline is fixed, only the pore size can be chosen to reduce the viscous drag force. This however cannot be done without lowering the absorbency. The conflicting requirements on absorbency and longitudinal flow drag mean that optimization of the absorbent structure geometry is possible.

So far the absorbent structure has been considered for generality on a conceptual level using straight cylindrical pores for illustration. To derive quantitative results two realistic geometries will be described which correspond to experimental models tested.

3.3.3.1 Random Porous Matrix

For this geometry, we are able to draw on the knowledge from flows in porous media (see for example ref. 27). The randomness of the matrix makes impossible an exact analytical treatment starting with the basic equations of fluid dynamics. Empirical laws and parameters are relied upon to describe the flow dynamics.

In porous media flows, pore pressure and volume flux are analogous to pressure and velocity in fluid dynamics and actually represent the latter in an average sense. The principal dynamical equation is Darcy's Law which relates the volume flux to the driving forces

$$\bar{q} = \frac{k}{\mu} \nabla(p + \rho g h) \qquad (3.3)$$

where $\bar{q}$ is the volume flux in cc/cm^2-sec, k the empirically determined permeability in cm^2, μ the viscosity in gm/cm-sec, and h the height in cm with reference to some fixed level. Permeability is thus a measure of the ease with which a fluid flows through a porous medium. The form of Darcy's Law is completely analogous to the Navier-Stokes Equation if in the latter the momentum term is neglected and the viscous term is assumed to be linearly dependent on velocity. These approximations of the Navier-Stokes Equation are valid for laminar, low Reynold's number flows.

Equation (3.3) can be used to estimate the drainage efficiency of a porous conductor. Recognizing that in this application there is no externally applied pressure gradient, we need to retain only the gravitational force in using Eq. (3.3). With the conductor lying at an angle θ with respect to the horizontal,

$$q_{axial} = k\rho g\ \alpha/\mu$$

where $\rho g\alpha = \rho g \sin\theta$ is the component of gravity in the longitudinal direction. It can be easily shown that for a transmission line span 1000' in length with a 30' sag in the middle, the angle of incline is 6° at the ends, decreasing nearly linearly to 0° at the middle. Thus α can be no larger than about .1.

The values shown in Table 3.1 are representative of the range of permeabilities of practical materials. In terms of the simple capillary model described above, permeability of a medium is not independent of its

Material	Permeability (cm^2)
agar-agar	$2.0\text{x}10^{-10}$ - $4.4\text{x}10^{-9}$
hair felt	$8.3\text{x}10^{-6}$ - $1.2\text{x}10^{-5}$
soils	$2.9\text{x}10^{-9}$ - $1.4\text{x}10^{-7}$
wire crimps	$3.8\text{x}10^{-5}$ - $1.0\text{x}10^{-4}$

Table 3.1

Permeability of Some Materials(28)

absorbency. Materials such as wire crimps with a large permeability will likely have a rather poor absorption capability. In our laboratory, the permeability of a glass fiber bundle was measured to be 3×10^{-6} cm^2. Using this value for k and .01gm/cm-sec for μ of water,

$$q = .03cc/cm^2\text{-sec}$$

Assuming that water is transported over 20% of the total cross-sectional area A of a 1.5 cm radius conductor, a maximum flow rate can be calculated:

$$Q_{max} = .2Aq = .04cc/sec$$

This rate is equivalent to the rate of water collected from about one meter of the conductor in heavy fog using the fog condensation rate calculated in Appendix B. With such a low drainage capacity, a porous conductor is expected to perform poorly in extended heavy fogging periods and to have long drainage times after rain.

3.3.3.2 Regular Channel Structure

The low permeability of porous materials results for three reasons. First, viscous drag forces are large in the relatively dense solid matrix. Second, on the microscopic level liquid elements follow tortuous paths as dictated by the random solid matrix. And third, as the material fills up with liquid, some air is bound to be trapped inside, thus reducing the effective flow cross section. These difficulties may be avoided to some extent by having uniform channels.

Figure 3.3 shows a regular channel structure consisting of a closely packed bundle of round rods with the interstices between the rods constituting the flow channels. This geometry closely resembles commonly used stranded conductors. Viscous drag, as described above, decreases with

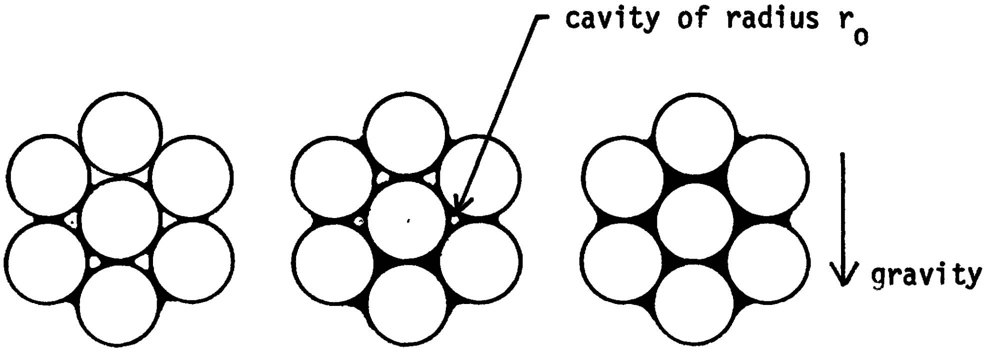

Fig. 3.3 A Stranded Bundle at Successive Stages of Saturation (dark areas denote liquid)

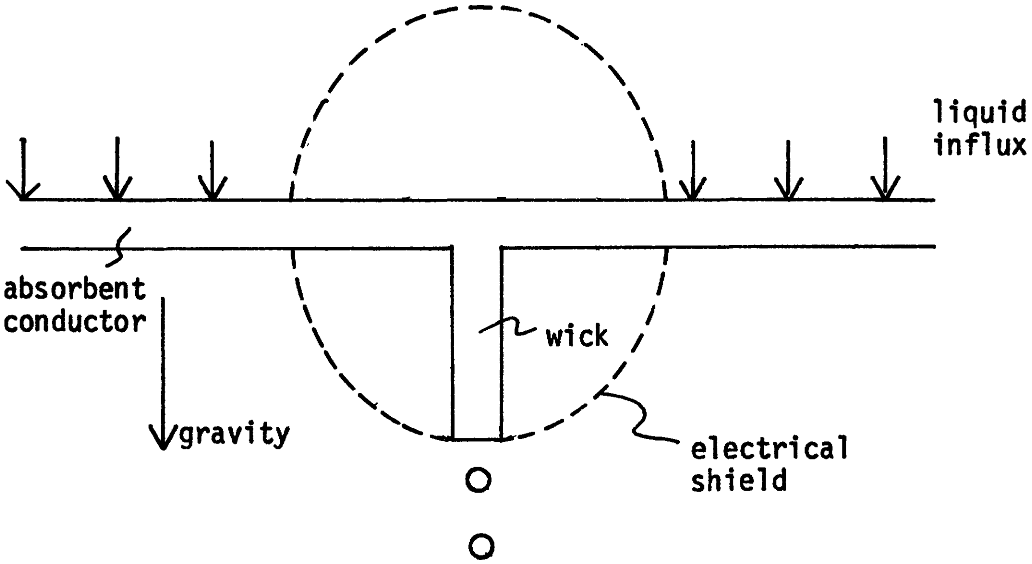

Fig. 3.4 Illustration of Wicking

increasing channel size but the absorbency requirement limits the maximum channel size.

According to the principle of capillarity, the absorbency of the stranded structure is due to the formation of menisci at the contact points of the strands. For a bundle of three or more strands, it is possible for adjacent menisci to join, thus reaching, in the interstices, the unstable situation of liquid containing empty cylindrical holes. The tendency of these holes to collapse and to pull in surrounding liquid leads to the apparent absorbency of this structure. Figure 3.3 illustrates this sequence. This process depends critically on the surface wettability, i.e., the liquid must be able to first form a continuous film around the surface of each strand. Otherwise, without liquid continuity and the resultant constraint on the hydrostatic pressure distribution, any liquid added will simply adhere to the outer structure surface as individual drops. Also,liquid movement from channel to channel must be allowed. As discussed in the next chapter, these requirements are met by cutting surface grooves on each rod.

If the absorption process is relatively slow, then at each stage of saturation the hydrostatic pressure distribution applies in the liquid and the curvatures of the menisci automatically satisfy the pressure jump between the liquid and air outside. The menisci at the higher elevations obviously will have a greater curvature since they must support the liquid below. The minimum curvature occurs just when the adjacent menisci join to form the cylindrical cavity of radius r_0. Depending on whether this minimum curvature can support the liquid column, the cavity may or may not collapse. Thus the relationship

$$\gamma/r_o = \rho g h_o \tag{3.4}$$

where h_o is the height of the structure, gives the maximum allowable size of the channel for the structure to be able to fill up with liquid by absorption. For $h_o = 3\text{cm}$,

$$r_o = .25\text{mm}$$

which is half of that derived with the simple capillary model since the radius of curvature in only one direction applies here.

The approximate permeability can be calculated by again using the rounded channel approximation. In the laminar flow regime (see Appendix D) simple Poiseuille flow applies(29) and the following relations can be easily derived

$$Q = \pi r_o^4 \rho g \alpha / 8\mu \tag{3.5}$$

$$k_c = \frac{Q\mu}{\rho g \alpha A_c} = \frac{r_o^2}{8} \tag{3.6}$$

where Q is the total flow for one channel with an angle of incline of $\theta = \sin^{-1}\alpha$, k_c the apparent permeability, A_c the channel area, and the other quantities as shown before, With $r_o = .25\text{mm}$,

$$k_c = 8 \times 10^{-5}\ \text{cm}^2$$

which is two orders of magnitude greater than that measured for the glass fiber bundle. For close-packed cylinders, the ratio of flow area to total cross-sectional area, n_e, is approximately .1, and the maximum possible flow rate for a bundle with radius $R_c = 1.5\text{cm}$ at a 6° angle of incline is

$$Q_{max} = (n_e \pi R_c^2)\ \frac{k_c}{\mu}\ \rho g \sin 6° = .6\text{cc/sec}$$

Comparison of the flow capability of the porous conductor and the stranded conductor shows clearly that drainage efficiency is much greater for macroscopic size channels, for which the permeability depends on the square of the channel size as illustrated by (3.6). The fact that the channels must fill up with water by capillarity places an upper limit on the channel size as given by (3.4). If the channels are too big, they fail to fill with water and the apparent permeability would fall to zero.

Chapter 6 shows that air entrapment is still a problem for this packed cylinder geometry, and in Chapter 7 another geometry is discussed which eliminates this problem.

3.3.3.3 Wicking

The liquid collected at the upper span sections will tend to accumulate at midspan where the angle of incline is zero, thus resulting in premature saturation there. Gravity can still be brought into play here to effect drainage with the use of wicks which furnish points of lower gravitational potential. Figure 3.4 illustrates the use of wicking. The wick is of course electrically shielded which also allows the water to drain out in a reduced gradient.

There is a limit to the capability of wicking which depends on the spacing between wicks and the parameters of the wick and the conductor. Even with the use of wicks saturation will still occur under certain foul weather conditions, but wicks do allow relatively quick drainage of the conductor at the end of the foul weather period. Wicking efficiency will be discussed further in section 6.3.2 and in Chapter 7.

CHAPTER 4

EXPERIMENTAL INVESTIGATIONS OF THE CAPILLARY ABSORPTION METHOD

4.1 Aims

The purpose of the following tests was to determine the validity of the no-drop-no-corona idea and the effectiveness of the capillary absorption method. Unlike other noise reduction methods, this one should theoretically suppress all corona if all surface drops are successfully absorbed. To establish the validity of this concept, comparative noise measurements were made between similar absorbent and nonabsorbent conductors.

It has been reported that the audible noise problem is worst during periods of fog and after rain when the ambient noise levels are low. Hence particular attention was paid to these two cases. For the absorbent conductors, the noise-level change with time-after-rain depended almost solely on the drainage rate. In after-rain tests, drainage was promoted either with a wick or with the test conductor hanging at an angle of incline comparable to that of a real line. These tests were intended only as a rough illustration of the drainage process, which is analyzed in detail in Chapter 5.

4.2 Description of Test Setup

Tests in our laboratory were done inside an acoustically shielded high voltage chamber. Figure 4.1 illustrates the layout of the chamber. Fog jets and a dripping device were installed to simulate fog and rain. High ac voltage was supplied by a 115V-115kV transformer to a 5' long cylindrical cage concentric with the test conductor which was at ground potential. For conductor sizes up to about 1" in diameter, this setup was capable of reaching dry corona threshold.

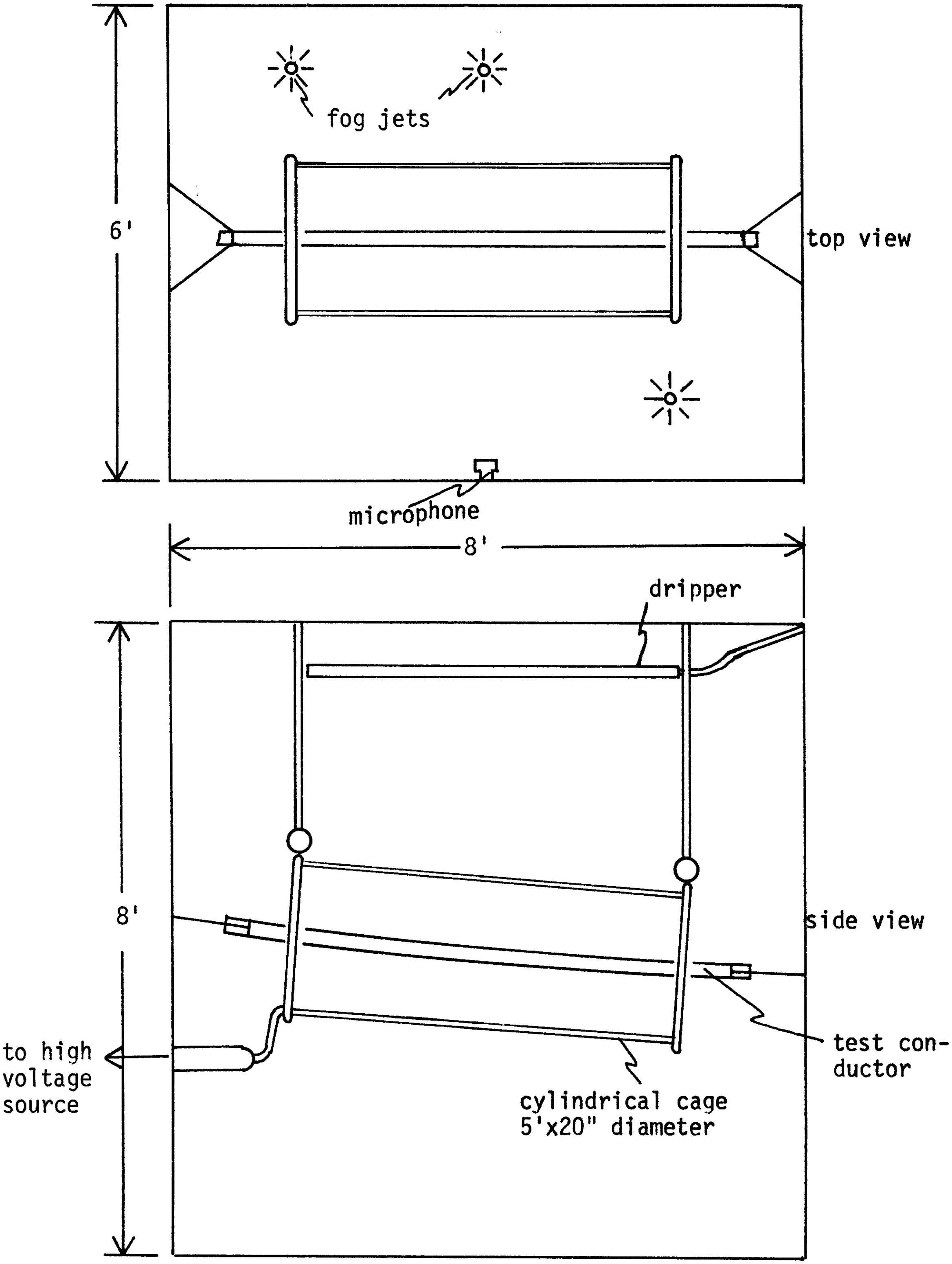

Fig. 4.1 Diagram of EPSEL Test Chamber

Noise measurements were made using a General Radio 1558-BP octave-band noise analyzer and a GR1560-P5 ceramic microphone with a GR1560-P40 preamplifier. The output of the octave-band analyzer was continuously displayed on a chart recorder.

The laboratory fog was considerably heavier than natural fog; this conclusion is based first on the rather low visibility of the fog (approx. 5'), and second on the fact that visible drops appeared on an energized nonabsorbent conductor only after about 15 minutes of fogging. In comparison, the corresponding time for droplet appearance in a natural fog is reported to be on the order of one to two hours. Our fogging tests lasted generally about one hour, by which time the noise level has long reached its peak. Noise measurements in fog were made periodically with the jets turned off.

The artificial rain-maker consisted of a hollow tube with small holes spaced 2" apart out of which water dripped onto the conductor below. The flow rate was not monitored since very few measurements were made during rain.

A common problem with fogging tests in high voltage chambers is the formation of drops on the high voltage feed-through wall. These drops can produce vigorous corona activity and often leads to flashover along the wall. To prevent this heat lamps were installed to keep the wall dry. Although as a result the chamber temperature rose during fogging tests, the effect on the results is expected to be small.

All of the several absorbent conductor designs tested showed significant reduction of noise in fogging tests. As expected, no improvement was detected for the heavy rain case where surface drops were present, but after rain the noise from the draining absorbent conductors invariably decreased significantly in a matter of a few minutes.

4.3 Early Experimental Designs

The first test conductor consisted of a 3/4" diameter brass tube covered with layers of water absorbent fiberglass. Fine copper wire (20 mils dia.) was closely wrapped on the outside to serve as a permeable electrical shield. Figure 4.2 compares the noise levels for the saturated and unsaturated cases in fog. Although the difference was sizable, even at the high gradient levels, the sharp increase of noise for the unsaturated case was rather unexpected. Close inspection revealed that even below saturation, surface droplets on the order of the wire diameter remained. These were surmised to be corona generators.

In an attempt to eliminate all surface droplets, the next conductor tested was a porous tubing 3/4" in diameter with 1/8" walls made of sintered stainless steel and having an average pore size of 10 microns. The wettability of the material was not known quantitatively, but positive absorbency was shown and was improved by the application of slight amounts of photoflo.

Figure 4.3 compares the noise performance in fog and rain of the porous conductor to that of a 3/4" diameter smooth brass tube which was made wetting by cleaning with solvent. No improvement in rain was recorded. The improvement in fog was appreciable, but again the noise curves merged rapidly near the dry corona threshold of the porous conductor.

A fiber glass wick was inserted along the length of the porous tube for drainage with an 8" section hanging down at the end as shown in Fig. 4.4. Figure 4.5a gives the noise levels after rain. For the porous conductor,

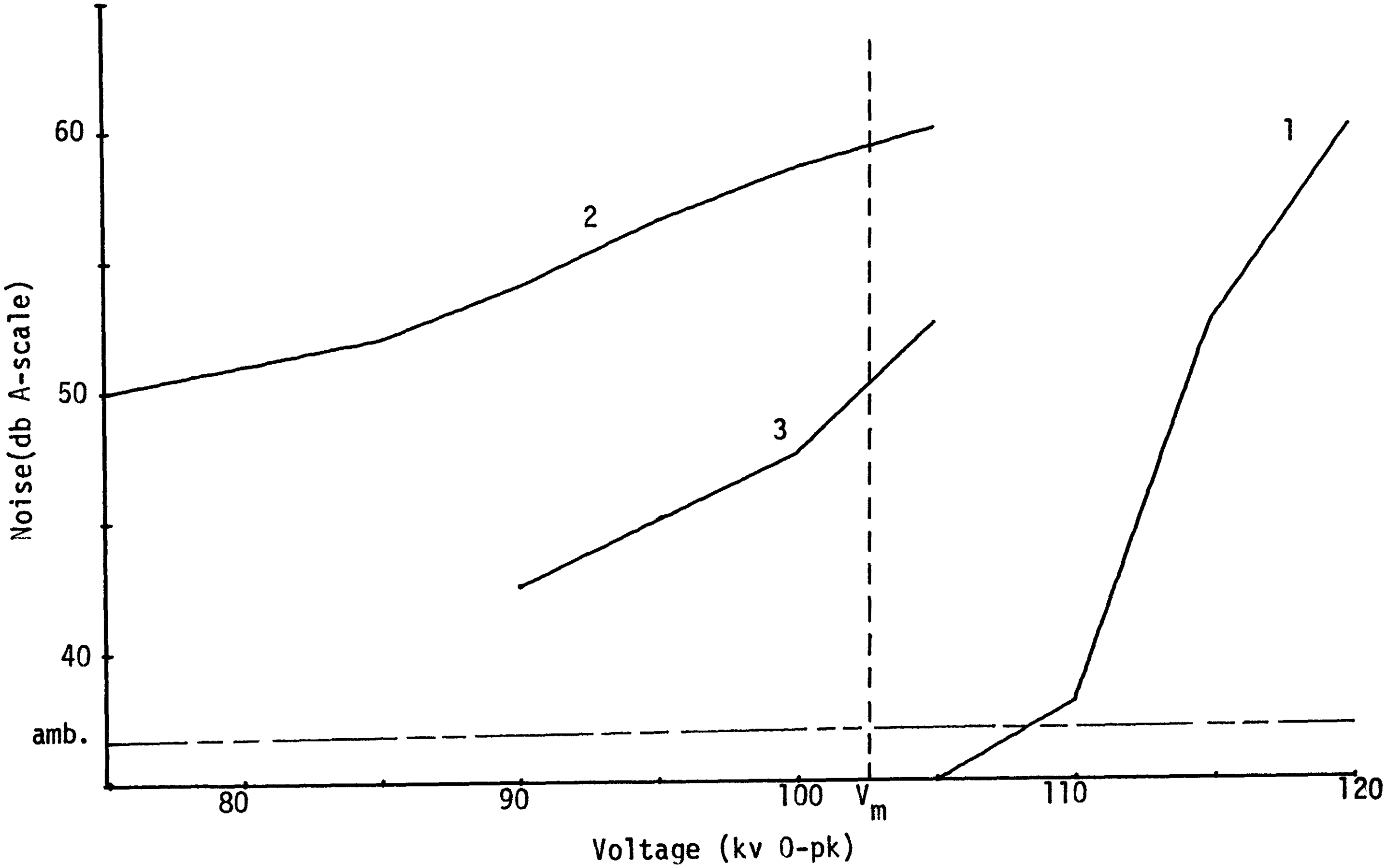

Fig. 4.2 Noise Performance of Wire-Wound Absorbent Conductor. Curve 1) Conductor Dry, Curve 2) Conductor Saturated with Pendent Drops Showing; Under Heavy Fog, Curve 3) Conductor Unsaturated; Under Heavy Fog. V_m = 80% of Dry Corona Threshold of a Smooth Surface Conductor of the Same Diameter

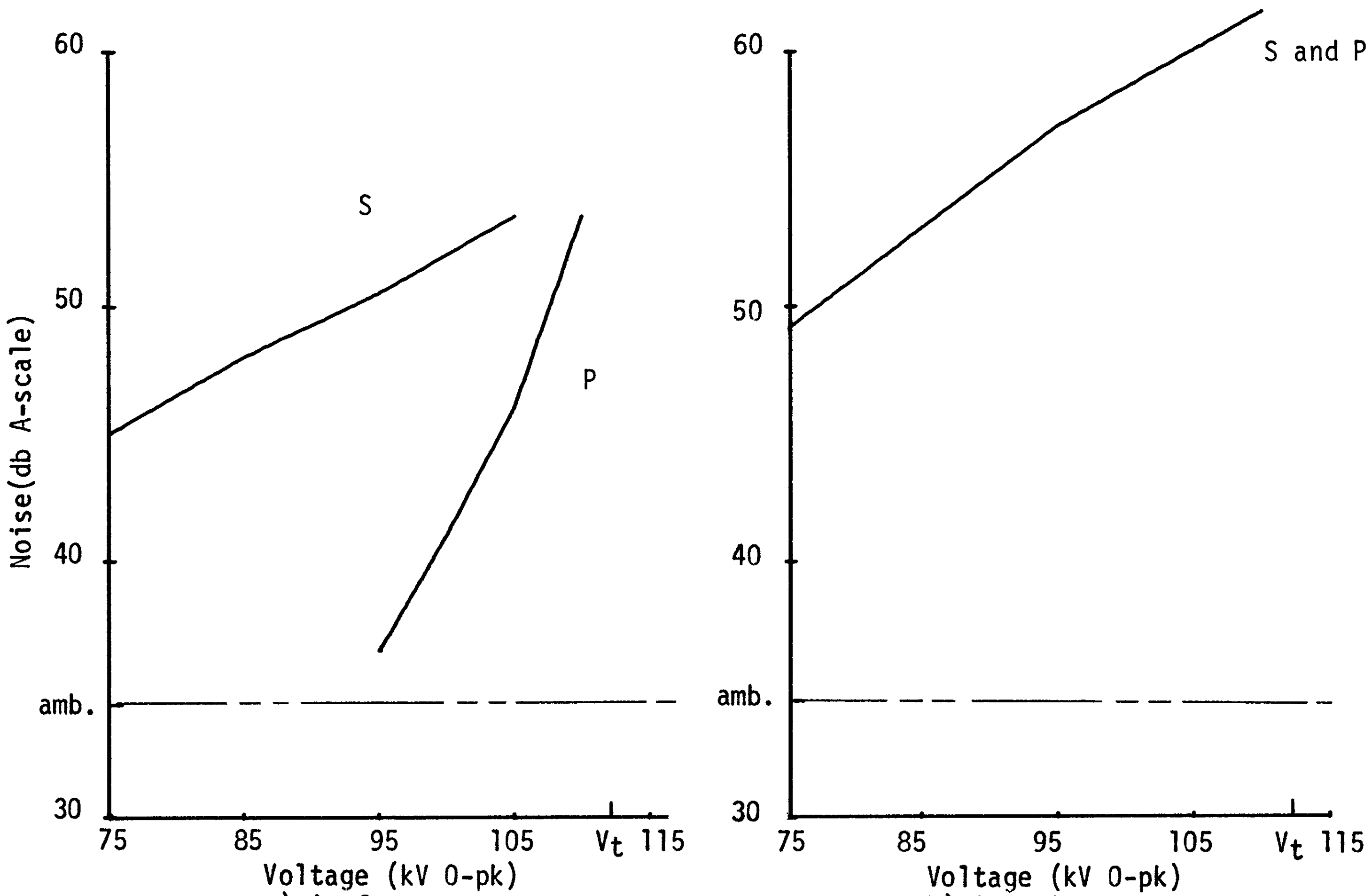

a) in fog

b) in rain

Fig. 4.3 Noise Performance of Porous Conductor in Fog and in Rain. P : 3/4" Porous Conductor (dry corona threshold V_t), S : 3/4" Smooth-Surface Conductor

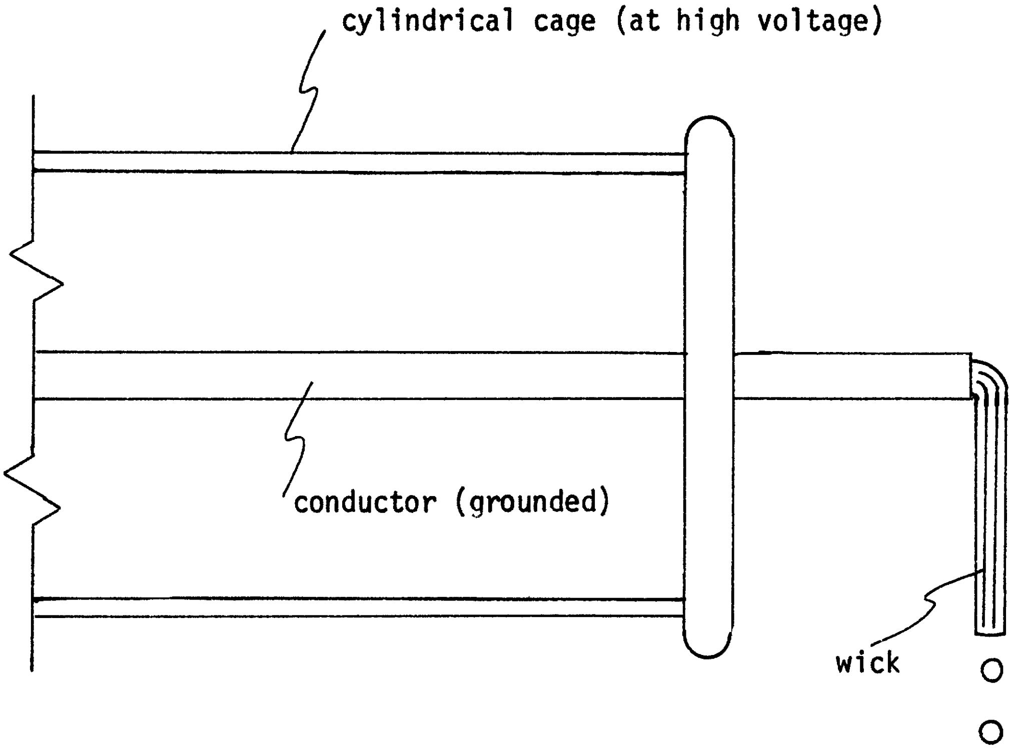

Fig. 4.4 Draining the Porous Conductor with a Wick

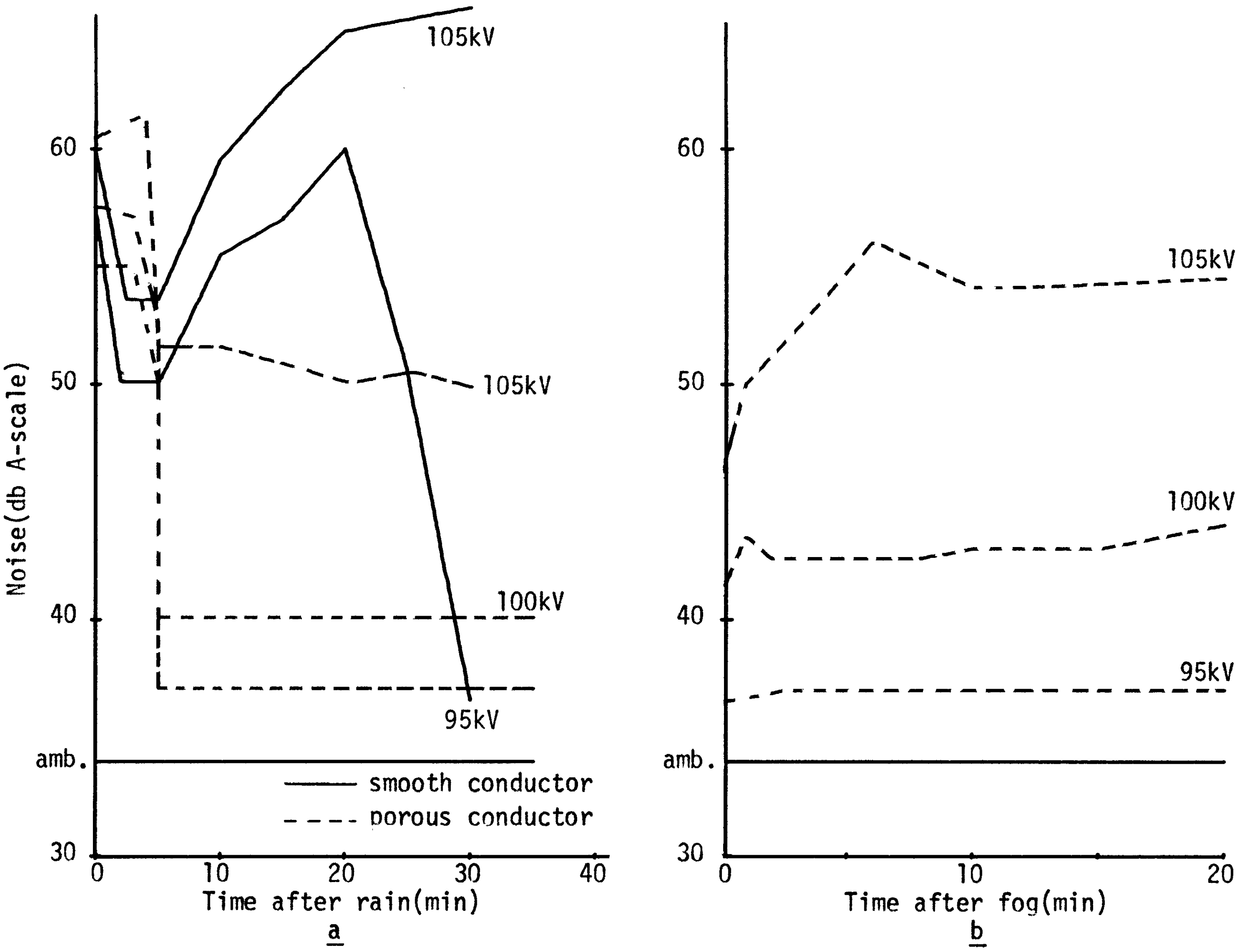

Fig. 4.5 Noise performance of porous conductor after rain and after fog

the sharp drop in noise, at about 5 minutes after rain stopped, coincided with the disappearance of all surface drops. For the smooth conductor, the immediate noise drop of about 6db could be attributed to the termination of splashing and hence the disappearance of all corona sites except for the bottom drops. The steady noise rise thereafter came about probably because of the increased corona activity of the bottom drops as they decreased in size. This behavior, also observed by investigators at Project UHV, is an indication that for a single drop with no liquid addition, there exists an optimal size for corona generation that is less than the maximum possible size. Eventually the drop size decreased to below the instability level and all corona activity ceased as evident in the 95kV curve.

During the testing an anomalous but quite repeatable rise in noise was observed after fogging. As shown in Fig. 4.5b, this rise was most dramatic at the voltage level of 105kV (80% of the smooth conductor dry corona threshold) and was hardly noticeable at 95kV. Randomly situated corona sites appeared in conjunction with the noise rise although no visible causes could be detected from a distance. In an effort to explain these anomalous corona sites an experiment was set up in which the porous conductor was placed parallel to, and about 3" from, a grounded wide-mesh screen. Then with the conductor energized to the point when corona sites appear, the conductor surface was scanned with a 105x microscope placed behind the grounded screen. For every corona site located, the corona issued from a fiber several microns in diameter and tens of microns long. Thus, microscopic fibers, when wet, can be good corona generators at very high gradient levels. These sites were not evident during fogging probably because the surface moisture content was high and surface tension forces kept the fibers in a flat position. In subsequent tests, care was taken to avoid contacting the test conductors with fibrous materials.

Industrial metal spraying processes were explored as a more practical means to obtain a porous metallic layer. The sprayed coatings tested were quite absorbent but had rather low dry corona thresholds except for the very thin ones. With better process control metal spraying could be a practical way to obtain a porous surface.

4.4 The Grooved Stranded Conductor

The best experimental results were obtained with the stranded geometry as described in Chapter 3. Fine grooves were cut on the surface of each strand to promote spreading and to enable transverse liquid movement (between interstices).

The use of surface grooves to improve wettability is well known in heat pipe technology and a detailed analysis of spreading in grooves was made by Bressler and Wyatt(30). Theoretically, the wettability enhancement can be ascribed to an effective increase of $\gamma_{sg}-\gamma_{sL}$ (see Eq. (2.1)) proportional to the surface area increase. Note that enhancement follows only if the contact angle for the flat surface is less than 90°. Alternatively, the grooves can be considered as open capillaries where the formation of menisci cause the water to extend in the direction of the grooves. Apparent perfect wetting can be achieved with grooving even though the actual contact angle on a flat surface is greater than zero. In addition, the grooves, when cut circumferentially, allow the water to encircle each strand; while on a smooth strand, even with zero contact angle, the water tends to remain on the bottomside because of gravity.

Aluminum rods were chosen in the construction since pure aluminum oxide was known to be wetting, but the ease of contamination made maintenance of a well wetting surface a major problem throughout the testing. Anodization gave a very wetting surface, but exposure to the laboratory atmosphere for a few days degraded the wettability appreciably. It was further found that the wettability could be restored by rinsing in a dilute alkaline solution such as sodium hydroxide and then steaming under atmosphere pressure. In Appendix C a detailed account is given of the surface preparations.

Figure 4.6 shows a cross-sectional view of the stranded test conductor. A high dry corona threshold required fine grooves which were very difficult to machine. As a compromise, 50 threads-per-inch grooves were chosen for the outer strands and were cut to a depth of approximately .2mm with an oversized die. After machining, the outer strands were deburred by an electropolishing process and then anodized. The inner strands had 32 threads-per-inch grooves cut to a depth of .5mm and were also anodized but not electropolished. Similar to ACSR cables the strand layers were countertwisted in the bundle. A close fit of the outer strands was obtained by reducing the inner strand diameter by 10 mils; this was necessary since even small gaps between outer strands prevented menisci formation and resulted in surface drop formation during fogging.

Fogging and after-rain tests were made on three similarly constructed conductors; one with grooved strands, one with smooth strands cleaned with solvent to simulate an aged conductor, and one with smooth strands lightly coated with grease to simulate a new conductor. Test results are given in Figs. 4.7 and 4.8.

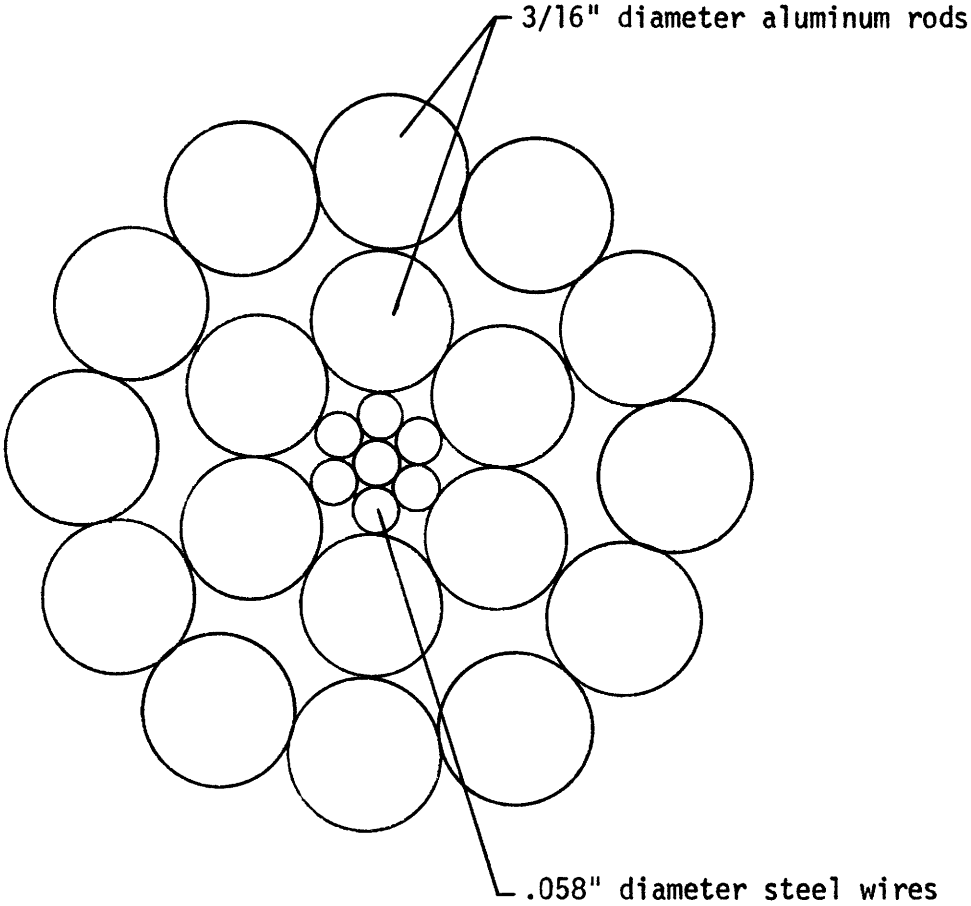

Fig. 4.6 Cross-Sectional View of Stranded Conductor

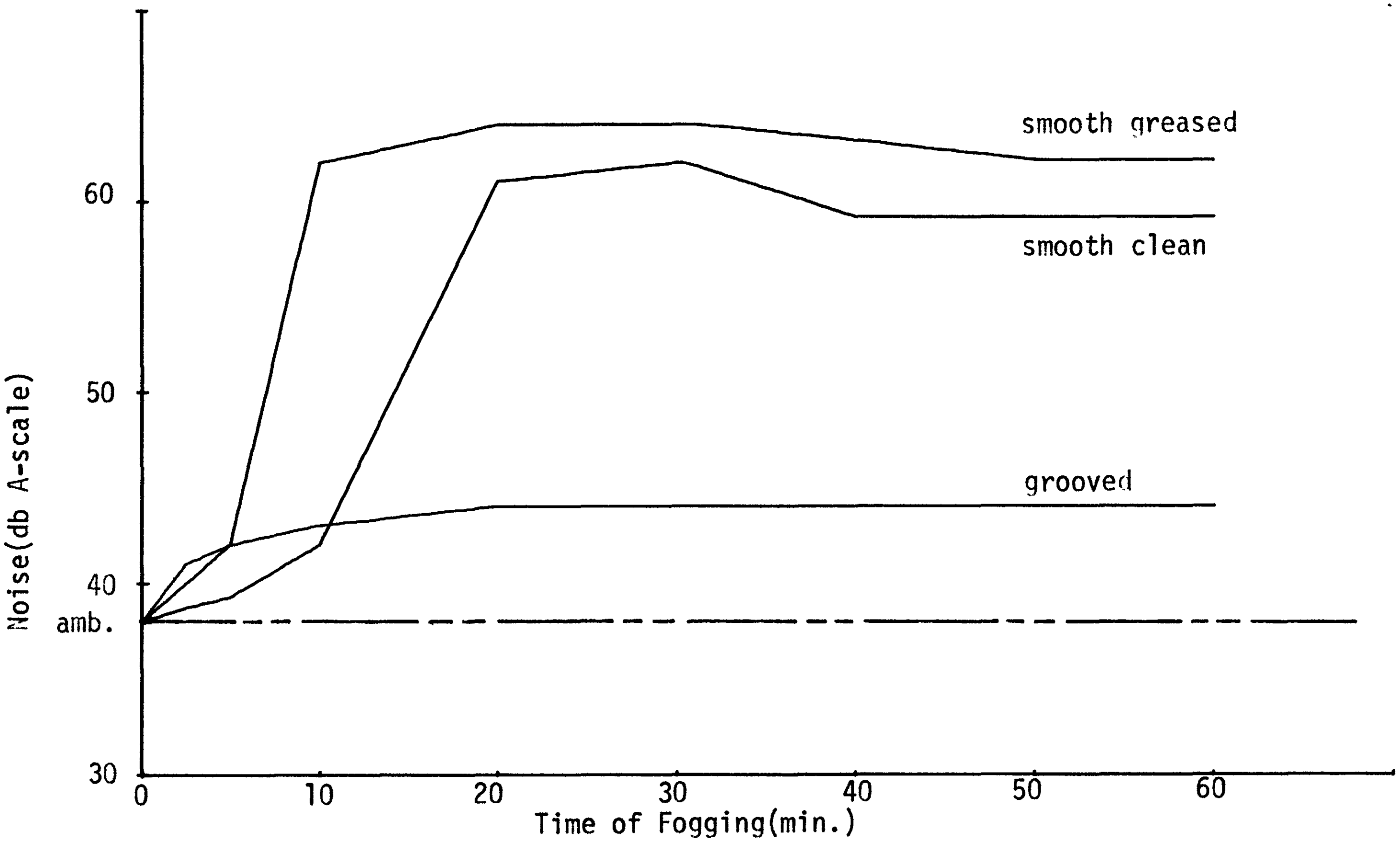

Fig. 4.7 Fogging Test Results (at EPSEL) Dry Corona Threshold of Smooth Conductor: 130 kV 0-pk Test Voltage: 105 kV 0-pk Angle of Incline of Conductors: 6° at upper end and 2° at lower end.

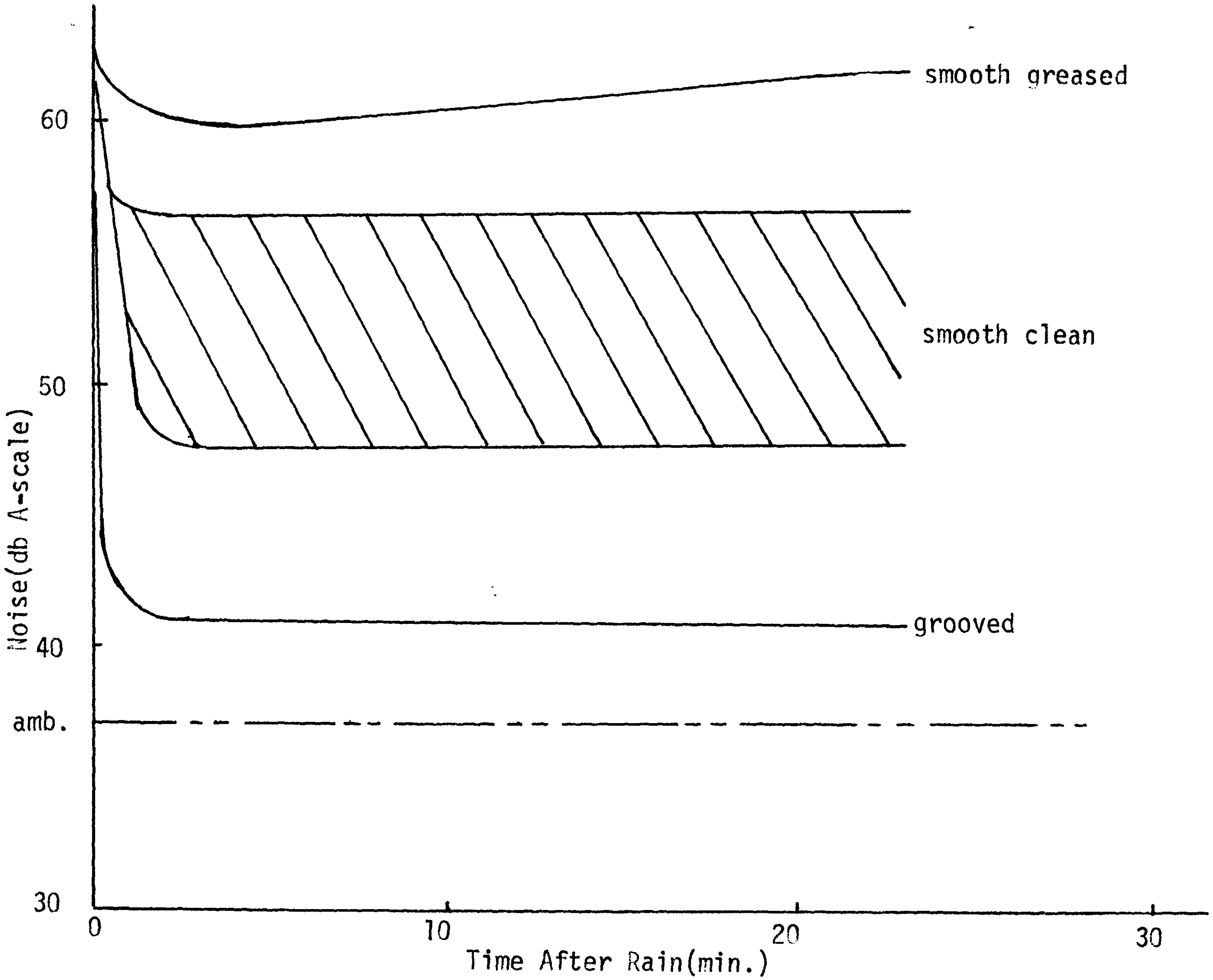

Fig. 4.8 After-Rain Test Results (at EPSEL) Dry Corona Threshold of Smooth Conductor; 130 kV 0-pk. Test Voltage: 105kV 0-pk. Angle of Incline of Conductor: 6° - 2°

In conjunction with the low noise levels registered for the grooved conductor, observations showed that its surface was quite free of water drops as opposed to the smooth ones. There was however a small rise in noise of about 5db above ambient shortly after fogging and several small corona sites were observed on the conductor. The cause of these corona sites was uncertain, but quite likely it was minute foreign particles adhering to the surface. To achieve the improvements recorded, great care was exercised in preparing the surfaces and in keeping them free from contamination due to improper handling. However, no precautions were made to avoid dust settling on the conductor. The anomalous noise rise after termination of fogging found for the porous conductor was not found with the grooved conductor, presumably because of proper handling.

For the cases of the smooth conductors in fog, the low initial noise level followed by a relatively rapid rise was characteristic of such test conditions. Surface droplets large enough to form corona spitters appeared simultaneously with the onset of noise. The length of the initial quiescent period depended on the rate of liquid condensation. Beyond noise onset, the smooth clean conductor showed a small but definite noise decrease. At the same time, the surface drops were seen to coalesce and often to disappear between the strands. Sections of the conductor surface were then covered by only a water film instead of drops. The greased conductor surface showed drop coalescence to a smaller extent but some noise decrease was also recorded.

In the after-rain test, the smooth clean conductor showed a much larger noise fluctuation than the others, mostly because the noise came from only a few remaining drops. In fact, when the surface was carefully washed down with water and the conductor re-energized, only ambient noise would be recorded. In contrast, the greased conductor showed consistently high noise levels for the same procedures.

Similar tests, but on a larger scale, were carried out at Ohio Brass' Frank B. Black Research Center where a high voltage silo 70' in diameter was made available. Two 24' long conductors, one grooved and one smooth, were constructed; each one consisting of four 6' sections connected by threaded studs. The center stainless steel wires (see Fig. 4.6) supported the necessary tension for hanging. Spiralling the outer rods was found to stress the joints and to cause bulging there; to counter this problem, collars were made to slip over the joints. These were made of solid aluminum for the smooth conductor and of porous stainless steel for the grooved conductor. The smooth conductor strands were cleaned to achieve moderate wettability.

Quantitative testing was done in artificial fog and light rain made by spray nozzles with the conductors hanging at an angle of about 3°. The sound measuring equipment was the same as used in our laboratory. Figures 4.9-4.11 give the test results. The noise levels were somewhat different from the measurements made in our laboratory, but showed the same general behavior.

In the light rain simulation, the spray jets were directed at the conductor so that some of the much larger droplets in the central portion of the spray cone impinged on the conductor. The condensation rate was quite large as indicated by the appearance of surface droplets only a few minutes after the jets were turned on, as opposed to over half an hour if the jets were directed parallel to the conductor. A steady downward trend

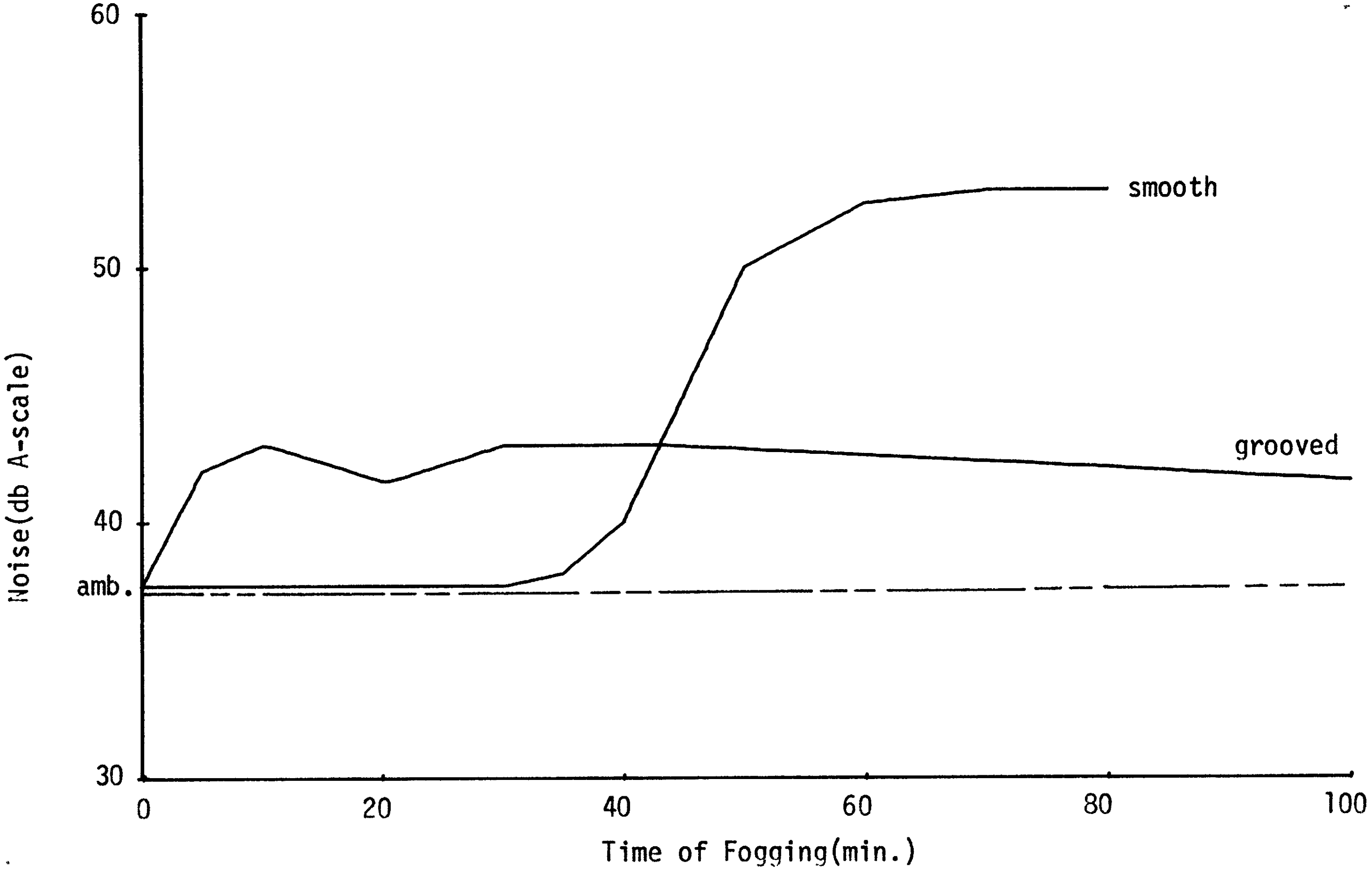

Fig. 4.9 Noise Performance of Smooth vs. Grooved Conductors in Fog (Ohio Brass)
Dry Corona Threshold: Smooth 195 kV, Grooved 180 kV, Test Voltage: 160 kV

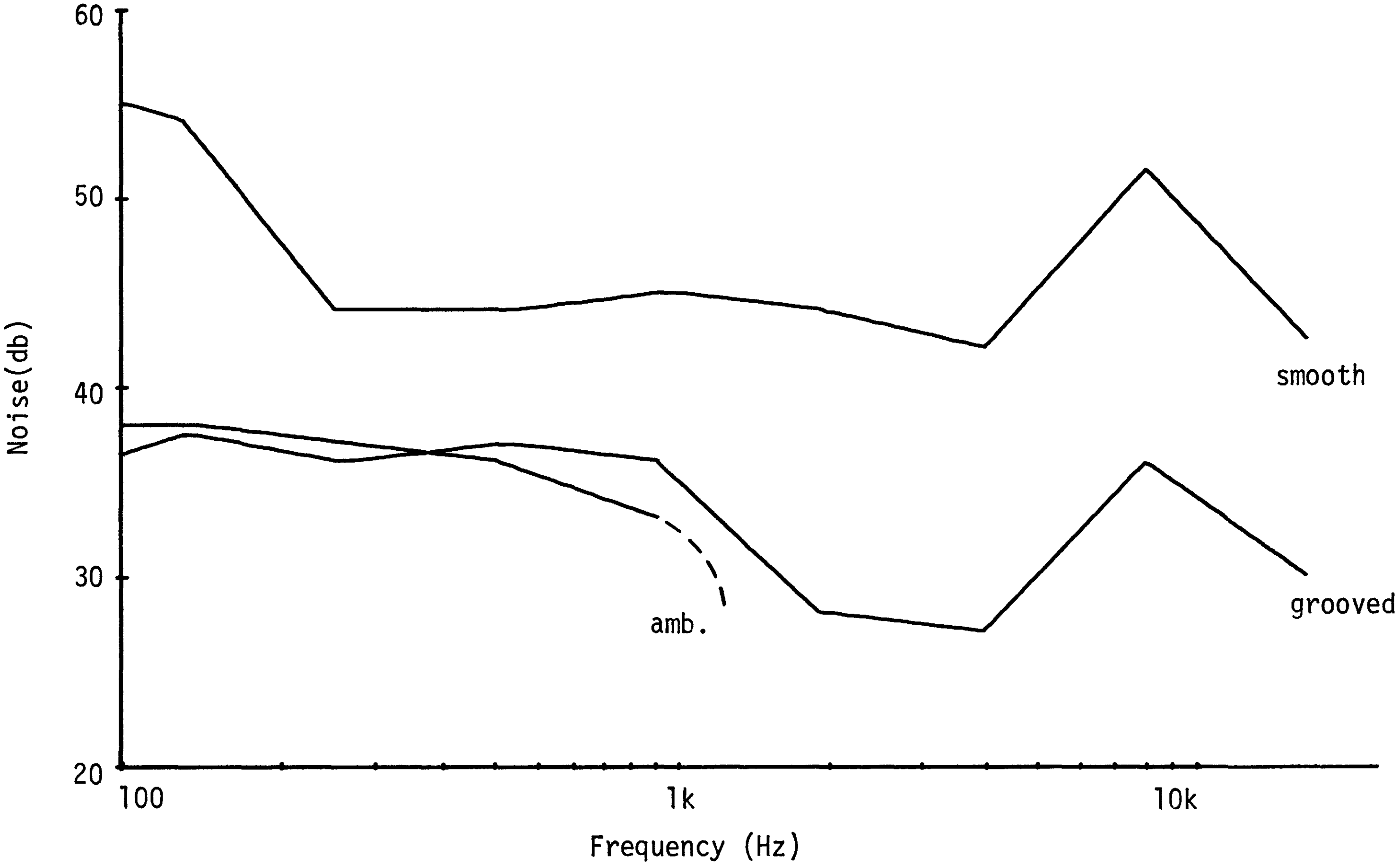

Fig. 4.10 Noise spectrum of smooth vs. grooved conductors after 1 hr. 20 min. of fogging, test voltage: 160 kV

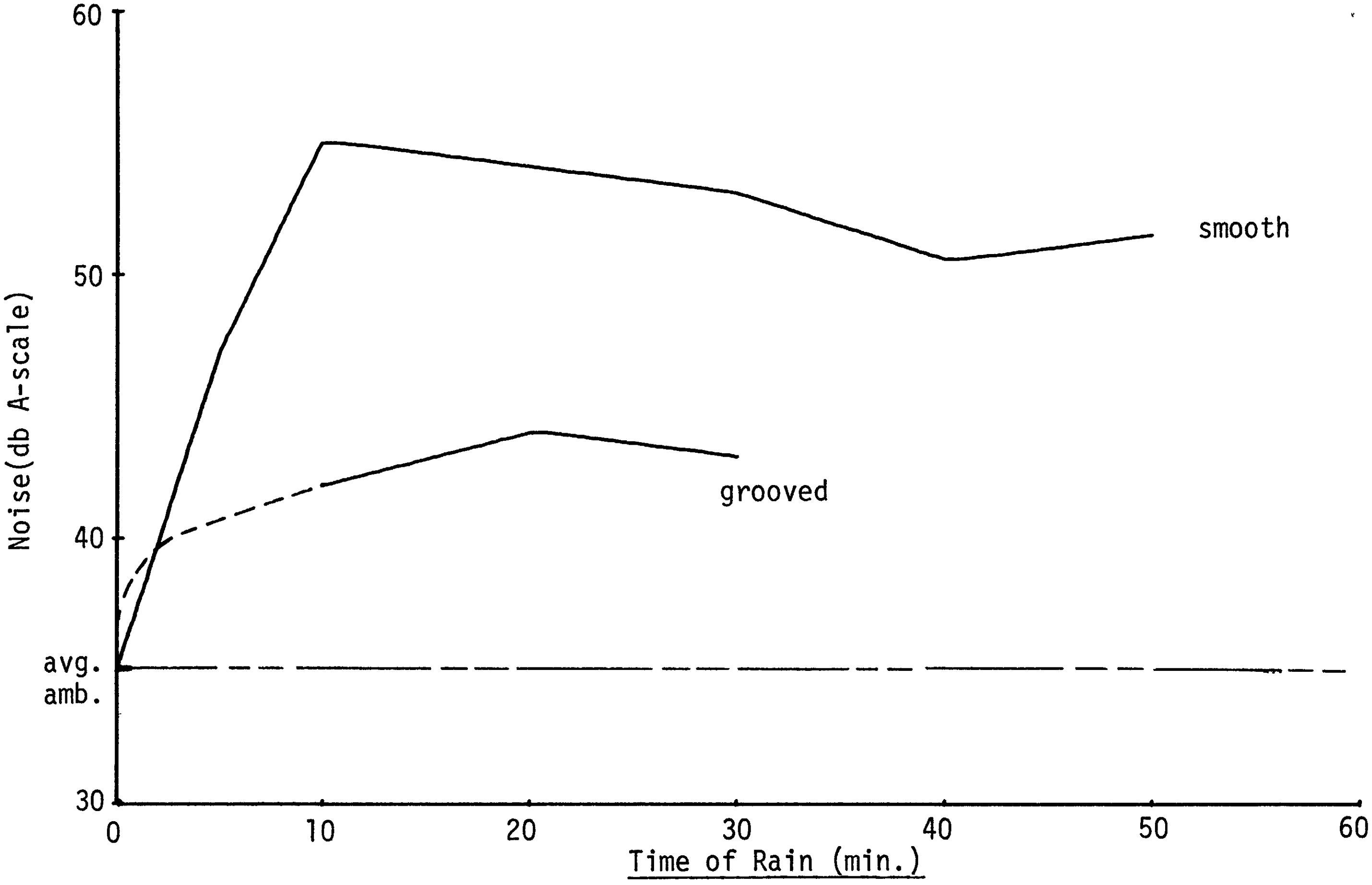

Fig. 4.11 Noise performance of smooth vs. grooved conductors in light rain (Ohio Brass), test voltage: 160 kV

in noise was noted for the smooth conductor as shown in Fig. 4.11. From corona photos, the conductor surface was apparently approaching the fully wetted state with the surface drops decreasing in number. If the collars were also porous in this case, it would not be surprising if the noise continued to drop toward ambient level. Once a liquid continuum forms around the individual strands, even the smooth conductor is capable of absorption and drainage.

To ascertain that the noise improvement was not simply due to variations in test conditions, a visual comparison test in fog was made with both conductors strung side by side and simultaneously energized. The dry corona threshold of the smooth conductor was measured visually and the test voltage was set at 80% of the threshold or above. A series of time exposure photographs taken periodically showed clearly the smooth conductor in vigorous corona activity after 45 minutes of fogging and the grooved conductor with only a few scattered corona sites. Figure 4.12 is a photo taken after one hour and ten minutes of fogging.

An after-rain test was made using the same arrangement with the conductors hosed down to the point of saturation. After a draining period of about two minutes, there was essentially no corona activity from either conductor except for the solid collars on the smooth conductor. This test demonstrated the dependence of drop formation on the history of the wetting process.

4.5 Summary of Test Results

These experiments leave little doubt that the absorption method is effective in reducing noise in fog and after rain. Significant noise reduction was obtained even at gradient levels up to 80% of dry corona

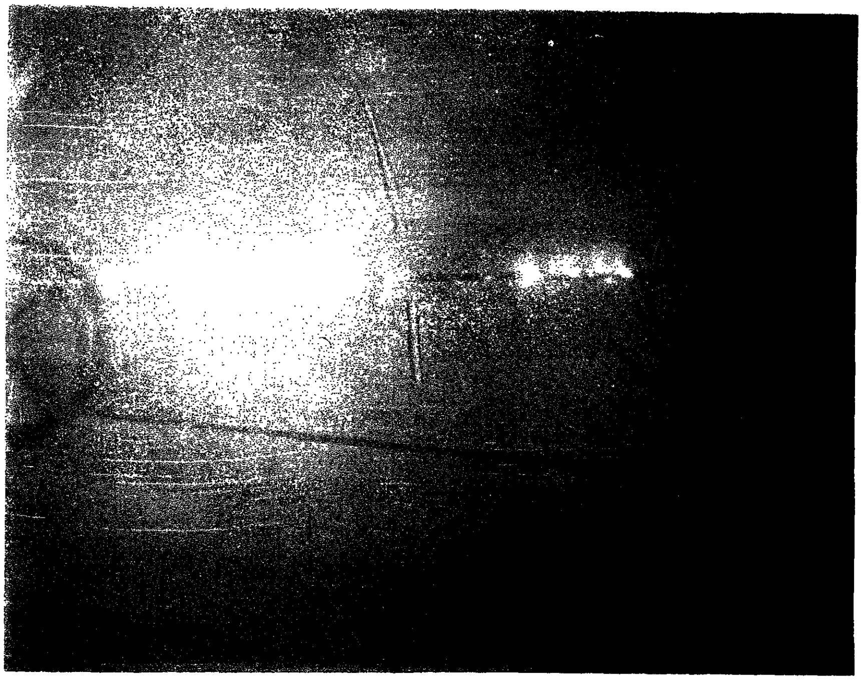

top: smooth conductor
bottom: grooved conductor
applied voltage: 240 kV
dry corona threshold voltage of smooth conductor: 275 kV
time of fogging: 1 hr 10 min

Fig. 4.12 Comparison of visual corona from the smooth and the grooved conductors threshold. The improvements recorded here could not be directly compared to those recorded for other noise reduction methods because of the difference in conductor sizes and test voltages. However, if corona is substantially suppressed, as is evident in Fig. 4.12, then significant noise improvement should result regardless of the scale of the experiment. The residual corona sites due to foreign particles after absorption of the water drops would be the sole limiting factor in the noise improvement.

The test results of the clean smooth conductor illustrate very well the effect of contact angle hysteresis on surface drop formation. In fog, drops formed all over the conductor surface and resulted in much corona activity; after thorough drenching of the conductor in rain, few drops remained to cause corona. Based on this observation, one must conclude that noise measurements made after rain do not necessarily give sufficient information on the noise performance of a conductor.

CHAPTER 5

A QUASI-ONE-DIMENSIONAL FLOW MODEL OF THE ABSORBENT CONDUCTOR

5.1 General Discussion

The effectiveness of an absorbent conductor depends on its ability to drain the collected water. This is true even for low liquid condensation rates because any collected moisture will tend to concentrate at the span midsection with subsequent saturation there. An analytical model must be formulated in order to predict adequately the liquid movement inside the absorbent conductor and to establish design criteria. Such criteria are especially important since the need for wicking is anticipated at the essentially horizontal span midsection.

As discussed in Chapter 3, any absorbent conductor must exhibit a relatively high longitudinal permeability as well as an adequate degree of absorbency. These two requirements restrict any applicable design to include narrow, longitudinally uniform channels, an illustration of which is the stranded bundle described in Chapter 4. This narrow channel restriction places the flow into the viscosity-dominated regime, thus allowing the neglect of momentum and resulting in considerable simplification of the analysis.

The flow in a multitude of parallel channels can be modeled in two ways. As shown in Fig. 5.1, a discrete model assigns sets of flow variables and flow equations to each channel with transfer of mass coupling the flow in adjacent channels. A continuum model, on the other hand, deals with only one set of variables which are the flow variables of Fig. 5.1 averaged over the cross section of participating channels. In this

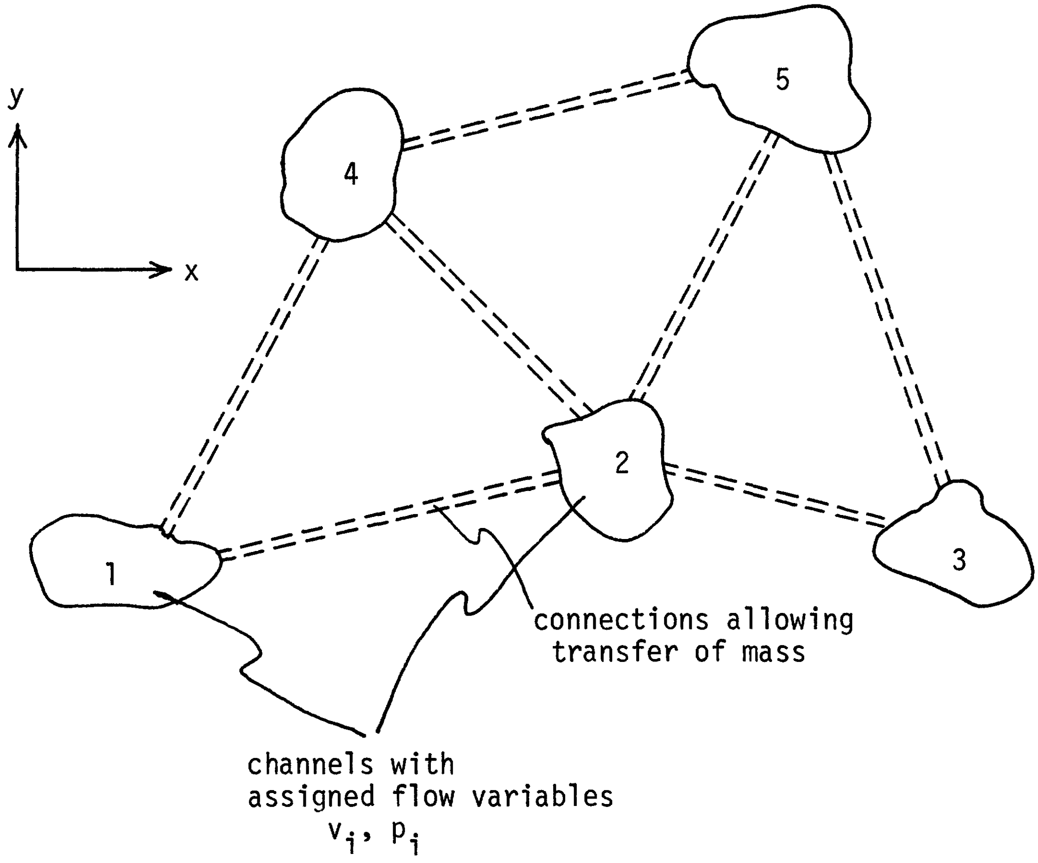

Fig. 5.1 Discrete modeling of parallel flow channels

model, v_i and p_i of Fig. 5.1 is replaced by $v(x,y)$ and $p(x,y)$. While the discrete model is capable of giving a more detailed flow pattern, the continuum model is chosen for development here because of its mathematical simplicity. Comparison with experiments shows that the model is not entirely adequate in representing a bundle structure of the kind discussed in Chapter 4, but the model does bring out the salient features of the flow. In Chapter 7 an other absorbent conductor design is proposed for which the model fits quite well.

We are interested primarily in the behavior of the absorbent conductor under steady rain or fog and in the draining process after rain. Therefore the model developed in this chapter includes the possibility of distributed water influx and allows transient analysis. In addition, it also takes into account variations in the angle of incline and anisotropy of the absorbent conductor.

5.2 Description of Model

Figure 5.2 shows how the internal state of a general flow structure is described in the continuum model. A homogeneous distribution of distinct but interconnected channels defines a flow area whose shape is arbitrary (shown as square in figure). Since unsaturated flow is the case of interest, the channels can be divided into filled and unfilled regions which are assumed separated by a free surface, where the liquid pressure is designated p_c and is determined by capillary effects. To see this we refer to the stranded structure mentioned in Chapter 3 and reillustrated in Fig. 5.3. In this example, the free surface is a fictitious surface between the second and third levels of interstices. Provided the liquid forms a continuous film around each of the strands, the annular holes just

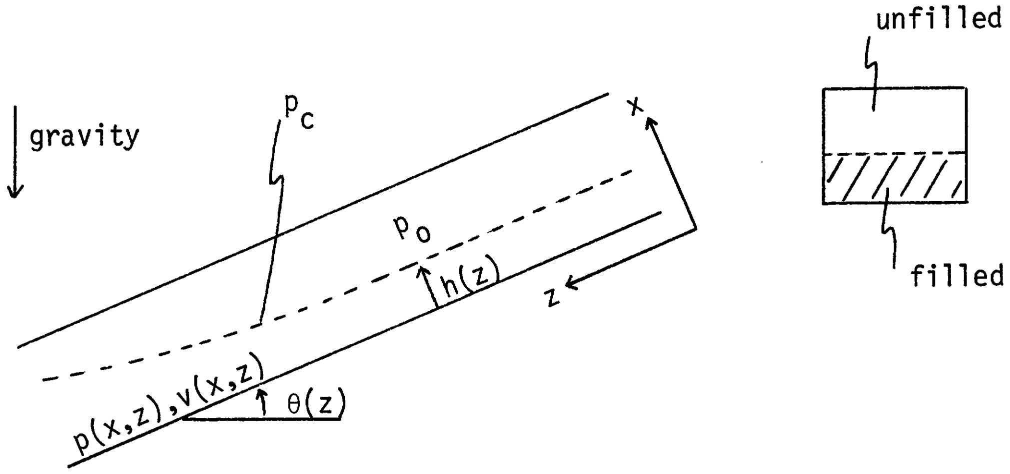

Fig. 5.2 Continuum model of an absorbent conductor

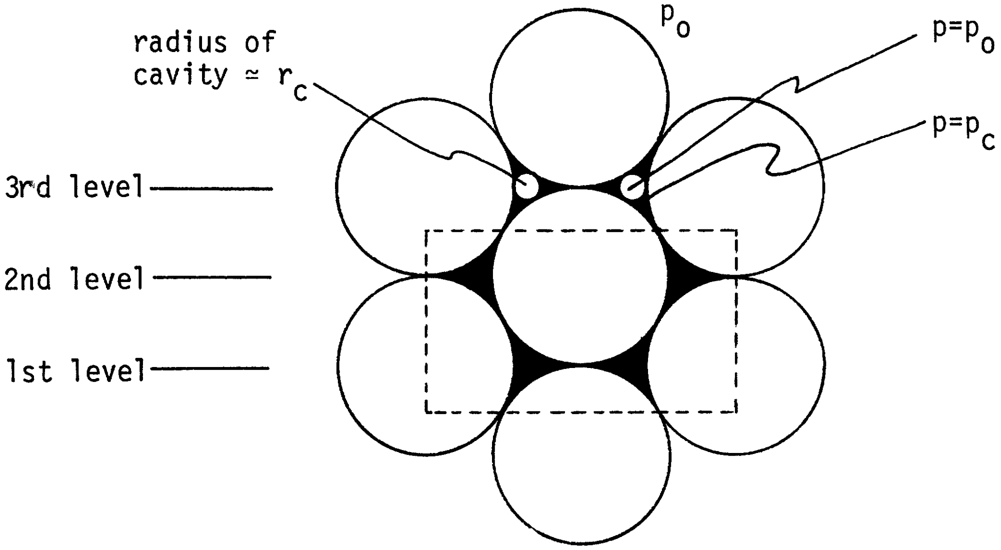

Fig. 5.3 A stranded bundle at an intermediate level of saturation

above the free surface, illustrated by the third level in Fig. 5.3, remain unfilled but are near a well defined critical radius r_c when filling is imminent. The pressure in the cavities is assumed to be p_o, the atmospheric pressure; i.e., at least one end of the cavity is open to the external environment. Because $p_o - p_c \approx \gamma/r_c$ where γ is the liquid-air surface tension coefficient, the pressure p_c in the liquid at such a level is always kept near $p_o - \gamma/r_c$.

Two obvious choices of a coordinate system exist: one with an axis parallel to the real horizontal line, or one with an axis parallel to the conductor. The latter choice is clearly much simpler here since the coordinate axes coincide with the principle axes of the anisotropic medium. The error introduced by the slight curvature of the conductor is expected to be negligible.

For the geometry of the overhead conductor, i.e., a very long length compared with the cross-sectional dimensions, the longitudinal velocity v_z is expected to be the dominant component of $\bar{v}$. This situation is suitable for quasi-one-dimensional modeling where the variations in the transverse dimensions are suppressed. Three flow variables, the longitudinal velocity v(z), the pressure p(z), and the free surface height h(z), describe the state of the quasi-one-dimensional system as shown in Fig. 5.2.

Since the flow actually takes place only over a portion of the total cross-sectional area, i.e., the darkened areas in Fig. 5.3, it is necessary to clearly define how the velocity is averaged. We choose to average it over the entire cross section of the filled region as indicated by the dotted box in Fig. 5.3, thus allowing us to directly relate h to p. This averaged velocity is much smaller than the actual velocity and proper account must be taken when parameters involving the velocity, i.e., the Reynold's number, are calculated. It might be mentioned briefly that averaging can introduce significant errors when products of averaged terms are involved. For example, in open channel flows, the error introduced by using the average velocity in the kinetic energy term must be compensated for by the introduction of a correction coefficient. In this study all the nonlinear terms involve only one average quantity and no averaging errors are present.

The starting point for formulating a set of governing equations is the Navier-Stokes Equation in the integral form(29).

$$\int_V \frac{\partial}{\partial t} \rho v_i v_j n_j dV + \int_V p\bar{n} dV = \int_V -\rho g\bar{k} dV - \int_V \eta \nabla^2 v_i dV \tag{5.1}$$

where the indices denote Cartesian components and $\bar{k}$ is the unit vector opposite to the direction of gravity. As mentioned above, we expect viscous flow and hence neglect at the outset the momentum flux term altogether. Appendix D discusses the estimation of the Reynold's Number(29) which justifies such a step.

The last term on the right hand side of (5.1) represents viscous effects and can be replaced by fv_i where f is a frictional factor (expressed in tensor form for anisotropic media). As a simple example, the drag force in Poiseuille flow can be represented exactly in this way(29). Appendix D also shows that the flows of interest are laminar, for which f is dependent only on geometry. In general, f may be difficult to calculate exactly, but it can always be measured.

Applying (5.1) to an elemental volume as shown in Fig. 5.4, and considering the longitudinal component,

$$h[p^*(z+\Delta z) - p^*(z)] - p_c\Delta h = \rho g\alpha h\Delta z - f_z v_z h\Delta z \qquad (5.2)$$

where $p^* = \frac{1}{h}\int_0^{h(z)} p(x,z)dx$, $\rho g\alpha$ is the longitudinal component of the gravitational force, and v_z is the averaged velocity. For a homogeneous medium p_c is constant and is chosen here as the zero reference pressure. Dividing (5.2) by $h\Delta z$ and taking the limit as Δz approaches 0,

$$\frac{1}{h(z)}\frac{\partial}{\partial z}(h(z)p^*(z)) = \rho g\alpha(z) - \frac{1}{K_z}v_z(z) \qquad (5.3)$$

$1/K_z$ is used in place of f_z since K_z corresponds to the permeability as discussed in Chapter 3. Note that for convenience the viscosity coefficient is included in K which has the units cc-sec/gm. The partial derivative in (5.3) indicates that time dependence of the variables is implied.

Conservation of mass can be applied to the control volume of Fig. 5.4. If the top surface of the control volume is assumed to move with the free surface, then

$$n_e\frac{\partial A}{\partial t} + \frac{\partial}{\partial z}(v_z A) = Q'$$

where n_e is the ratio of pore (air space) volume to total volume, A the cross-sectional area of flow, and Q' the distributed liquid addition from the boundary. For a given cross-sectional geometry,

$$A = \int_0^h hw(x)dx$$

where w(x) is the width of the structure. Since the inclusion of this width function adds mathematical complexity and obscures the basic dynamical features of the flow, a constant structure width is assume in our model. With this assumption the mass conservation equation becomes

$$n_e\frac{\partial h}{\partial t} + \frac{\partial}{\partial t}(v_z h) = q' \qquad (5.4)$$

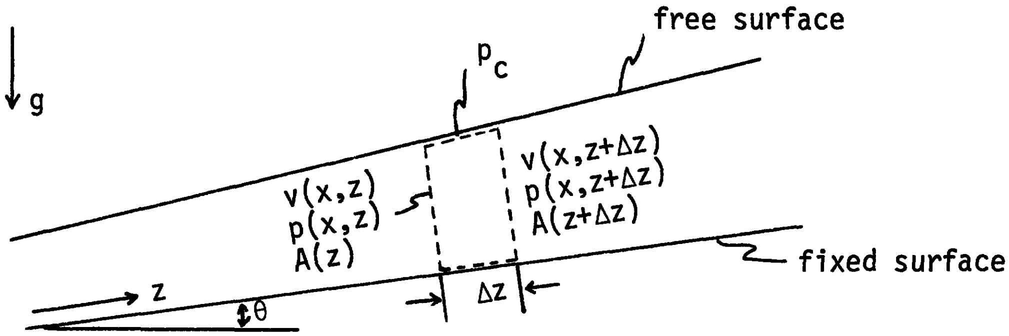

Fig. 5.4 Control volume (dotted box) for integration

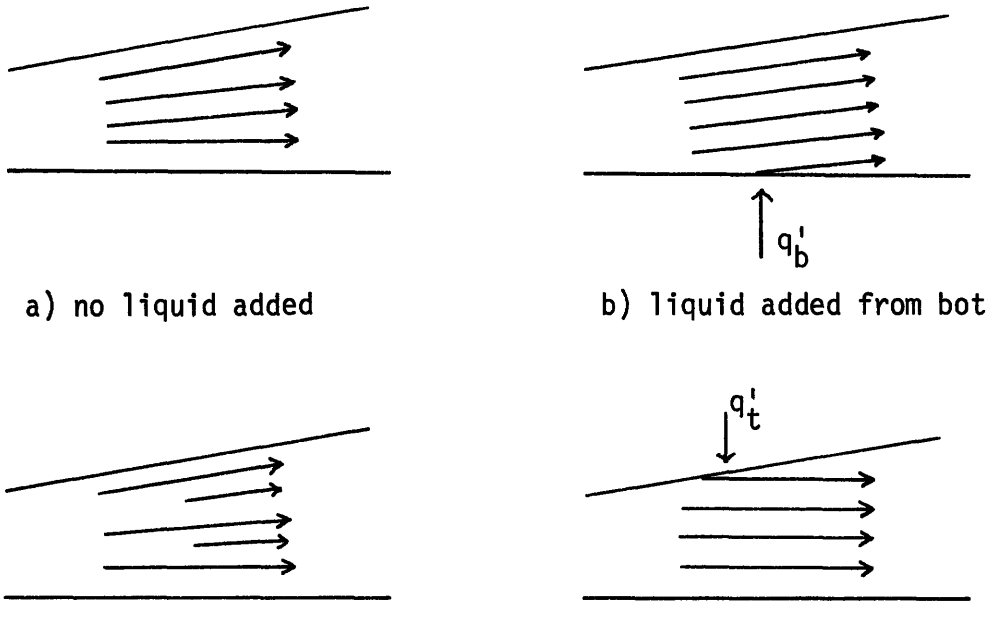

a) no liquid added

b) liquid added from bottom

c) liquid added from side

d) liquid added from top

Fig. 5.5 Possible flow patterns with or without liquid addition where q' is in units of volume per unit area per unit time.

An additional equation is needed to relate the three dependent variables v, h, and p*. In both open channel flows(31) and in percolative flows(27) where quasi-one-dimensional modeling is used, the approximation of a hydrostatic pressure distribution gives the third relation.

$$p(x,t) = \rho g(x-h) \tag{5.5}$$

This approximation, however, is limited in its range of applicability for anisotropic media. To see this we can simply consider the extreme case where transverse flow is completely prohibited. This corresponds in Fig. 5.1 to channels that are disconnected everywhere except at the ends. Each channel then resembles a closed pipe, for which the area remains constant and the pressure varies to satisfy mass conservation and boundary conditions. When transverse motion is sufficiently restricted, the transverse pressure variation can no longer be hydrostatic, but rather the cross-sectional height h tends to remain constant. Because of this effect, a condition must be found to determine the region of validity of the hydrostatic approximation.

In searching for a new relation that is of more general applicability in anisotropic media, one should realize that this relation must include the hydrostatic approximation as a special case. Also it is clear that a transverse permeability K_x, analogous to K_z in the longitudinal direction, must play a significant role in this new relation. This hints at a closer look at the transverse component of the Navier-Stokes Equation, which has been neglected so far in the quasi-one-dimensional formulation:

$$\frac{\partial p}{\partial x} = -\rho g\beta - \frac{1}{K_x} v_x \tag{5.6}$$

where $\rho g \beta$ is the component of the gravitational force in the transverse direction.

Figure 5.5 shows the possible patterns of a conductor segment and how flow depends on the direction of liquid addition. In general, v_x can be represented as a power series in x.

$$v_x = v_{xo} + c_1 x + c_2 x^2 + c_3 x^3 + \dots \tag{5.7}$$

The constant term corresponds to fluid addition from the bottom, $v_{xo} = q'_b$. A self consistent derivation of the constants c_i appearing in (5.7) is not allowed by quasi-one-dimensional modeling, but by approximating the power series with only the first two terms, (5.7) can be usefully combined with (5.6) and the mass conservation condition to give the needed new relation.

To see this, a mass conservation equation involving v_x can be obtained by again considering the control volume of Fig. 5.4 with the top surface now assumed stationary with time. Incompressibility of the liquid requires that the total flux out of the control volume must be zero and leads to

$$v_z h(z+\Delta z) - v_z h(z) + \Delta z v_{x\text{-surf}} - \Delta h v_{z\text{-surf}} - \Delta z q'_b - q'_s \Delta z = 0$$

where q'_s is the liquid added from the side. Dividing through by Δz and taking the limit as $\Delta z \rightarrow 0$ results in

$$\frac{\partial}{\partial z}(v_z h) + v_{x\text{-surf}} - v_{z\text{-surf}} \frac{\partial h}{\partial z} = q'_s + q'_b$$

Substituting in (5.3)

$$n_e \frac{\partial h}{\partial t} + v_z \frac{\partial h}{\partial z} - q'_t = v_{x\text{-surf}} \tag{5.8}$$

where q' has been replaced with $q'_t + q'_s + q'_b$ and $v_{z\text{-surf}} = v_{z\text{-avg}}$ is assumed. The last assumption follows because total longitudinal flow forces vary little over the cross section for small surface slopes.

Integrating (5.6) with respect to x, and using the linear approximation of v_x,

$$p(x) - p_b = -(\rho g\beta + q_b'/K_x)\,x - \frac{c_1}{K_x}\frac{x^2}{2} \tag{5.9}$$

where p_b is the pressure at the bottom. Note that if the bottom surface is the boundary between air and the porous medium, p_b is allowed to vary freely within a limited range because of the menisci which exist there. The boundary condition on p at the free surface gives

$$p_b - p_c = (\rho g\beta + \frac{1}{K_x} q_b')\,h + \frac{c_1}{K_x}\,\frac{h^2}{2} \tag{5.10}$$

where p_c is the capillary pressure as defined earlier and is set to zero for a homogeneous medium.

Using the relation

$$v_{x\text{-surf}} = q_b' + c_1 h$$

(5.9) may be integrated with respect to x from 0 to h and an expression for p* is obtained.

$$p^* = p_b - (\rho g\beta + \frac{1}{K_x} q_b')\,\frac{h}{2} - \frac{h}{6K_x}(v_{x\text{-surf}} - q_b')$$

Substitution of p_b from (5.10) results in

$$p^* = (\rho g\beta)^*\,\frac{h}{2} + \frac{h}{3K_x}\,v_{x\text{-surf}} \tag{5.11}$$

where

$$(\rho g\beta)^* = \rho g\beta + q_b'/3K_x \tag{5.12}$$

Combining (5.8) and (5.11),

$$n_e \frac{\partial h}{\partial t} + v_z \frac{\partial h}{\partial z} - q_t' = \frac{3K_x}{h} (p^* - (\rho g \beta)^* \frac{h}{2}) \qquad (5.13)$$

This is the desired result with p^* and $(\rho g \beta)^*$ defined respectively by (5.11) and (5.12).

The validity of (5.13) can be checked for two limiting cases:

1) K_x approaches ∞; i.e., negligible transverse flow restriction.

$(\rho g \beta)^*$ approaches $\rho g \beta$ from (5.12) and p^* approaches $\rho g \beta\ h/2$ which is the hydrostatic limit.

2) K_x approaches 0; i.e., complete transverse flow restriction.

For finite pressures, the left hand side approaches 0 and the flow approaches closed pipe flow with any height variation accounted for by liquid addition from the top.

Equation (5.13) shows that addition of liquid from the top only indirectly affect the internal pressure via the change in channel height. On the other hand addition of liquid from the bottom results directly in an apparent change in the gravitational force.

Adding liquid from the side only modifies the higher order constant in the expansion of v_x; provided that any side liquid addition is included in the mass conservation equation, (5.4), no further consideration is necessary.

A limiting flux from the bottom can be deduced from (5.12) in the hydrostatic limit. The pressure at the bottom is given by $(\rho g \beta)^*$ h, and if it is not to exceed atmospheric, then the limiting flux must satisfy

$$(\rho g \beta + \frac{q'_{b\ max}}{3K_x})h = (p_o - p_c) \qquad (5.14)$$

where p_o is atmospheric pressure.

5.3 An Alternative Approach

The flow structure could be considered as a porous medium at the outset, with flow governed by Darcy's Law$^{(27)}$,

$$\bar{v} = \frac{k}{\mu} \nabla\phi \tag{5.15}$$

where $\bar{v}$ is the averaged velocity; k the permeability (expressed in tensor form for anisotropic media); μ the liquid viscosity; and $\phi = p + \rho gh$ the so-called piezometric head. The similarity of (5.15) to (5.3) is obvious when the $\rho g\alpha$ term in (5.3) is integrated (for α const) and incorporated into the pressure term. By equating k_i/μ to K_i, an exactly parallel analysis will result in the same set of quasi-one-dimensional equations.

Equation (5.15), together with the assumption of incompressible flow, $\nabla \cdot \bar{v} = 0$, results in Laplace's Equation in p or ϕ. In general, the solution of Laplace's Equation with a free surface is rather difficult and can be solved exactly only in some special cases. A quasi-one-dimensional model, called the Dupuit-Forcheimer approximation$^{(27)}$, is often relied upon which corresponds to the one developed here in the hydrostatic limit.

5.4 Theoretical Case Studies

Equations (5.3), (5.4), and (5.13) form a closed set of equations relating the variables v, h, and p*. When combined with proper boundary and initial conditions, this set of nonlinear, first order, partial differential equations appears to form a well posed problem whose solution likely requires numerical integration. Here a complete numerical solution has little engineering value in the sense of providing understanding or establishing design criteria. In this section a set of simplified cases are considered where significant physical features of the problem are singled out; the results are then compared with experimental data in the next chapter.

5.4.1 Hydrostatic Limit

Normalizing (5.13) gives in the steady state

$$\kappa(v'_z \frac{\partial h'}{\partial z'} - (q'_t)) = p^{*\prime} - h'$$

where $\kappa = \frac{V_o h_o^2}{3Lp_o^* K_x}$ is a dimensionless constant involving the characteristic quantities v_o, h_o, L and $p_o^* = (\rho g \beta)^* \, h_o/2$. Provided $\kappa << 1$, the hydrostatic limit is a good approximation as demonstrated later in section 5.4.2. In this limit (5.13) can be replaced by

$$p^* = (\rho g \beta)^* \, h\, /2 \tag{5.16}$$

The governing set of equations is reduced to

$$\frac{\partial}{\partial z} (\rho g \beta)^* \, h(z,t) = \rho g \alpha(z) - \frac{v_z(z,t)}{K_z} \tag{5.17}$$

$$n_e \frac{\partial}{\partial t} h(z,t) + \frac{\partial}{\partial z} v_z(z,t)\, h(z,t) = q' \tag{5.18}$$

where q' is considered known.

5.4.1.1 Uniform Flow ($\partial/\partial z = 0$) with $q' = 0$

This constitutes the simplest flow situation. After deleting all the appropriate terms and combining the equations (5.17) and (5.18)

$$h = \frac{q}{\rho g \alpha K_z} \tag{5.19}$$

where $q = v_z h$ is the total volume of flow per unit width imposed by an upstream condition. Although this case is theoretically trivial, it provides a straightforward comparison between theory and experiment.

5.4.1.2 Steady State Drainage

This case is of special interest for two reasons. The first is that it points out the physical significance of the $\partial p^*/\partial z$ term as representative of a diffusive action. The second is that on practical grounds, drainage is the main focal point of this investigation. This case is represented by Fig. 5.6.

Boundary conditions may be imposed in several ways; by the occurrence of saturation or uniform flow; by an open end termination; or by the presence of wicks as shown in Fig. 5.6. For the full set of equations (5.3), (5.4), and (5.13), three boundary conditions are needed to fully specify the problem. In the hydrostatic limit, however, one equation is eliminated and only two boundary conditions can be specified. If three boundary conditions can be physically imposed, this would mean that the hydrostatic approximation is violated somewhere in the region of interest and the full set of equations must be used to calculate the flow profile.

Equations (5.17) and (5.18), without the $\partial/\partial t$ term, combine into

$$\frac{d}{dz} K_z\, h(z)[\rho g\alpha(z) - \frac{d}{dz}\, \rho g\beta h(z)] = q' \tag{5.20}$$

where $\alpha(z)$ and q' are known. Certain special cases of this equation allow direct integration.

5.4.1.2.1 $q' = 0$; α Constant

Replacing (5.18) by the condition of constant flux, $v_z h = q$, and substitution into (5.17), lead directly to

$$\frac{dh}{dz} + \frac{q}{\rho g\beta K_z h} = \alpha/\beta \tag{5.21}$$

the solution of which is

$$\frac{h-h_L}{a_2} + \frac{a_1}{a_2^2}\, \ell n\left(\frac{a_2 h - a_1}{a_2 h_L - a_1}\right) = z - L \tag{5.22}$$

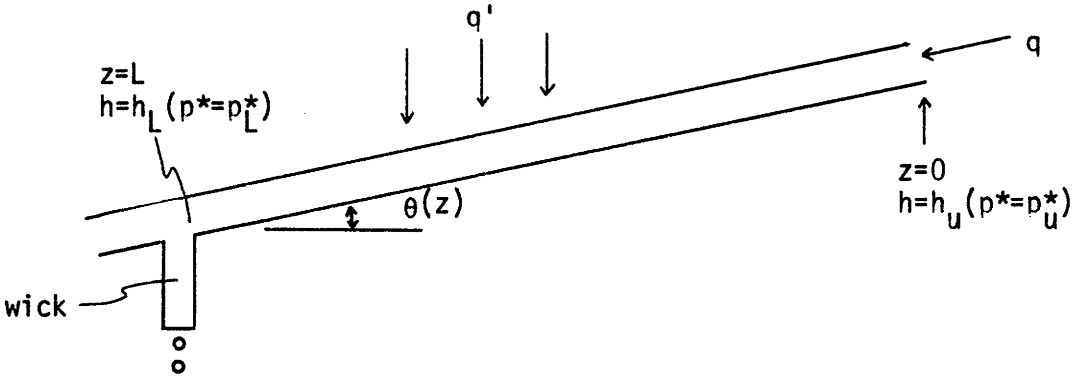

Fig.5.6 Diagram of drainage with nonzero angle of incline

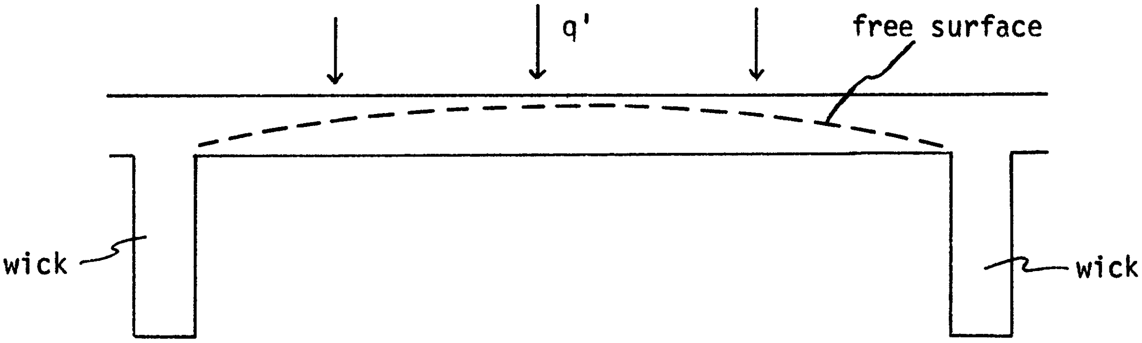

Fig.5.8 Horizontal drainage by wicking

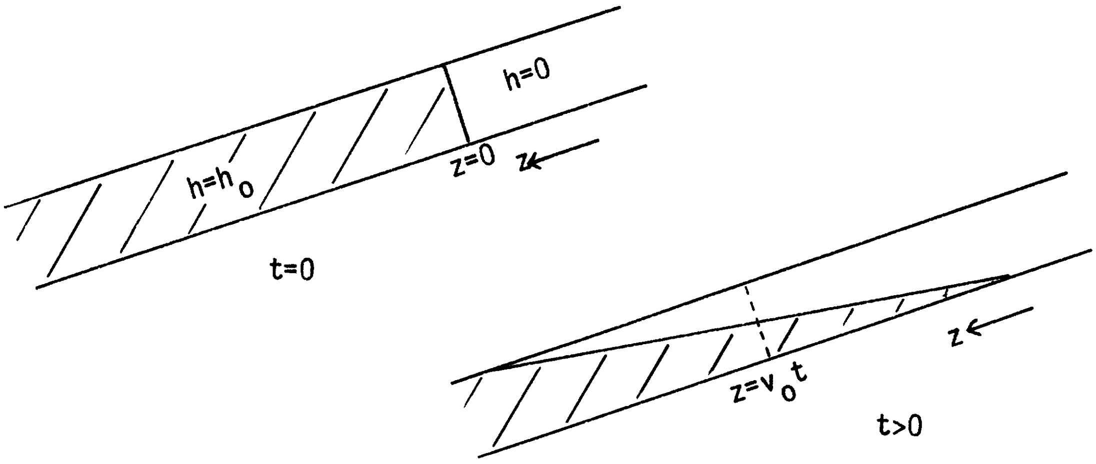

Fig.5.9 A hypothetical transient flow profile

where $a_1 = \frac{q}{\rho g \beta K_z}$, $a_2 = \alpha/\beta$, and L is the position where the boundary condition is applied. As an example, Fig. 5.7 shows the profile as given by (5.22) for a saturated end condition* with uniform flow upstream; the parameters used in the calculations match those of the experiments described in Chapter 6.

In the special case of $\alpha = 0$ ($\beta = 1$), (5.21) can be directly

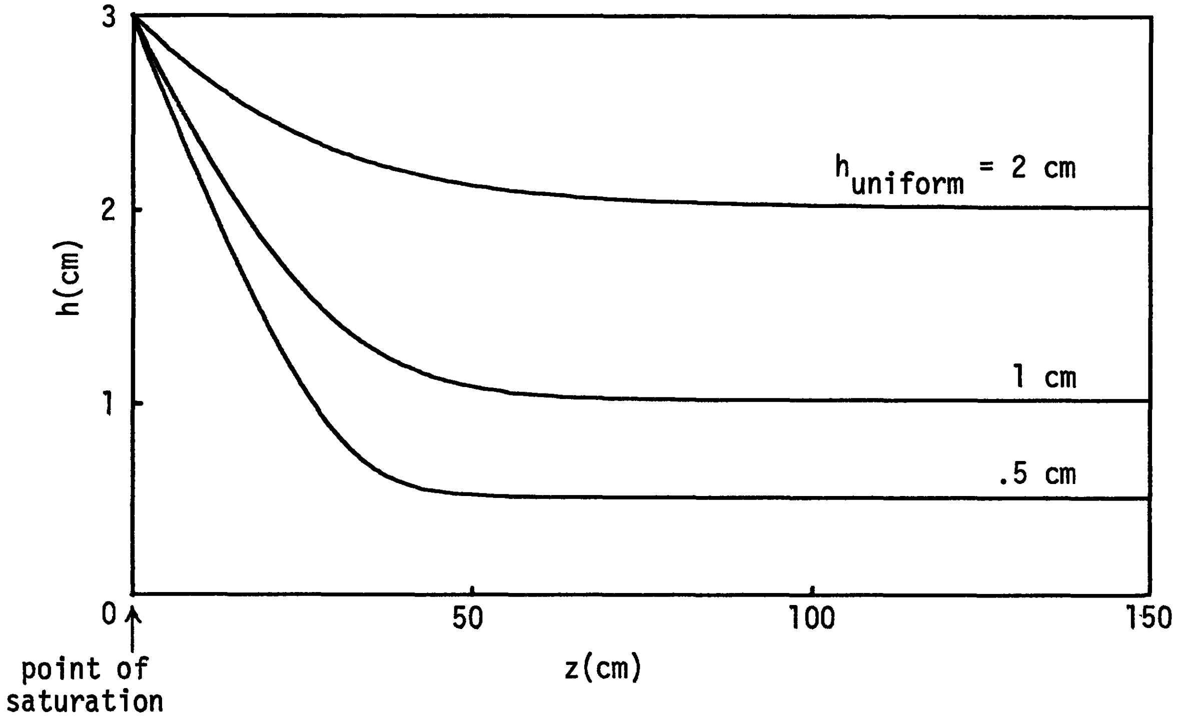

Fig. 5.7 Profiles of uniform flow with a saturated end condition

---

[*] The simple height-constraint boundary condition is only an approximation to the real condition. At a distance from the boundary that is on the order of the flow height, the quasi-one-dimensional model breaks down. Although the flow details near the boundary is not of concern in the examples of this chapter, these details can show how realistic the boundary conditions for the quasi-one-dimensional model is.

integrated to yield

$$\frac{h_u^2 - h^2}{2} = \frac{q}{\rho g K_z} z \qquad (5.24)$$

The maximum flow, q_{max}, that is allowed by the conductor for a given L occurs when $h_u = h_o$ and $h_L = 0$:

$$q_{max} = \frac{2\rho g K_z h_o^2}{L} \qquad (5.25)$$

This result will be used in section 6.3.2.

5.4.1.2.2 $\alpha = 0$, q' Constant

Under these conditions, (5.20) reduces to

$$\frac{d^2}{dz^2} h^2(z) = -\frac{2q'}{\rho g \beta K_z} \qquad (5.26)$$

This can be recognized as a steady state one-dimensional diffusion equation involving $h^2(z)$ with a distributed source. The physical significance of the $\rho g \alpha$ and the $\partial hp^*/\partial z$ terms in the force equation (5.3) now becomes clear; the former term represents a bulk force dependent only on the angle of incline while the latter represents a diffusion force dependent only on variations of the flow height.

Integration of (5.26) yields

$$h^2(z) = \frac{-2}{\rho g K_z} [q'z^2 + b_1 z + b_2] \qquad (5.27)$$

where b_1 and b_2 are constants to be determined. Figure 5.8 shows a physical situation corresponding to this case. With the boundary condition at z = 0 and L being identically h = 0 (an idealized situation),

$$h^2(z) = \frac{2q'}{\rho g K_z} z(L-z)$$

and

$$h_{max}^2 = \frac{q'L^2}{2\rho g K_z} \qquad \text{at } z = L/2 \tag{5.27a}$$

Thus for a given q', saturation occurs at the midpoint of the section if $h_{max} = h_o$.

5.4.1.3 Transient Drainage

Time dependence is incorporated by the addition of $n_e \frac{\partial h(z,t)}{\partial t}$ to (5.20)

$$n_e \frac{\partial h}{\partial t} + \frac{\partial}{\partial z} h K_z[\rho g \alpha(z) - \frac{\partial}{\partial z} \rho g \beta h] = q' \tag{5.28}$$

To completely specify the problem, an initial condition expressed by $h(z,0) = h_i(z)$ is needed together with two boundary conditions. Since the practical transient cases of interest are those after any liquid addition has stopped, q' is set equal to zero. Also, to avoid cumbersome mathematics, α is considered constant.

In (5.28), the effects of gravity and diffusion are clearly distinguished. For example, if the last term on the left hand side is neglected, the remaining terms form the first order wave equation, the general solution of which is

$$h(z,t) = f(z - v_o t)$$

where f is an arbitrary function and $v_o = \frac{\rho g \alpha K_z}{n_e}$. Thus, under the effect of gravity, the initial profile tends to maintain itself, but moves as a whole with a velocity v_o down the incline. On the other hand, if α is zero, then a nonlinear diffusion equation remains.

Indeed, in a frame of reference moving with velocity v_o, (5.28) becomes

$$n_e \frac{\partial h}{\partial t'} + \frac{\partial^2}{\partial z'^2} \rho g \beta \; K_z \frac{h^2}{2} = 0 \tag{5.29}$$

where $t' = t$, and $z' = z + v_o t$ are the moving frame coordinates. The solution of (5.29) is still difficult to find. Although linearization can reduce (5.29) to the linear diffusion equation which has well documented solutions(32), this procedure is valid only for perturbations. From an engineering point of view, it is more fruitful to show dimensionally that diffusion is of secondary importance.

Consider the hypothetical profile shown in Fig. 5.9. Initially, a sharp boundary at $z = 0$ separates the saturated and the dry zones. Then as t increases, the line of separation moves with velocity v_o, and simultaneously diffusion acts to smooth out the transition region. The action decreases as the transition becomes smoother, and the transition region spreads with less rapidity. Thus, at large t, the saturated region will appear to shrink with velocity v_o.

To put this qualitative discussion on more solid ground, let us compare the ratio of the third term to the second term of (5.28)

$$\frac{\partial}{\partial z} vh \approx \frac{V_o h_o}{T}$$

$$\frac{\partial^2}{\partial z^2} \rho g \beta K_z \frac{h^2}{2} \approx \frac{V_o}{2} \left(\frac{\beta}{\alpha}\right) \left(\frac{h_o}{T}\right)^2$$

$$\text{ratio} = \frac{1}{2} \left(\frac{\beta}{\alpha}\right) \left(\frac{h_o}{T}\right)$$

where T is the length of the transition region. For a slope of 6°, (β/α) is approximately 10. The diffusion term becomes insignificant if $h_o/T = O(10^{-2})$, which is almost always satisfied in the transmission line geometry. Thus for a section of conductor of length $L (L >> h_o)$ that is initially saturated, the time to reach an unsaturated state is roughly L/v_0, provided there is no liquid added.

For $\alpha = 0$, Boussinesq derived an exact solution of (5.28) for certain initial profiles(27), the solution being in the form of

$$h(z,t) = h_0(z)/(1+t/t_0)$$

where t_0 is a characteristic time dependent on properties of the medium and the initial profile.

5.4.2 $\kappa \geq 1$

When the hydrostatic limit does not apply, (5.3), (5.4) and (5.13) must be solved simultaneously. In general, numerical techniques such as the finite difference method must be employed. The example below shows the applicability of the criterion, $\kappa << 1$, governing the use of the hydrostatic approximation.

For a steady state problem with q' and α equal to zero, the three equations can be reduced to one equation. First, (5.3) is replaced by

$$q = - K_z \frac{dp^*h}{dz}$$

where q is considered given. Then integrating this equation and substituting the result into (5.13),

$$\frac{dh}{dz} = \frac{3K_x}{q} \left| \frac{(hp^*)_0 - qz/K_z}{h} - \frac{\rho g h}{2} \right| \tag{5.30}$$

where $(hp^*)_0 = hp^*(z=0)$. By constraining q, h, and p^* (or $\frac{dh}{dz}$) at $z = 0$, this equation can be numerically integrated. Figure 5.10 gives several profiles with K_x as the varying parameter. For $K_x > 3 \times 10^{-5}$ cc-sec/gm, a limiting profile is clearly approached. The parameters in this example were chosen

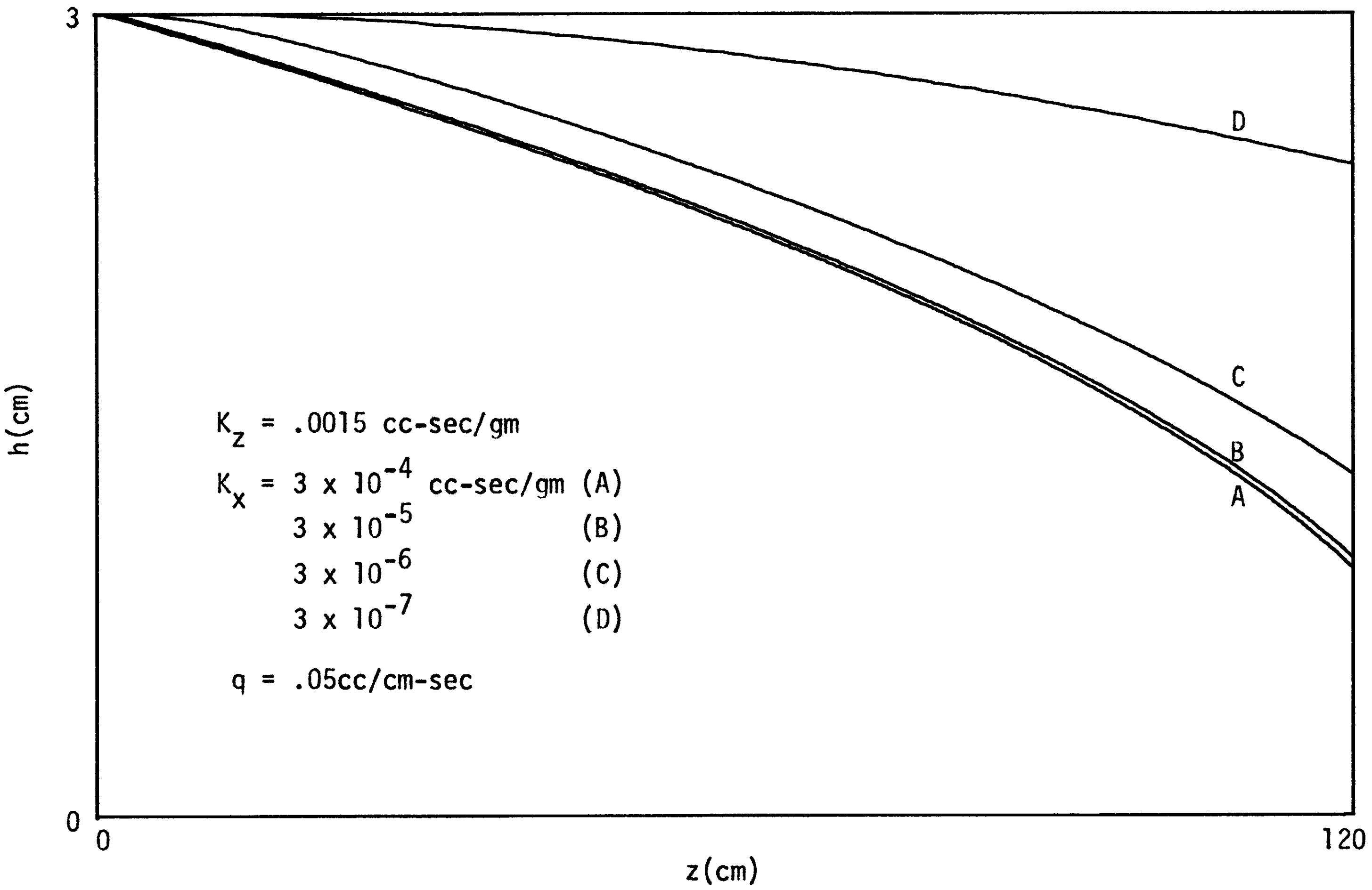

Fig.5.10 Calculated profiles showing the effect of varying K_x (q', $\alpha = 0$)

to match the experiments to be discussed later. Using these parameters, and with $v_o = q/h_o$, $p_o^* = \rho g \beta h_o/2$

$$\kappa = \frac{V_o h_o^2}{3Lp_o^* K_x} \approx 1$$

and the validity of the criterion is demonstrated.

CHAPTER 6

EXPERIMENTAL CASE STUDIES OF FLOW IN A STRANDED BUNDLE

6.1 Aims

Gravity-induced flow was experimentally investigated in a stranded bundle similar to the stranded conductor of Chapter 4. Besides furnishing test data as a basis to evaluate the theoretical model developed in Chapter 5, the results gave quantitative knowledge as to the efficiency of an actual absorbent transmission line span in transporting water by the action of gravity. The very important effect of wicks on the internal flow was also tested.

The preceding theoretical analysis distinguishes two forces that promote flow (see section 5.4.1.2) although both forces are ultimately derived from the gravitational field. The gravitational force, as represented by $\rho g \alpha$ in (5.3), depends on the local angle of incline of the flow structure while the diffusive force, as represented by $\partial hp^*/\partial z$ in (5.3), derives from the natural tendency of the flow to achieve constant height. In general both of these forces act simultaneously. At the upper sections of a transmission line span the gravitational force is expected to dominate; at the horizontal midsections, only the diffusive force can cause flow, but only if wicks are employed to impose variations in the flow height. The flow experiments performed were an attempt to evaluate the effects of these forces separately.

6.2 Experimental Setup

The chief problem in the experiments lay in the difficulty of observing h or v. However, the pressure at the bottom of the flow structure, p_b, was monitored using simple manometers. Since p* was deduced from p_b

using theoretical results, the check on the model based on correlation of theoretical experimental results was somewhat weakened.

A 6-foot stranded structure similar to the test conductor described in Chapter 4 was used as the flow model. For simplicity, the bundle had a rectangular cross section with no twisting; its cross-sectional geometry is shown in Fig. 6.1 along with the positioning of a manometer. The height of the bundle was chosen to be 3cm since measurements showed that this structure was capable of supporting a water column of this height. That is, for the hydrostatic case, when saturationwas indicated with the meniscus in the manometer parallel to the bottom of the bundle, the interior of the bundle was completely filled with water.

Figure 6.2 illustrates the experimental setup. With the flow rate monitored by a rotometer, water was added to the bottomside of the bundle at the upper end via a 2mm diameter tube. A wicking section was placed at the lower end to drain away the water, thus preventing saturation there. The reason for doing this will be discussed later.

During the course of experimentation, the results were found to depend strongly on the preparation procedure. Some preliminary testing using glass rod bundles showed that air bubbles were easily trapped but that they can be minimized by prewetting the rod surfaces. The procedure adopted in the experiments was to initially immerse the test bundle and then to carefully drain it so that the rod surfaces were prewetted but the channels were completely empty. In this way reasonable repeatability was achieved.

6.3 Measurement of Permeability

Permeability was measured using the apparatus illustrated in Fig. 6.3.

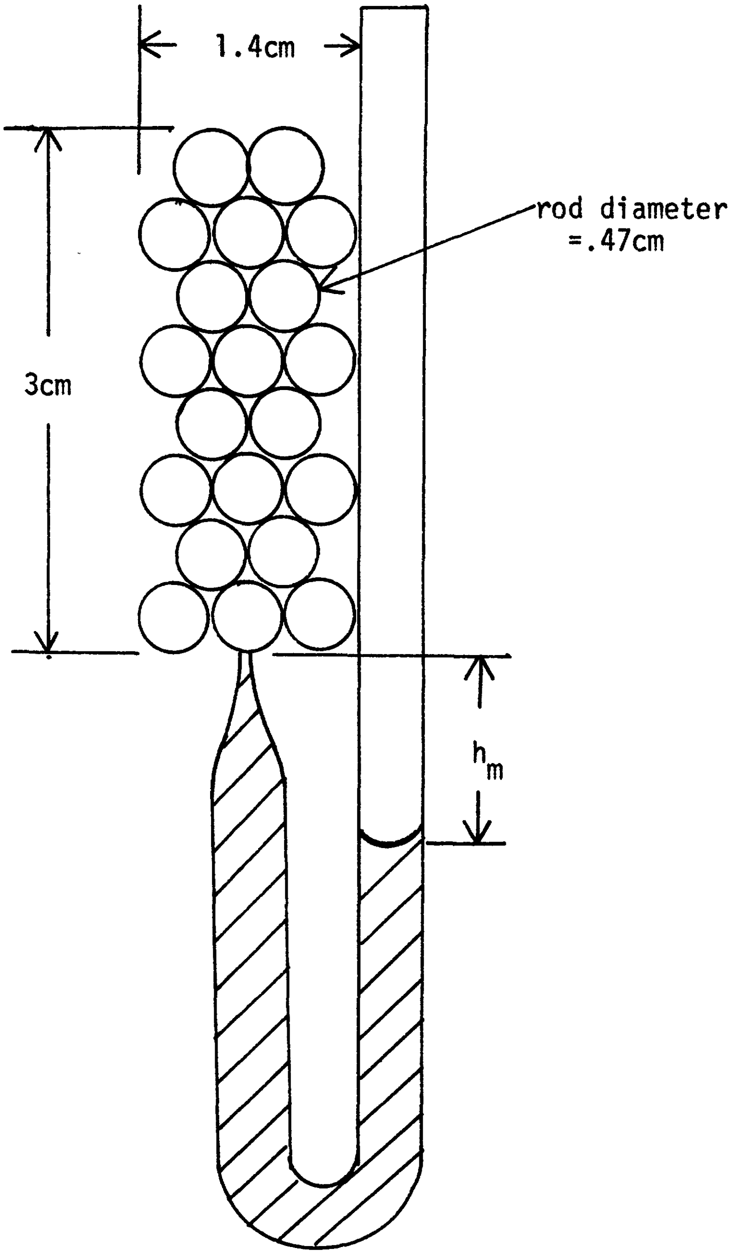

Fig.6.1 Cross-sectional diagram of test bundle showing position of manometer

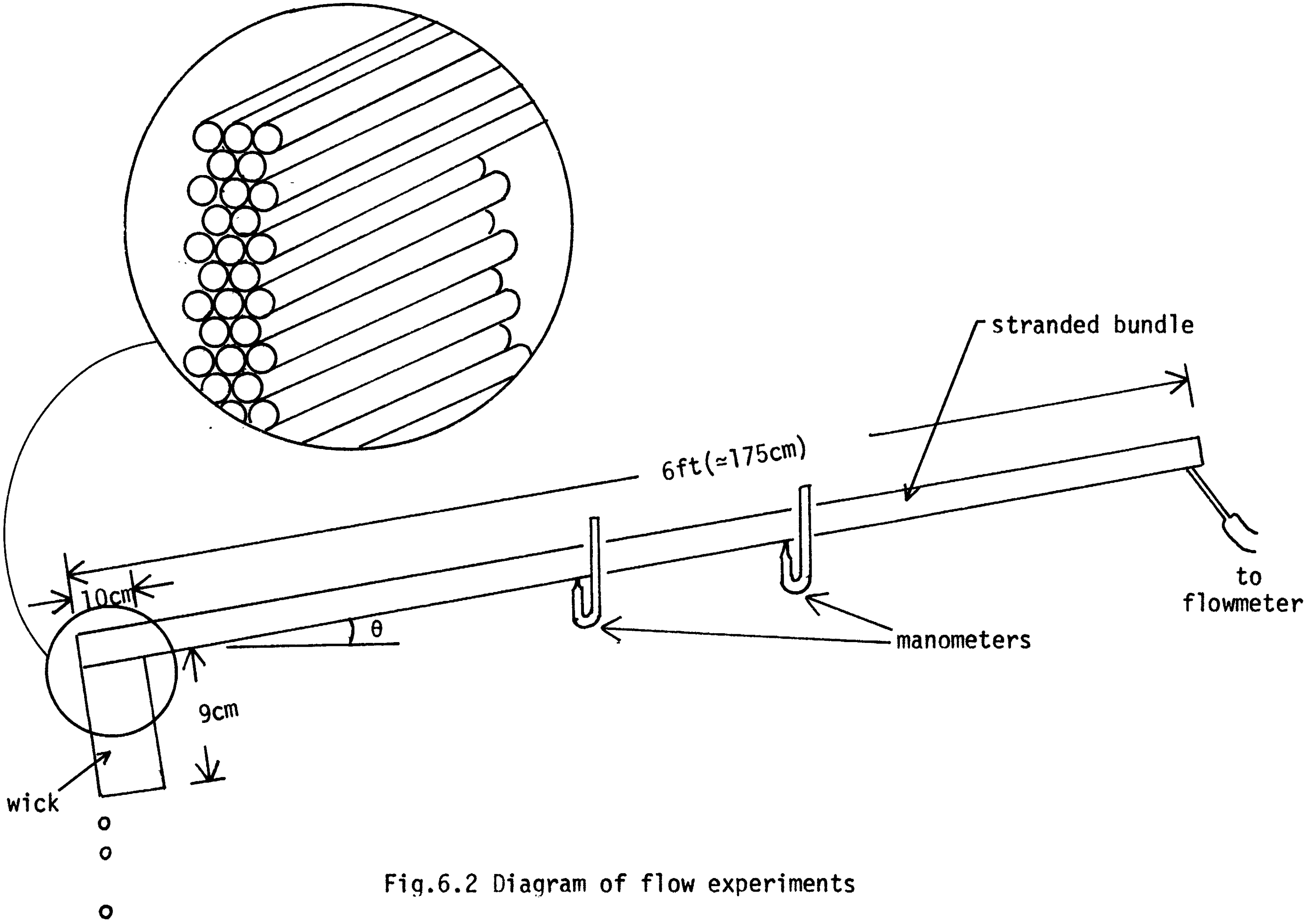

Fig.6.2 Diagram of flow experiments

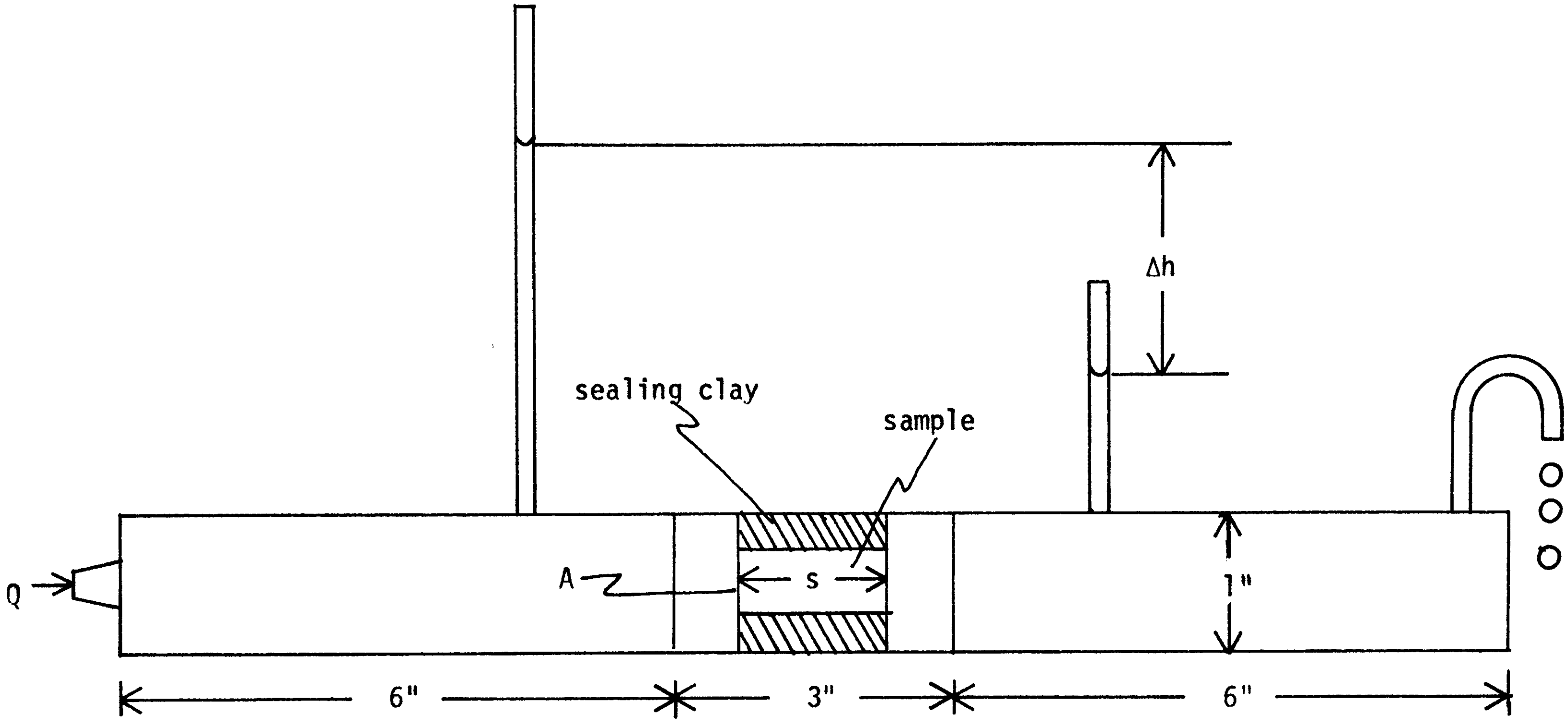

Fig.6.3 Diagram of apparatus for permeability measurements

The flow rate Q and the difference in height of the water column in the upstream and downstream manometers, Δh, were measured and the permeability was calculated using

$$K = \frac{Qs}{\rho g A \Delta h} \tag{6.1}$$

where A and s are respectively the sample area perpendicular to the flow and the sample length along the flow. This definition of K is compatible with (5.3) and with the averaged velocity.

Table 6.1 lists the longitudinal and transverse permeabilities of stranded bundles consisting of smooth or grooved strands. The grooved rods were cut with a 32 thread/inch die and the depth of the grooves was approximately .5mm. As expected, the longitudinal permeability was essentially independent of the smoothness of the rod surface, thus giving evidence to the occurrence of laminar flow. The transverse permeability, however, showed orders of magnitude difference between the smooth and the grooved rods.

	longitudinal (K_z)	transverse (K_x)
smooth rods	.0017	4.1×10^{-6}
grooved rods	.0013	1.5×10^{-4}

Table 6.1 Table of Measured Permeabilities (in cc-sec/gm)

In measuring the transverse permeability of the grooved bundle, the grooved strands were separated by smooth strands so that complete interlocking of grooves between strands was avoided. For the 6-foot grooved bundle, some interlocking of the threads occurred, but there was sufficient variations in the threads to ensure that complete interlocking along the entire length did not result. Hence the measured transverse permeability should at least have the right order of magnitude. The finite permeability measured for a smooth-stranded bundle was probably due to slight fluctuations in the rod diameter and to looseness in the packing of the sample.

To lend confidence to these measurements, we can roughly calculate a longitudinal permeability for this geometry. Approximating the channels as cylindrical cavities as illustrated in Fig. 6.4, a channel permeability, $k_c = .000156\text{cm}^2$ can be calculated using (3.6). The permeability as defined in our model is related to this channel permeability by

$$K_z = n_e k_c / \mu$$

where n_e is the pore volume ratio and μ the viscosity of water. A pore volume ratio of .094 can be easily derived for the close-packed cylinder geometry, and with $\mu = 10^{-2}$ gm/cm-sec, the permeability is calculated to be

$$K_z = .0015 \text{ cc-sec/gm}$$

which compares extremely well with the measured values.

6.4 Gravity Flow

For long channels with a constant angle of incline, free surface viscous flows tend toward a uniform state (i.e., constant height). Significant deviations from this uniform flow will occur for a limited region next to the upstream and downstream boundaries in order to satisfy conditions imposed there. In this set of experiments uniform flow was achieved in a 6-foot section for the boundary conditions. If the flow becomes uniform in a distance that is small compared to the transmission line span length, then it can be concluded that at least for low rates of

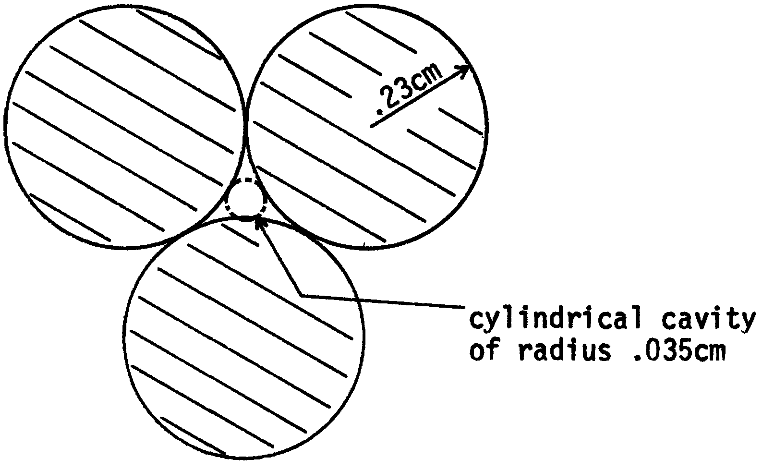

Fig.6.4 Approximating the interstice as a cylindrical pore

liquid influx uniform flow applies to any segment of interest whose angle of incline is approximately constant. Low rates of liquid influx means that the total fluid added to the segment from the outside is small compared to the rate of flow coming into the segment from its upper boundary.

Based on the analysis of section 5.4.2 and the measured transverse permeability, flow in the grooved bundle is expected to be in the hydrostatic regime. Hence the experimental results are compared with the simplified hydrostatic equations as given in section 5.4.1. Manometers placed periodically along the bundle gave the profile of h_m, as defined in Fig. 6.1, which is related to p_b by

$$p_b = p_o - \rho g h_m \tag{6.2}$$

In the hydrostatic limit, $p_b = p_c + \rho g \beta h$ where h is the theoretical free surface height (note that p_c is reintroduced here since p_b is now related to p_o). Since the height of the bundle, h_o, was chosen such that $p_c = p_o - \rho g \beta h_o$, h and h_m are related by

$$h = h_o - h_m \tag{6.3}$$

where β, being close to 1 for the cases of interest, is not shown. Equation (6.3) will be used in the comparison of theory and experiment.

The typical profiles of h_m are shown in Figs. 6.5 - 6.8 for various angles of incline. In spite of the fluctuations, these profiles indicate that uniform flow did in general occur over a substantial section of the bundle and that boundary conditions caused pronounced deviations from uniform flow only for regions extending about 50cm away or less.

Using this data the uniform flow height versus the flow rate can be plotted with the angle of incline as a parameter. The results, as given

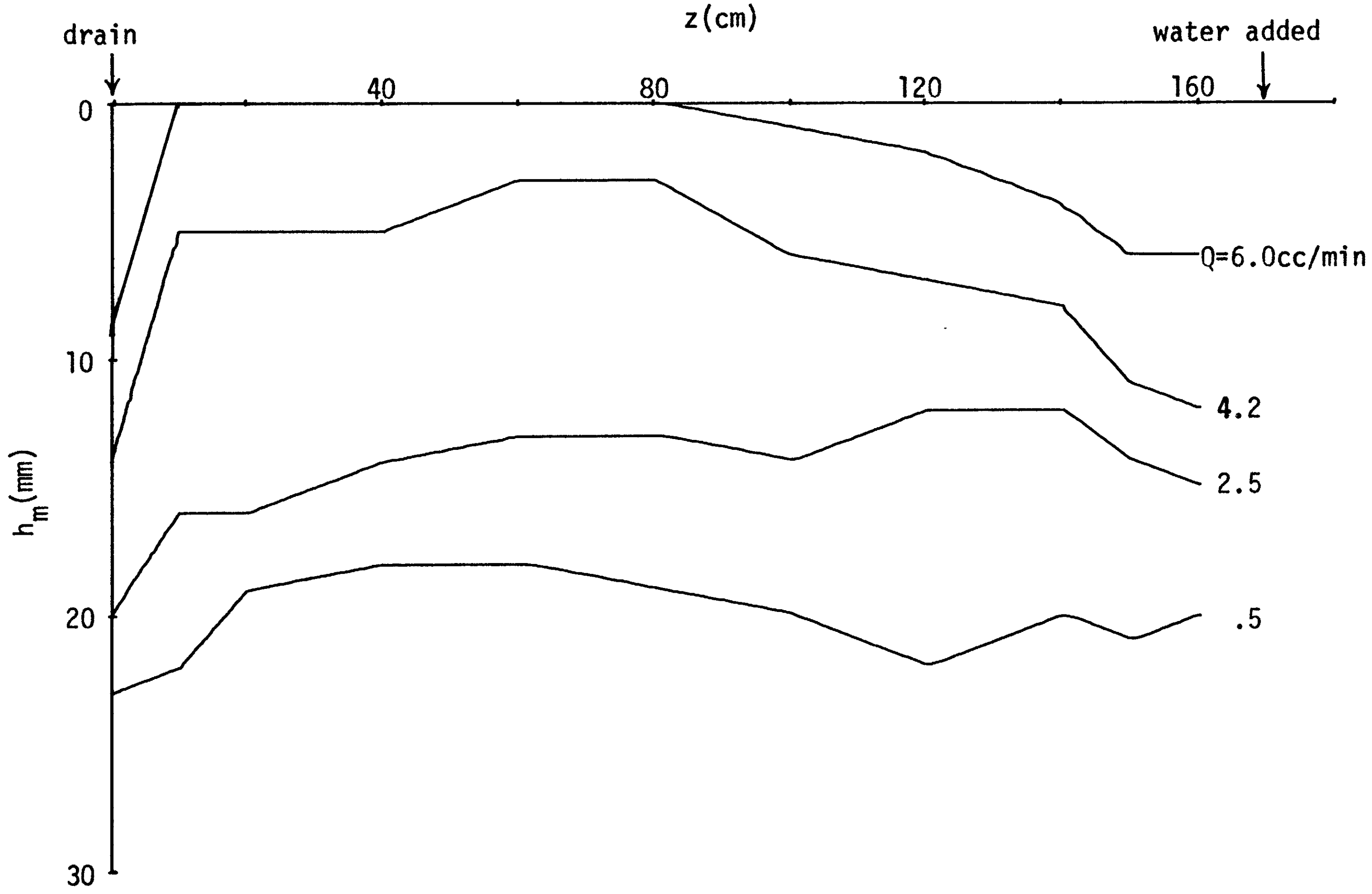

Fig.6.5 Profile of h_m for $\theta=2^o$

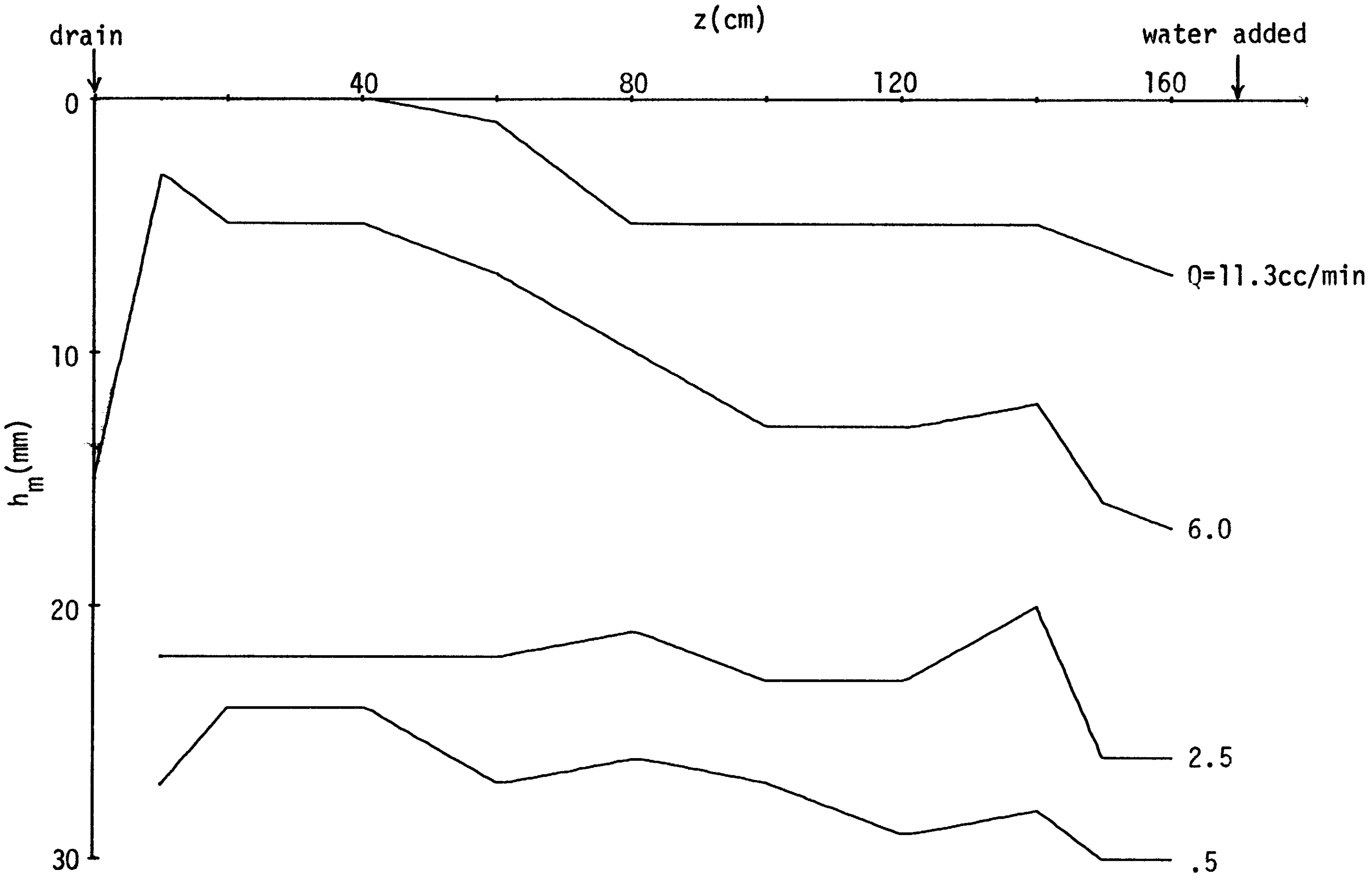

Fig.6.6 Profile of h_m for $\theta=4^o$

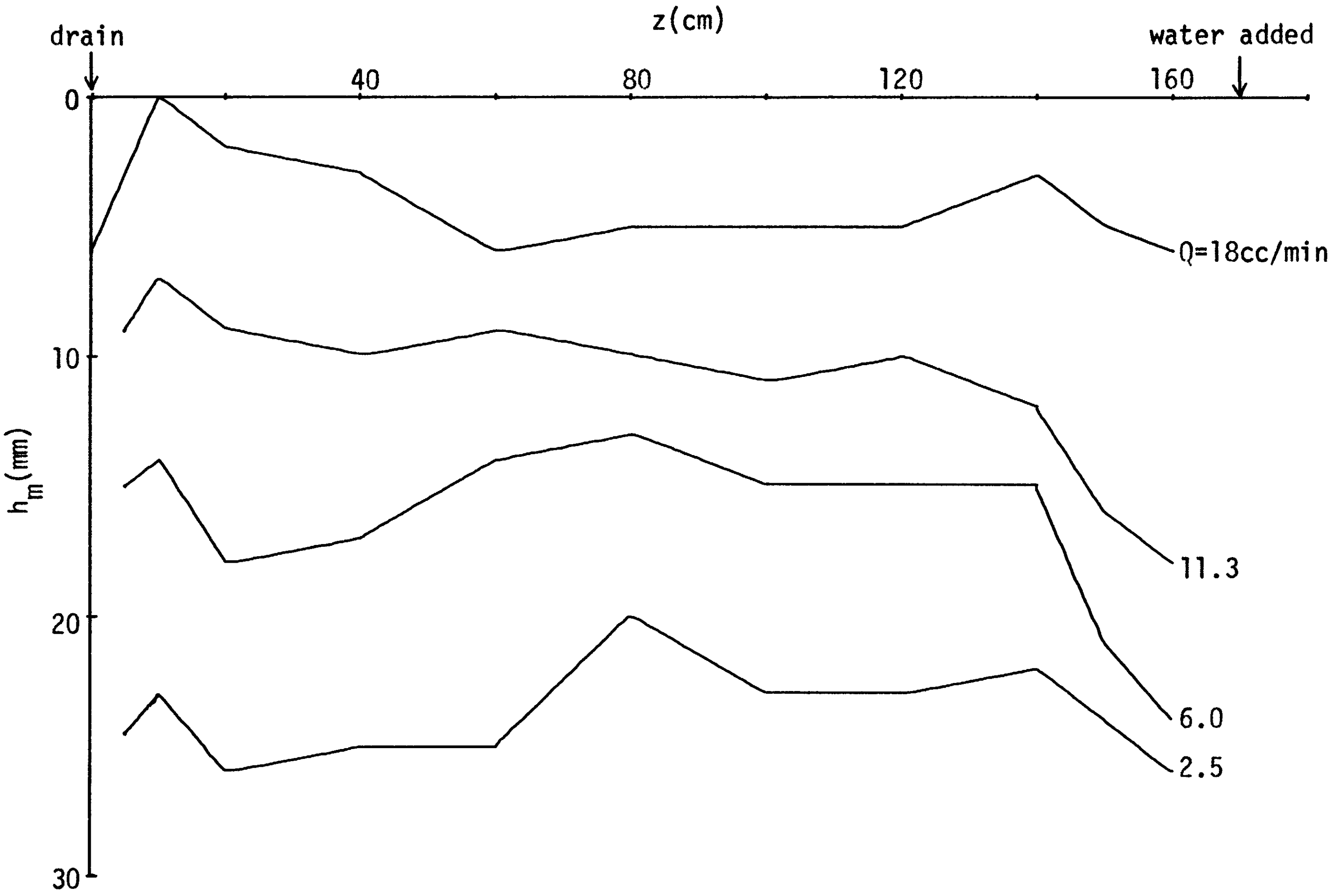

Fig.6.7 Profile of h_m for $\theta=6^o$

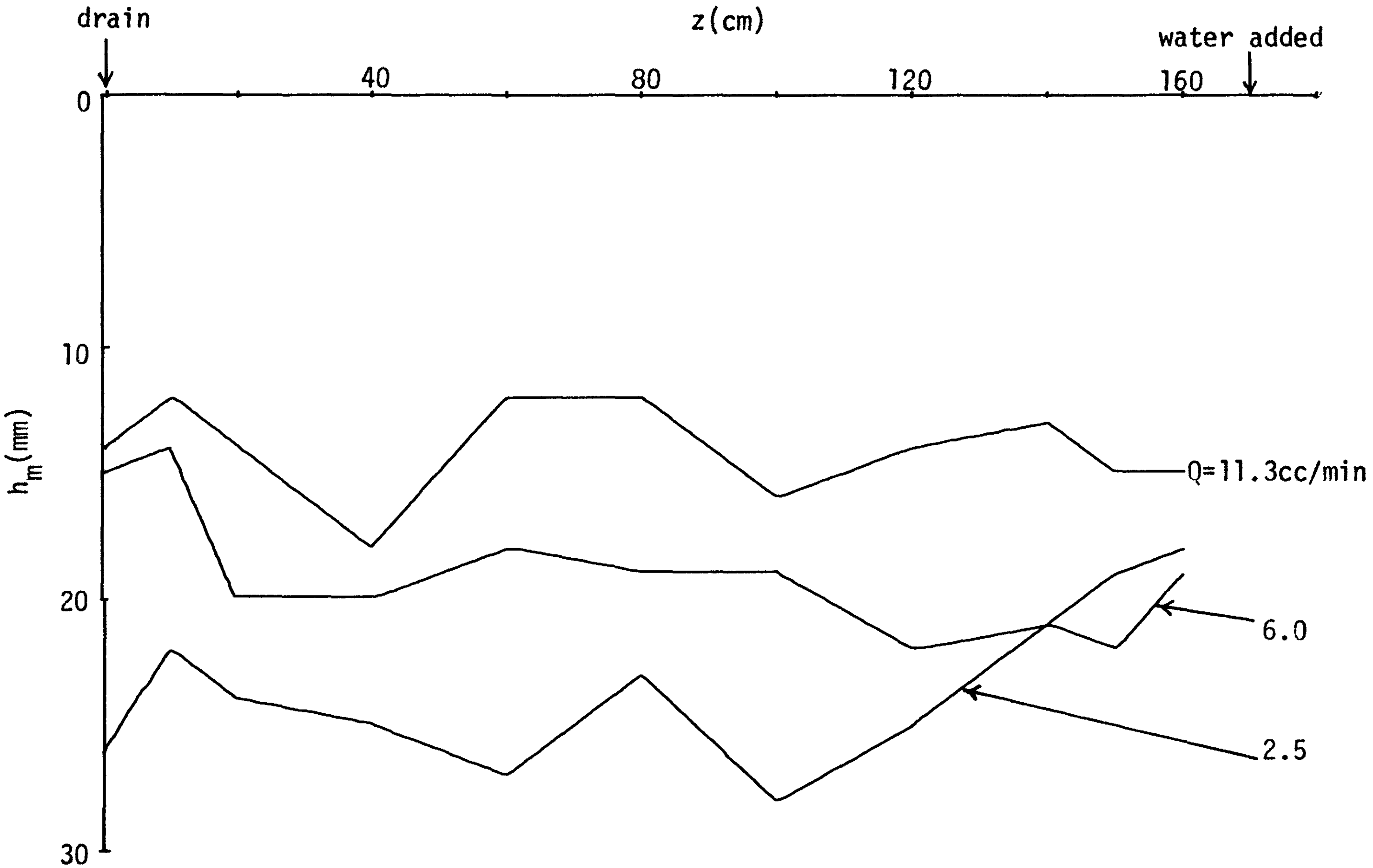

Fig. 6.8 Profile of h_m for $\theta=8^o$

in Fig. 6.9, show a linear dependence in agreement with the model prediction given by (5.19). Quantitative comparison to (5.19) can be made by considering the dependence of the maximum flow rate, q_{max}, on the angle of incline. In Fig. 6.10, the theoretical curve was obtained by letting $h = h_0$ and using the measured value of K_z. Because the measured q values at near saturation includes the unwanted effect of flow occurring on the outside of the bundle, the experimental values of q_{max} were obtained by projecting the linear portions of the h vs. q curve to the q axis. Close agreement is shown for the θ's tested.

Although the above results support the validity of the theoretical model, in other respects the experiments showed substantial deviation from theoretical prediction. For example, an apparent hysteretic effect was present when the flow rate was changed. Figure 6.11 shows the profiles of h_m for $\theta = 6°$ both for increasing flow rate and for decreasing flow rate. Fairly close correspondence existed for the very low and the very high rates, but for intermediate rates (Q = 11.3cc/min in Fig. 6.11), pronounced differences occurred in the profiles. The same sort of behavior was recorded for other values of θ as well.

As another example of the deviation from theoretical prediction, consider the profile near the downstream boundary. Assuming that the height at the lower boundary is at one-half of the height at uniform flow, then the theoretical profile can be easily derived using (5.22). The results are given in Fig. 6.12 for the angles of incline under consideration, and (6.3) allows direct comparison of Fig. 6.12 to Figs. 6.5 - 6.8. The correspondence is rather poor.

A likely cause of these discrepancies was that the constant-pressure free surface assumption was violated by two possible effects. In one

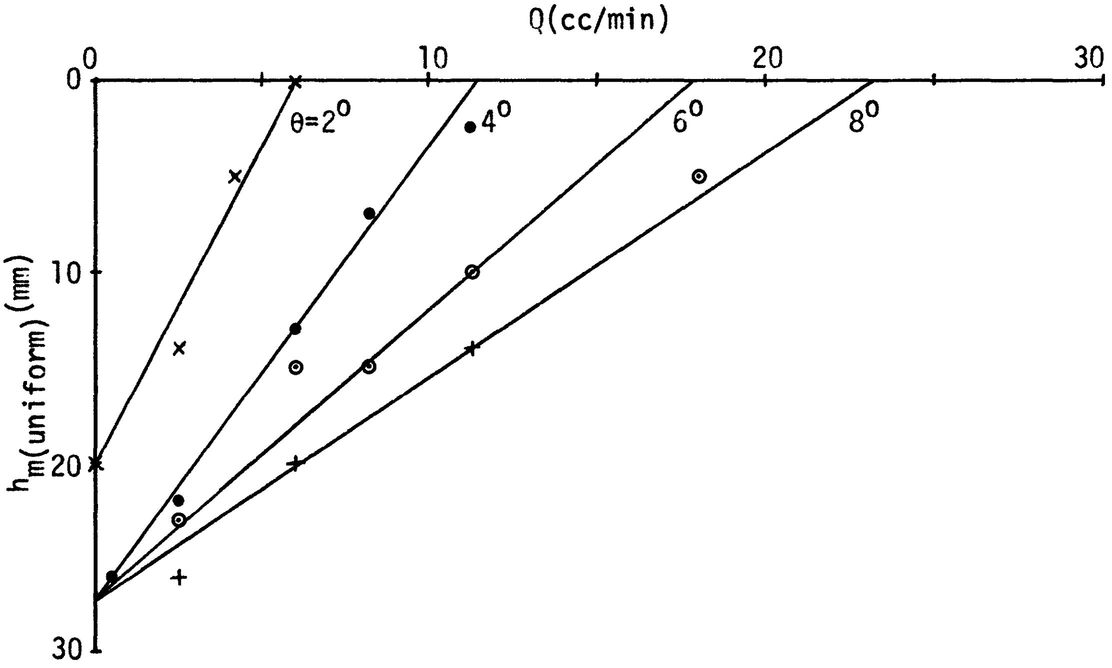

Fig. 6.9 Graph of h_m of uniform flow vs. flow rate

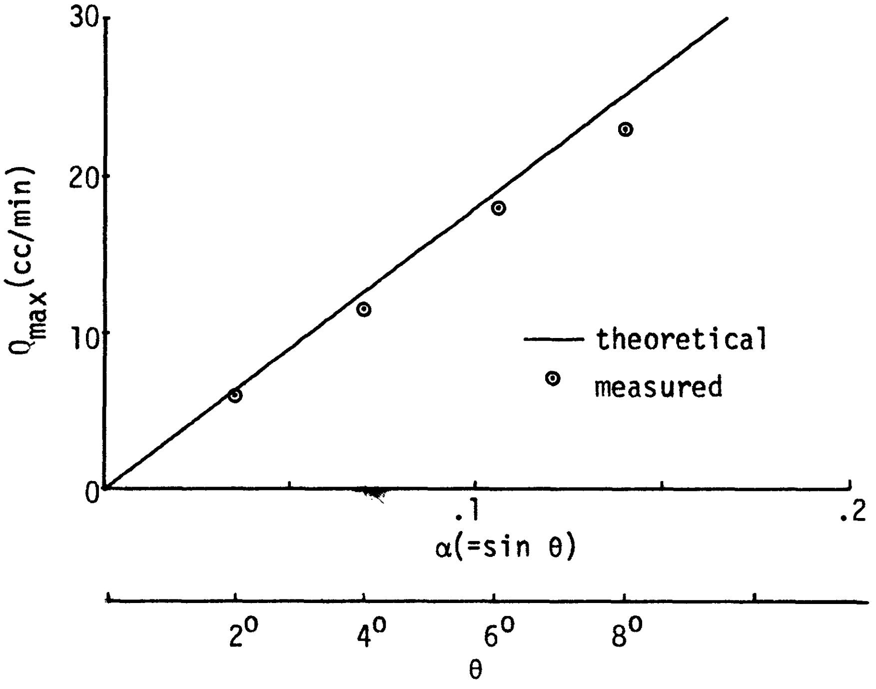

Fig. 6.10 Graph of maximum flow rate vs. angle of incline

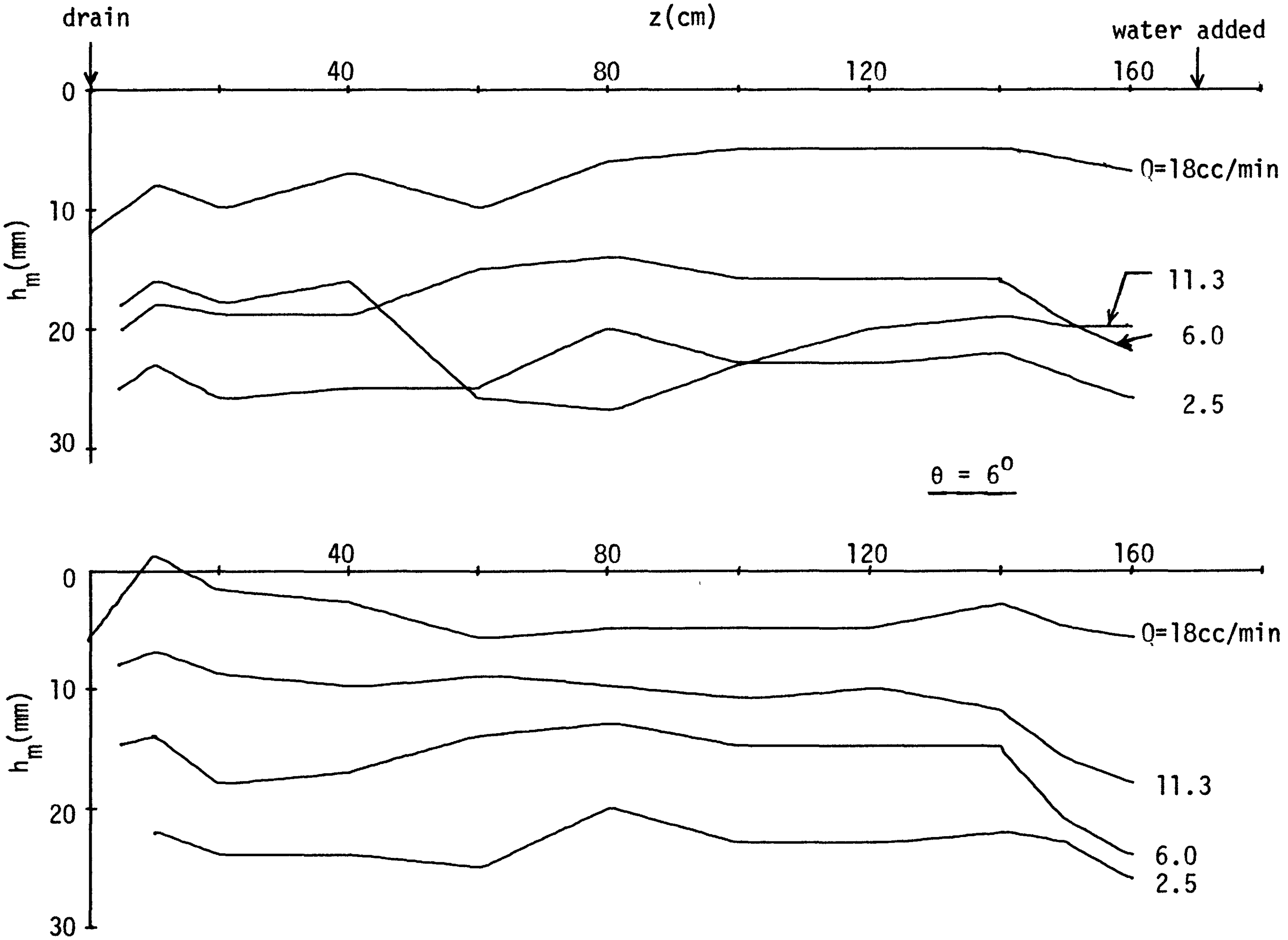

Fig. 6.11 Apparent hysteresis in the flow profile
upper graph: high flow rate → low flow rate
lower graph: low flow rate → high flow rate

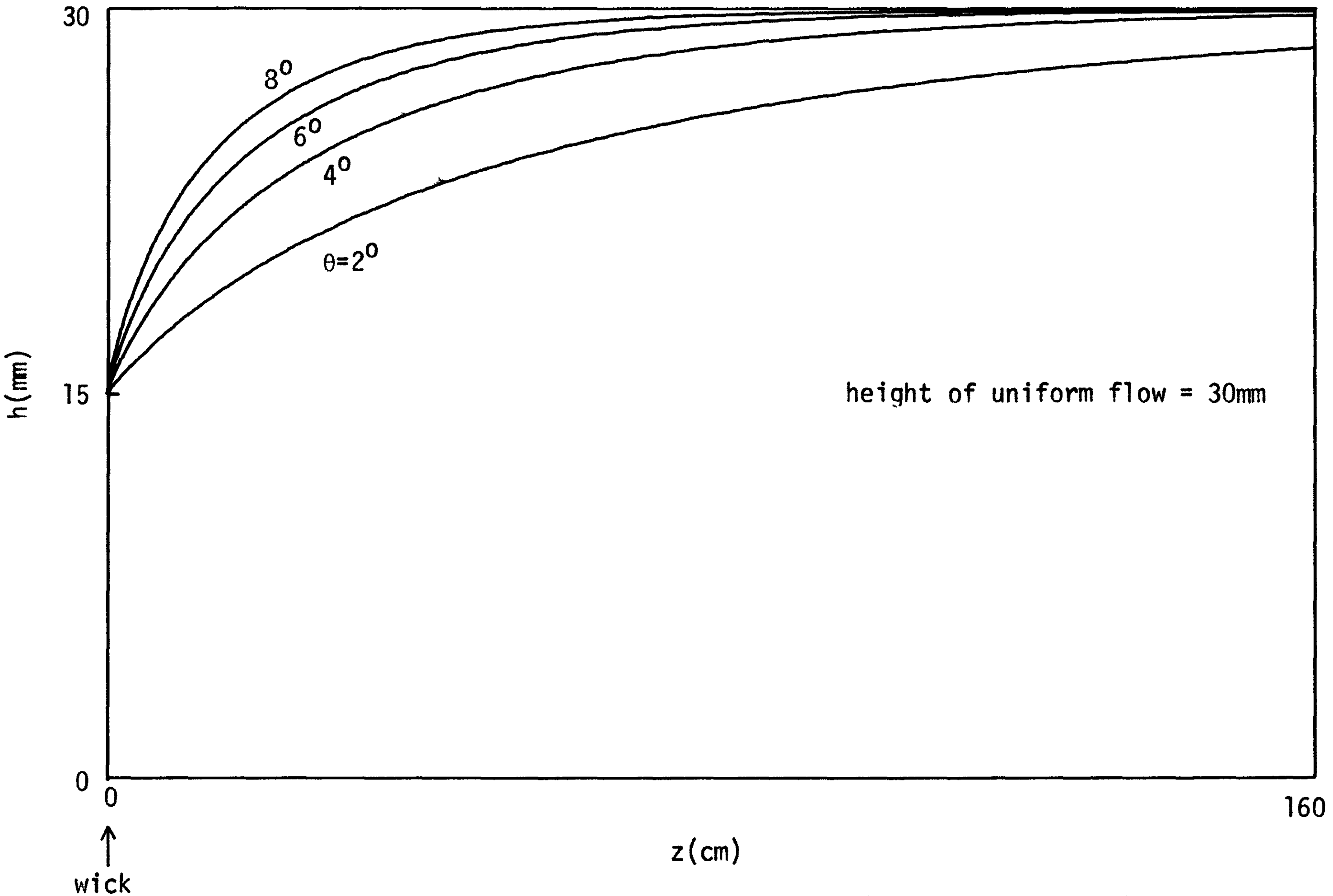

Fig. 6.12 Theoretical profile near a wick(hydrostatic limit)

effect the formation of menisci between adjacent strands caused the interstitial space to become effectively an enclosed channel with movement of air allowed only through the ends. If somehow both ends of a region were clogged, then depending on whether water or air was trapped inside, either a closed-pipe flow situation or an entrapped air bubble would result. Consider for example the possible flow case shown in Fig. 6.13. The hypothetical flow profile is one that would apply if the free surface condition were strictly adhered to. The flow height rises to saturation level at the lower end if the structure were simply terminated there with the pressure constrained to be atmospheric. The rise at the upper end could be due to some liquid input condition. Even if the hypothetical profile were reached somehow, it is clear from the figure that the free surface at the uniform flow region cannot change freely to accommodate changes in the flow rate since the channels immediately above and below the free surface are entirely enclosed.

The other possible effect causing deviation from the constant-pressure free surface hypothesis was the formation of a meniscus separating air and liquid in a particular channel as illustrated in Fig. 6.14. The assumption of a fixed free surface pressure takes into account only the curvature of the meniscus in the transverse direction. Ignoring the curvature in the other direction is possible only for uniform or near uniform flows. When changes in height occurs as in Fig. 6.14, then the longitudinal curvature becomes significant at the air-liquid interface. The free surface pressure then can take on, in an averaged sense, a value between $(p_o - \gamma/r_c)$ and $(p_o - 2\gamma/r_c)$ depending on the rate of change in the height and also on the contact angles of the menisci formed.

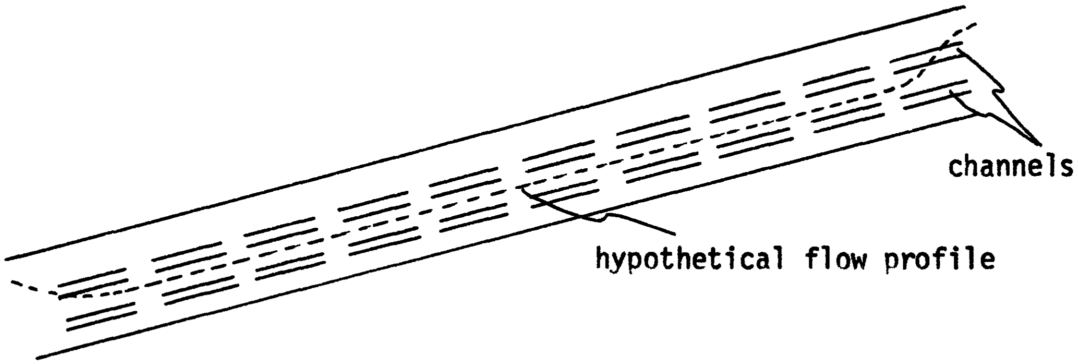

Fig. 6.13 A possible flow situation

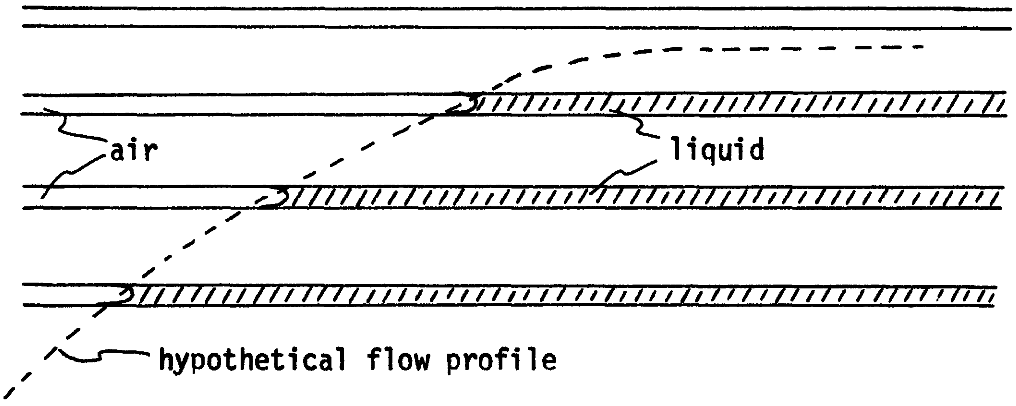

Fig. 6.14 Diagram of air-liquid interface in nonuniform flow

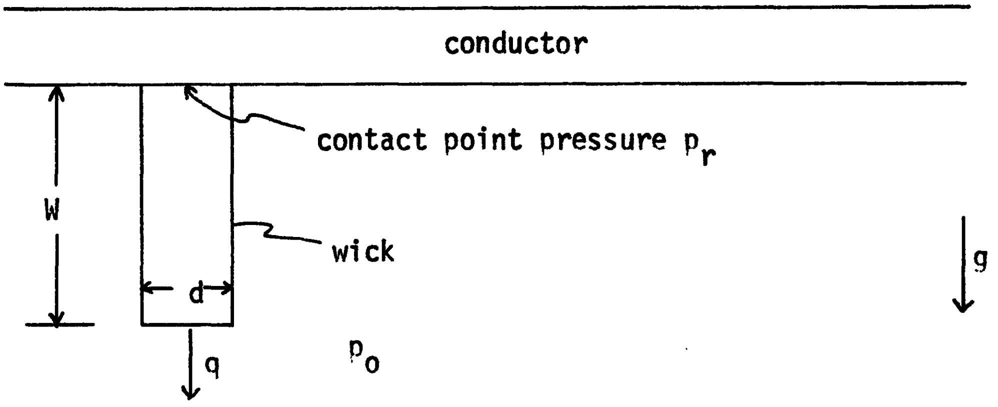

Fig. 6.15 Diagram of a wick

In these experiments the first effect was avoided to some extent by using a wick at the lower end. Since saturation was prevented there, air was allowed to enter into the interior parts of the bundle. The second effect is believed to cause the apparent hysteretic results. When the flow rate decreases, the top-most channel could continue to participate in the flow until its pressure becomes significantly below $p_o - \gamma/r_c$, the hypothetical free surface pressure. To minimize this effect, the profiles shown in Figs. 6.5-6.8 were taken with increasing flow rate.

6.5 Wicking and Horizontal Drainage

These experiments simulated flow at the horizontal midsection of the transmission line span where drainage must be accomplished by wicking. Up to now the wick was simply treated as a means of keeping a fixed pressure, or equivalently a fixed flow height in the hydrostatic limit, at some point on the conductor. A more detailed look at the wicking process is now needed.

Any real wicking structure has flow dynamics of its own. When the wick is placed in contact with the absorbent conductor, the pressure and the flow rate at the contact point must consistently satisfy the flow equations of both the conductor and the wick. Thus a limit on the flow rate can be imposed by either the conductor or the wick.

To estimate a wick-imposed drainage limit, we note that the wick is itself a capillary structure and obeys flow equations similar to those for the conductor. Figure 6.15 shows schematically a wick in contact with the conductor. By assuming that the wick is filled with water, a condition for maximum drainage, the correct application of (5.3) gives

$$q = dK_w((p_r - p_o)/W + \rho g) \qquad (6.4)$$

where K_w is the wick permeability and the other quantities are as shown in Fig. 6.15. The pressure at the contact point, p_r, clearly cannot be greater than p_o; and for a liquid continuum to exist, p_r cannot be much less than p_c, the capillary pressure of the conductor. With (p_r-p_o) always negative, the largest value q can be is

$$q_{max(wick)} = \rho g K_w d \tag{6.5}$$

The wick length has little effect as long as $W >> (p_o-p_c)/\rho g$ and because $p_o-p_c \overset{\sim}{\sim} \rho g h_o$, W need not be much longer than the conductor height.

The conductor-imposed drainage limit can be easily estimated using (5.25),

$$q_{max(conductor)} = 2\rho g K_z h_o^2/L \tag{6.6}$$

where L is the distance between the wick and a point where saturation is maintained. Assuming that $L \geq 10h_o$, the ratio of the drainage limits can be taken,

$$\frac{q_{max(c)}}{q_{max(w)}} \leq \frac{K_z h_o}{5K_w d} \tag{6.7}$$

Thus if $K_z h_o/5K_w d << 1$, a condition easily met even without using excessively large wick dimensions, then the drainage is primarily conductor limited.

In practice, deviations from the theoretical drainage rate must be expected for the following reasons:

1) the height of the flow cannot be constrained to be zero; or equivalently $p_r < p_c$.

2) the wick will generally not be filled with water.

3) the contact region between the wick and the conductor has finite

area.

As shown in Fig. 6.2, the wick used in all the experiments was simply a 9cm long downward extension of the bundle composed of sections of 10cm long grooved rod. This choice allowed a good contact between the wick and the bundle. The wick was capable of maintaining a lower pressure in the bundle adjacent to the contact point than the internal pressure upstream. There was however a fairly strong dependence of the contact point pressure with flow rate as shown in Fig. 6.16.

In the horizontal drainage experiment, the bundle was kept saturated at a distance L away from the wick. Figures 6.17-6.19 compare the experimental profiles of h_m with the theoretical profiles of (h_o-h) calculated from (5.24). Close agreement is shown even for L as small as 15cm.

A more useful quantity to compare is the flow rate which was measured by collecting the water dripping from the wick. A theoretical flow rate can be calculated using (5.24) with z replaced by L and h by h_L and assuming a linear dependence of h_L with flow rate as shown in Fig. 6.16. The results shown in Fig. 6.20 give confidence to the use of the theoretical model in predicting drainage rates.

6.6 Transient Drainage

Section 5.4.1.3 showed that in transient drainage, a zone separating the saturated and the unsaturated sections moves down the incline of the flow structure with a velocity $v_o = \rho g \alpha K_z / n_e$. Diffusion effects were shown to be negligible if the separation zone length L is much greater than the structure height h. For drainage tests with the comparatively short test bundle, diffusion effects are in general expected to be

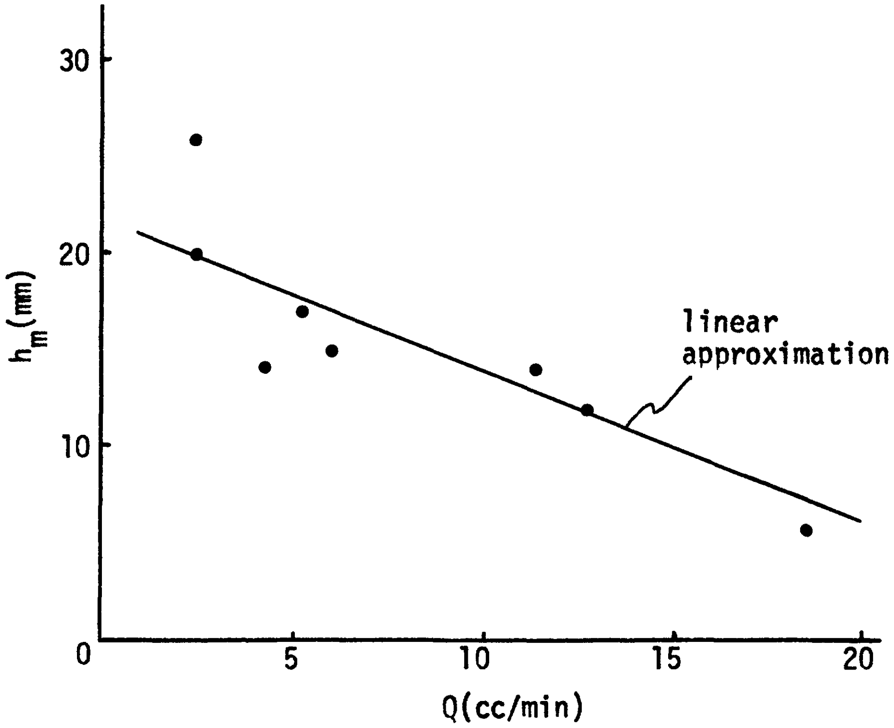

Fig. 6.16 Dependence of h_m adjacent to wick on flow rate

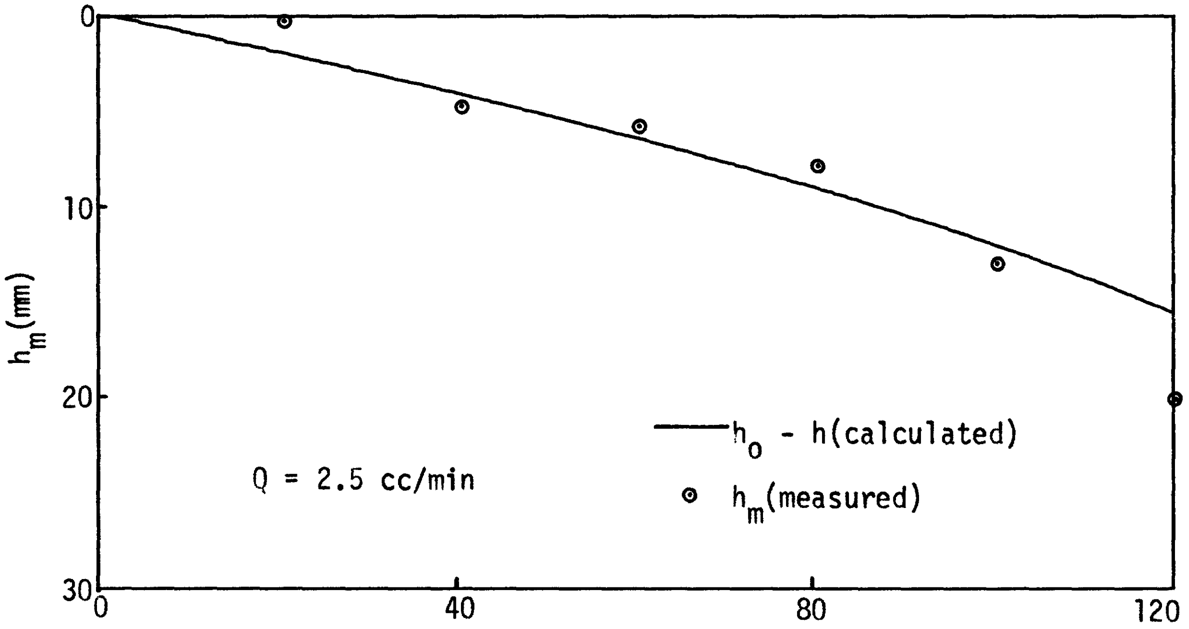

Fig. 6.17 Drainage profile for L=120cm

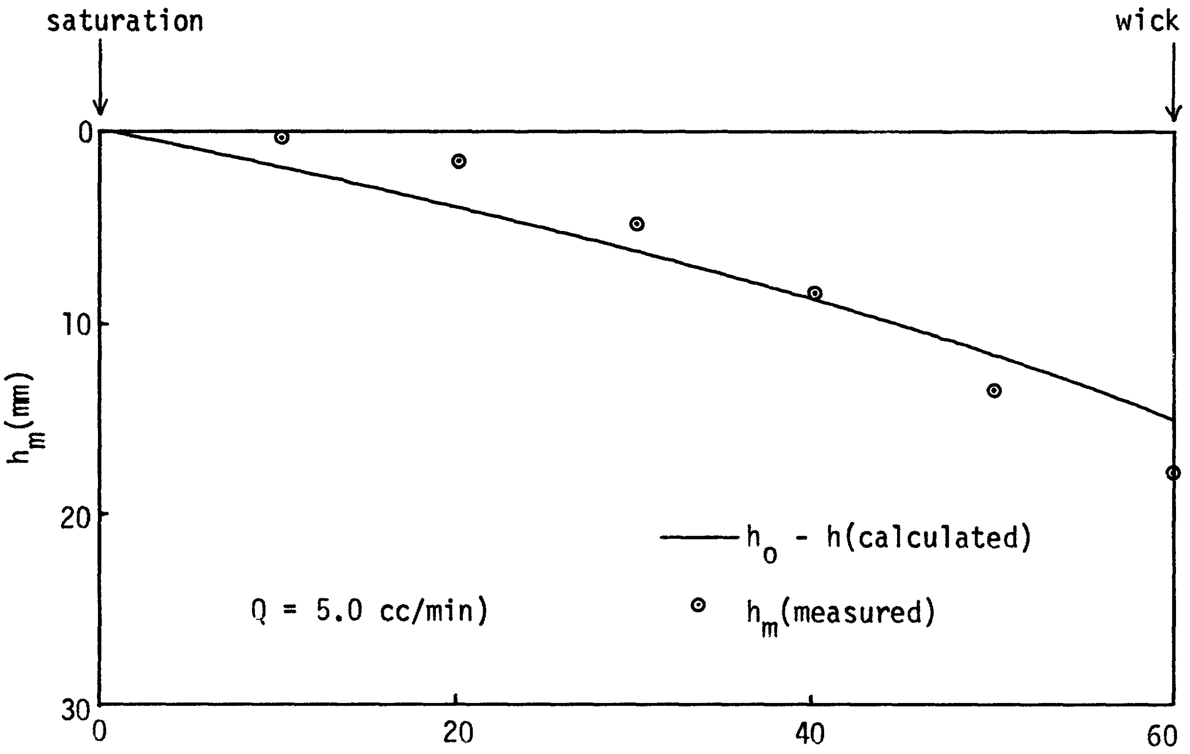

Fig. 6.18 Drainage profile for L=60cm

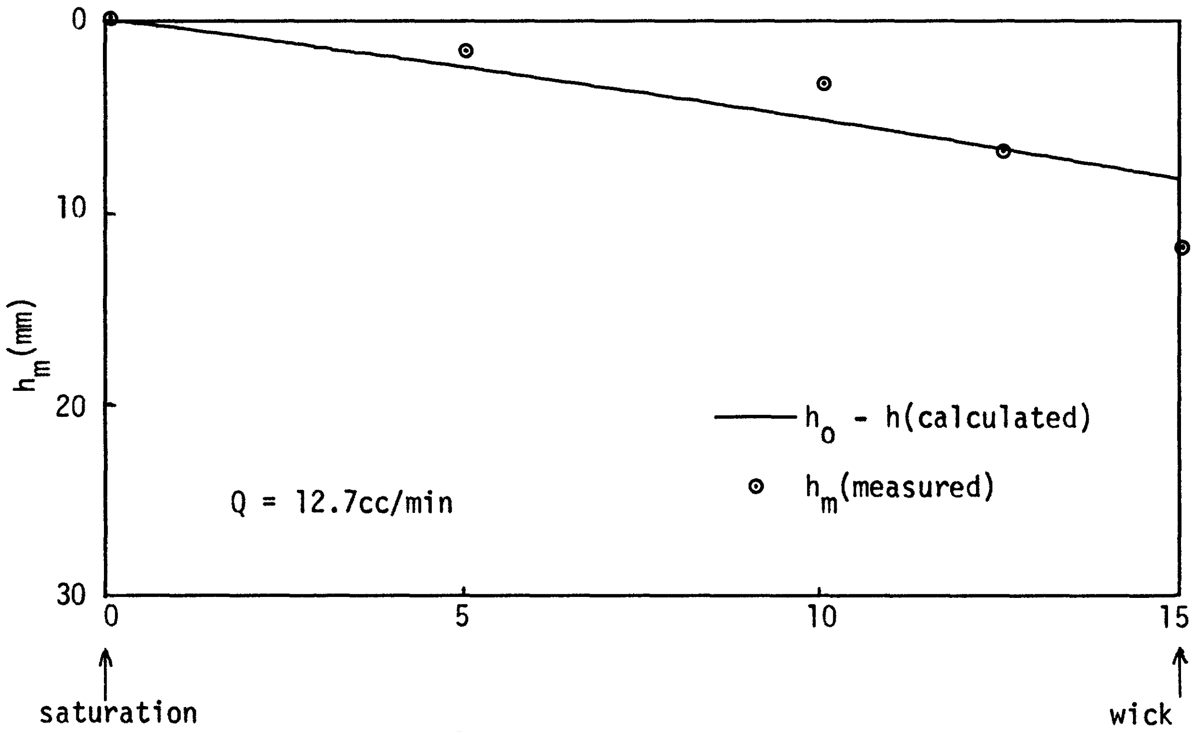

Fig. 6.19 Drainage profile for L=15cm

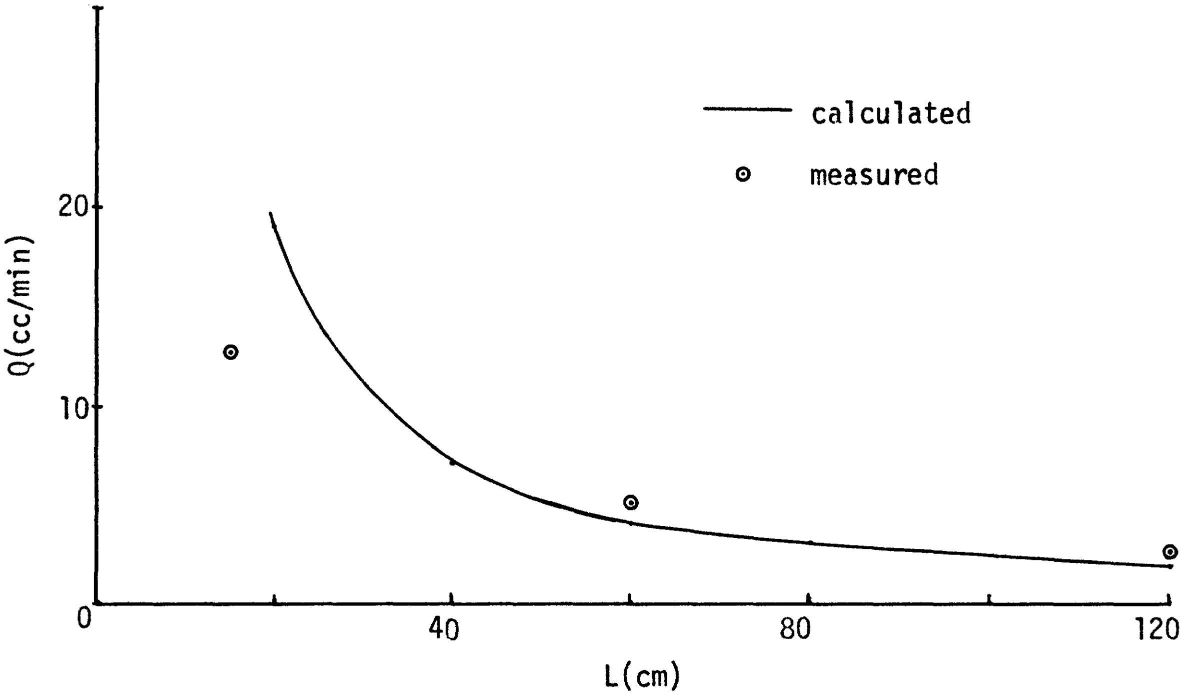

Fig. 6.20 Horizontal drainage rates

important. However, by judicious choice of a measurement parameter, a rough experimental estimate of v_0 was obtained without having to be overly concerned with diffusion.

According to the theoretical model, an initially sharp line separating the saturated and dry regions moves down the incline with velocity v_0 while diffusion acts to smooth out the profile. If the diffusion is strictly linear, then the smoothing of the initially steplike profile proceeds in a symmetrical fashion. This is a well known solution to the linear diffusion equation(32). The midpoint of the transition region remains at exactly half the saturation height, and an observer in the stationary frame will find that the velocity of this point is in fact v_0.

In this experiment, the quantity measured was the time, $t_{1/2}$, it takes for the pressure at given points to decrease to $p_c/2$ with the bundle initially saturated. In the hydrostatic limit this corresponds to the height at the points decreasing to $h_0/2$. Ignoring for the moment the fact that nonlinear rather than linear diffusion really applies here, the velocity of an apparent front can be determined. In order to obtain consistent results, the bundle was initially saturated by careful immersion to minimize trapped air bubbles. The wick at the lower end was not used during these measurements. The manometer tube opening, which contacted the bundle, was enlarged to about 1mm in diameter; and the manometers used were tested to have a response time of several seconds to abrupt pressure changes.

Figure 6.21 is a plot of $t_{1/2}$ versus distance from the upper end of the bundle at various angles of incline. For the larger values of θ, straight lines can be drawn extending to the origin. Departure from this

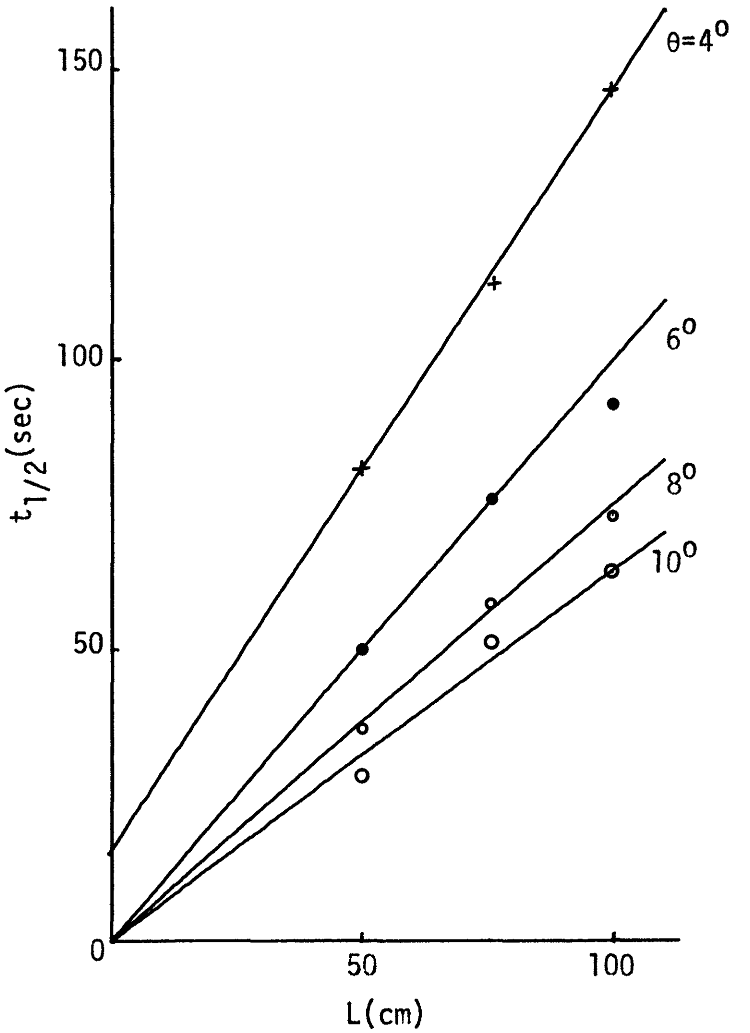

Fig. 6.21 Plot of $t_{1/2}$ vs. distance from upper end of bundle

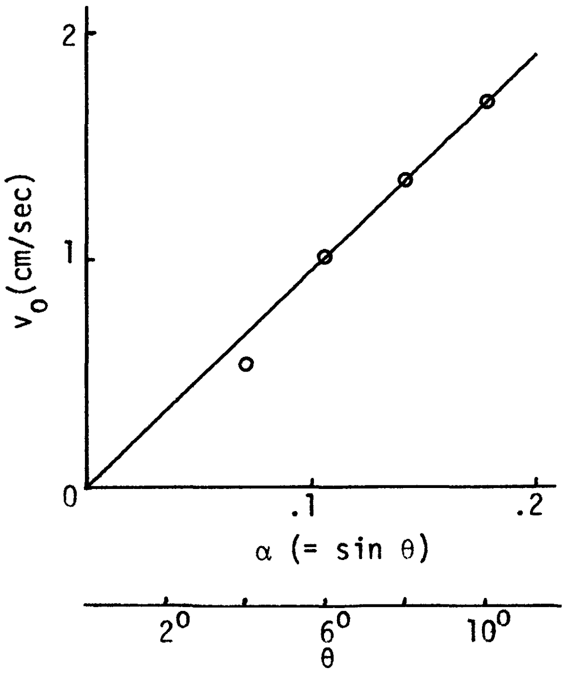

Fig. 6.22 Dependence of drainage velocity on angle of incline

behavior is noted for $\theta = 4°$, which is not too surprising since at this low value of θ, the lower boundary condition begins to have significant effect upstream. The slopes of these lines give the velocity of an apparent front and the dependence of this velocity on α is plotted in Fig. 6.22. The linear dependence shown strongly support the idea of a constant velocity transition region.

For the expression $v_o = \rho g K_z \alpha / n_e$, the coefficient of α is calculated to be 14.7cm/sec. In comparison, the value of 9.5cm/sec given by the slope of the experimental curve is reasonable considering that nonlinear diffusion and upper boundary effects have not been accounted for.

6.7 Summary

Flow in a stranded bundle appears to be quantitatively described by the theoretical model provided the free surface assumption holds and air bubbles are successfully avoided. The distinction is pointed out between gravitational versus diffusional forces as expressed by the $\rho g \alpha$ and the $hp^*/\partial z$ terms in (5.3). When the angle of incline of the flow structure is slowly varying as it would for a transmission line span, the flow is expected to be near uniform flow where the gravitational force is the dominant driving force. If the angle of incline is near zero, as at the mid region of the span, then only diffusive forces can act to cause flow. Wicks must be used to introduce this latter effect.

An important conclusion to be drawn from this section is that there exist a limit to the capability of wicking which depends on the flow structure itself rather than on the parameters of the wick. A sample calculation of wick separation will be given in the next chapter.

One unwanted phenomenon of flow in the stranded bundle structure is that air bubbles almost always form in the channels to a degree dependent upon the history of wetting. This phenomenon results in an apparent decrease in permeability. Some testing was done with the bundles randomly wetted down. The results showed large fluctuations but always with the apparent permeability significantly lower than that with the bundle carefully prewetted. The magnitude of the decrease was on the order of several times but was occasionally as much as an order of magnitude. In Chapter 7, an alternative design is proposed which should eliminate this problem.

CHAPTER 7

DESIGNING AN ABSORBENT CONDUCTOR

7.1 Design Considerations

In designing an absorbent conductor for actual field use, the primary factors to be considered are:

1) absorbency
2) permeability
3) water storage capacity
4) Drainage capability using wicks

These factors are discussed separately in the previous chapters; this chapter shows how they are related in the overall absorption scheme. Mechanical and electrical constraints are certainly important and they may ultimately determine the geometry of the conductor. Nevertheless, the design principles and procedures set forth in this chapter apply to a variety of geometries. In the following sections, specific design examples are given wherever possible.

7.2 Optimization of Conductor Geometry

From the relationships of absorbency and permeability to the channel size of the absorbent conductor, a channel size can be chosen to maximize the flow capability of the conductor. As an illustration consider the sample conductor, shown in Fig. 7.1, which is composed of a current carrying core and a thin concentric porous cylinder. Unlike the experimental porous conductor described in Section 4.3, this sample conductor stores and transports water primarily in the space between the core and the cylinder. The opening at the top of the cylinder allows free movement of air. Since a high degree of surface wettability is necessary for capillary absorption, perfect wettability is assumed.

The permeabilities k_c, defined in Chapter 3, and K, defined in Chapter 5, are used in this chapter; and it is helpful to point out the difference between them. k_c, the channel permeability, is defined with respect to the actual flow area; while K is defined with respect to the total cross-sectional area of the porous matrix and includes the viscosity of the liquid. Hence they are related by

$$K = \frac{n_e k_c}{\mu}$$

where n_e is the ratio of available flow area to total cross-sectional area.

The absorbency of a conductor is measured by the water level in the conductor at saturation (defined here as the point when the liquid pressure at the bottom of the conductor is equal to the atmospheric pressure). This level, h_s, is related to the channel size, r_o, by (3.2). Applying (3.2) to the geometry of Fig. 7.1 yields

$$\frac{\gamma}{r_o} = \rho g h_s \tag{7.1}$$

Note that a factor of two is missing here because the meniscus has curvature only in one direction.

The permeability of channels of arbitrary shapes is defined by (3.6). Deriving this quantity requires knowledge of the flow rate dependence on the driving force, which might be gravity or a pressure gradient. If the channel geometry is complicated, or if phenomena such as air bubble entrapment (see Section 6.7) is present, accurate determination of the permeability may require measurement.

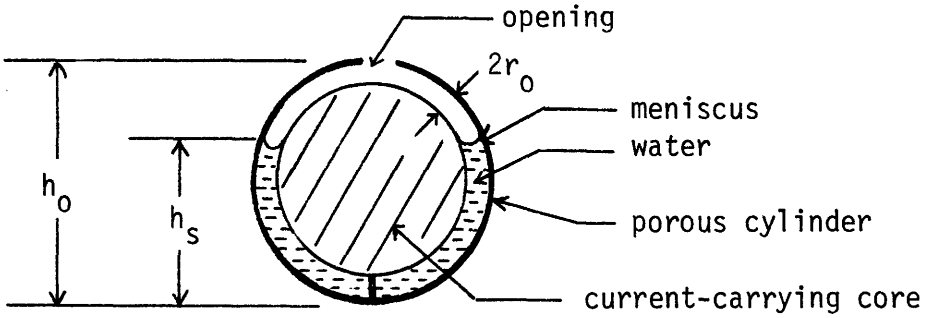

Fig. 7.1 Another absorbent conductor design

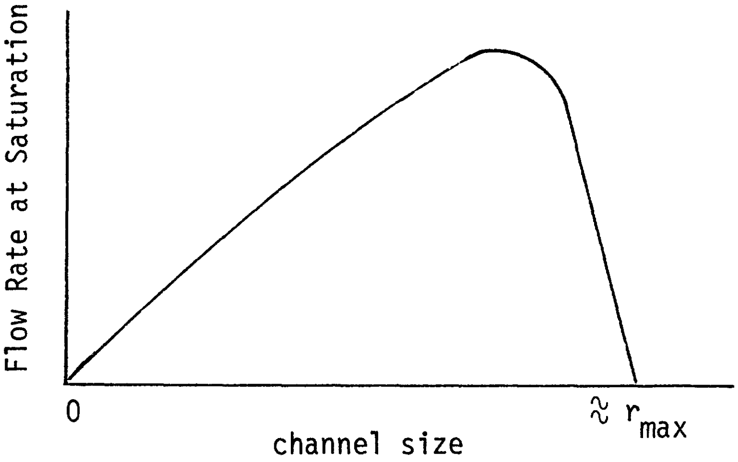

Fig. 7.2 Dependence of flow capacity on channel size

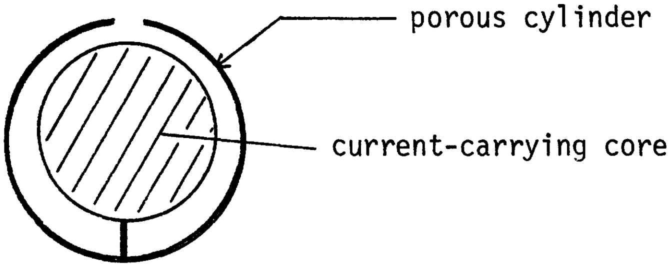

Fig. 7.3 Increasing the permeability with nonconcentric arrangement

The simple geometry of Fig. 7.1 allows calculation of the permeability since the Poiseuille flow solution for parallel plates (29) can be applied. With the conductor at an angle of incline θ and assuming that gravity (as represented by $\rho g \sin \theta$) is the only driving force, the flow rate Q is calculated to be (Ref. 29 gives the transverse velocity distribution in terms of the driving force G. Integration of the velocity over the flow cross section yields the total flow)

$$Q = A \frac{r_o^2}{3\mu} \rho g \sin \theta \tag{7.2}$$

where A is the flow area. Application of Eq. (3.6) with A_c replaced by A yields

$$k_c = \frac{1}{3} r_o^2 \tag{7.3}$$

Comparison of this permeability to that of a cylindrical channel (see (3.6)) shows that the dependence of k_c on the geometrical shape is given by the coefficient of r_o^2.

Comparing (7.1) with (7.3) one finds that the dependence of k_c on channel size is stronger than the dependence of capillarity (as given by γ/r_o) on channel size. Hence a higher total flow rate can be obtained by sacrificing some absorption capability. For example, if r_o is doubled, then k_c quadruples. Although the channel is now only half full at saturation, the maximum flow rate Q_s is still increased by a factor of two. A theoretical limit to increasing r_o exists roughly at the point where the meniscus cannot support a water column of height r_o; i.e.,

$$\gamma/r_{max} = \rho g r_{max}$$

$$r_{max} = (\frac{\gamma}{\rho g})^{1/2} = 2.7\text{mm} \qquad (7.4)$$

At this limit, the channel fails completely to fill with water and the apparent permeability falls to zero. Fig. 7.2 illustrates this dependence of Q_s on channel size. In practice, because of the likelihood of imperfect wettability, r_o should be well below r_{max}.

A further increase in flow capacity is possible by using a non-concentric arrangement as shown in Fig. 7.3. This configuration maximizes the permeability without sacrificing capillarity. The channel size at the bottom is still subject to the limit given by (7.4) since filling of the channel must begin there. Analysis of flow in this geometry is more difficult because the permeability is now a function of the water level.

To keep the calculations simple, let us assume that the porous cylinder is concentric and that at saturation the channels are half filled, $h_s = h_o/2$. Choosing h_o = 3cm and using (7.1), (7.2) and (7.3),

$$r_o = .5 \text{ mm}$$

$$k_c = .0008 \text{ cm}^2$$

$$Q_s(=6^o) = 4.0 \text{ cc/sec}$$

The importance of channel size is evident when this value of Q_s is compared to the value of .6 cc/sec calculated for the stranded bundle in Section 3.3.3.2.

7.3 Requirement on Transverse Permeability

The rate of water penetration from the conductor surface into the interior channels depends on the capillary pressure of the conductor and on its transverse permeability. A design requirement is that the maximum penetration rate be at least as large as some given precipitation rate, say in a light rain fall. For a conductor having a homogeneous cross section, such as the stranded conductor, the maximum penetration rate can be estimated using (5.14) (letting h be nonzero but small compared to h_0).

Equation (5.14) is however not suitable for the example of Fig. 7.1 since resistance to water penetration is given primarily by the porous cylinder. The maximum penetration rate for this case can be estimated using (3.3) which governs flow through porous media. Since the flow across the cylinder is mainly driven by the capillary pressure inside, the gravitational term in (3.3) is neglected. An order of magnitude estimate is then given by

$$q_{\text{penetration}} \approx \frac{k_t}{\mu} \frac{\gamma/r_o}{d} \tag{7.5}$$

where k_t and d are respectively the permeability and the thickness of the porous cylinder. If this rate is to be greater than the water-collection rate q', then

$$k_t > \frac{\mu d r_o}{\gamma} q' = 4.8\text{x}10^{-11} \text{ cm}^2$$

where d = 1 mm, r_o = .5 mm, and q' = .1 in/hr = $7.1\text{x}10^{-5}$ cc/cm^2-sec, were chosen. Comparing this value of k_t to the ones listed in Table 3.1, we see that the required penetration rate can be easily achieved.

7.4 Wick Design

The simplest wick consists of placing a porous structure in contact with the conductor as shown in Fig. 7.4. The transverse permeability of the conductor, K_x, then plays a large role in the drainage process. Suppose that the conductor is at an angle of incline $\theta(= \sin^{-1} \alpha)$ and the flow is blocked just downstream from the wick, then by conservation of mass

$$Q_s = K_z \rho g \alpha A_c \approx K_x A_w \rho g$$

The required contact area A_w is approximately given by

$$A_w \gtrsim \frac{K_z \alpha A_c}{K_x} \tag{7.6}$$

The maximum flow capability of the wick is given by (6.5) and the wick parameters must be chosen such that this capacity exceeds Q_s. From the discussion in Section 6.5, one can deduce that the dimensions of the wick need only be on the order of the conductor diameter.

At the upper parts of the transmission line span, the angle of incline dictates what the maximum flow can be; wicks there simply serve to interrupt flow and thus help to prevent saturation for the parts of the conductor below it. Hence these wicks do not have to impose a low pressure condition on the flow.

At the horizontal midsection, the flow rate is determined by how low a pressure the wicks can impose on the flow. Section 6.5 discusses in some detail the use of wicks to promote horizontal flow. An ideal wicking scheme would have the conductor flow channels bending downward; a good wicking scheme must be as close an imitation of this as possible.

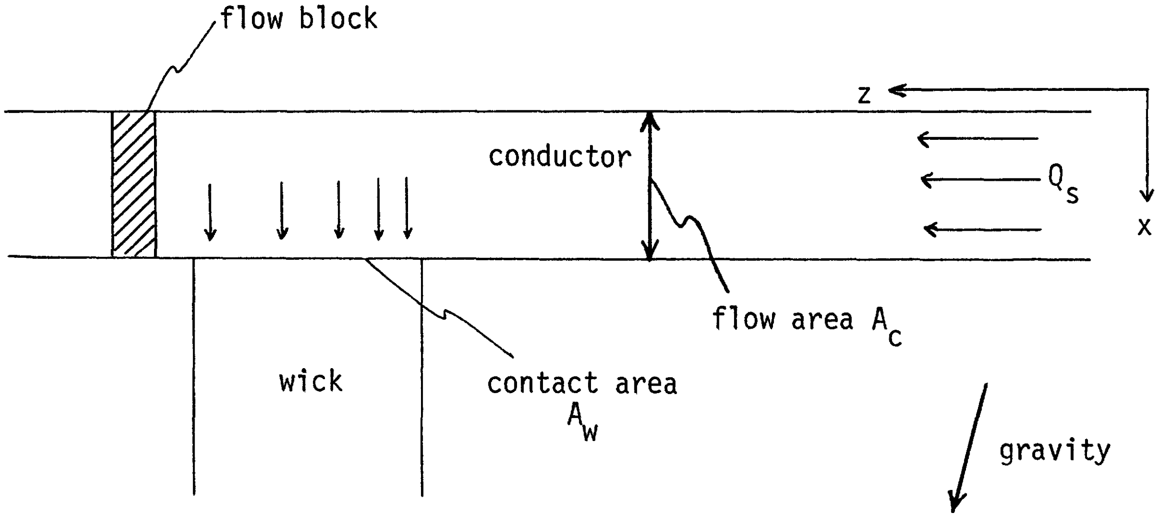

Fig. 7.4 Diagram of flow in wicking

7.5 Placement of Wicks

In this section an example is shown on the calculation of the wick spacing necessary to prevent saturation in a continuous light rain fall. A steady state is assumed to have been reached. The exact configuration of the conductor is not relevant for the calculation; only the longitudinal permeability K_z is needed. Fig. 7.5 shows a diagram of half a transmission line span of 300 m (1000 ft) total length. Only a single conductor is considered but this discussion applies equally well to multi-conductor bundles. The angle of incline varies nearly linearly from 6^o at the upper end to 0^o at midspan. The elliptical structures represent electrical shields for the wicks placed at various points along the line.

At the upper parts of the span, the saturation flow rate Q_s is given by (5.19), with q and h replaced respectively by Q_s and A_s, the flow area at saturation. The wicks effectively isolate the conductor sections between them (blocking of flow may be necessary as shown in Fig. 7.4) so that the total water collection rate of each section at steady state $Q'L_i$ equals the volume drained by the wick at its lower end. If wicks are placed where saturation just takes place, then

$$Q'L_i = \rho g(\sin \theta_i)K_z A_s \approx \rho g K_z A_s \theta_i \qquad (7.7)$$

Since θ varies linearly with distance,

$$\theta_i = (L - \sum_{j=1}^{i} L_j)(.1/L) \text{ radians} \qquad (7.8)$$

Combining (7.7) and (7.8) gives

$$L_i = \frac{M}{1+M} (L - \sum_{j=1}^{i-1} L_i) \qquad (7.9)$$

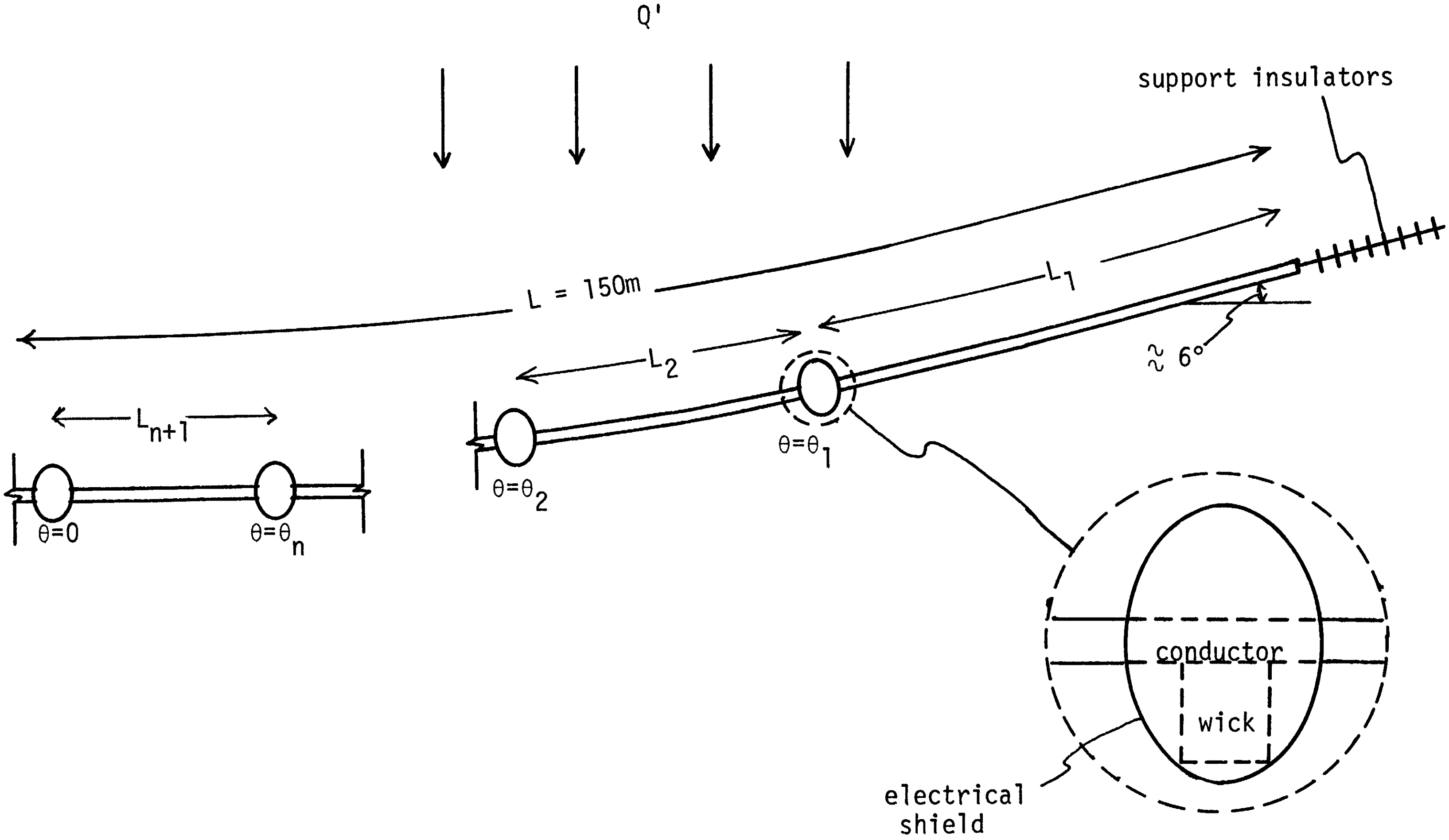

Fig. 7.5 Diagram of wick placement on transmission line span

where

$$M = \frac{\rho g K_z A_s}{Q'} \left(\frac{1}{L}\right)$$

At midspan, only diffusion flow (see Section 5.4.1.2) applies, and (5.27a), multiplied by an effective width w_{eff}, gives the relation between water collection rate and wick separation. Approximating w_{eff} by $h_o/2$,

$$L = \sqrt{\frac{\rho g K_z h_o^3}{Q'}} \qquad (7.10)$$

where h_o is the diameter of the conductor.

Table 7.1 gives the results of sample calculations of wick spacings for a conductor of 1.5 cm radius in a .05 in/hr rain fall (The spacing in some cases are shorter than the calculated value so that the sum of the spacings is 150 m). The value of .001 cc-sec/gm equals the permeability of the stranded bundle tested in the laboratory (see Sections 6.3), while the value of .005 cc-sec/gm is equivalent to the optimized permeability of the sample conductor discussed in section 7.2. It is quite clear from Table 7.1 that a large conductor permeability can significantly reduce the necessary number of wicks.

7.6 Evaluating Absorption Capability

The absorption capability of an absorbent conductor is a function of its storage capacity and drainage efficiency, and the precipitation rate. A steady state analysis totally ignores the effect of the storage capacity and hence should not be the sole basis on which absorption performance is evaluated. For instance, regardless of its drainage efficiency, a conductor of 1.5 cm radius with a 20% pore volume ratio will not saturate in

	K_z = .001 cc-sec/gm	K_z = .005 cc-sec/gm	K_z = .01 cc-sec/gm
L_1	44 meters	100	121
L_2	31	27	20
L_3	22	15	9
L_4	15	8	
L_5	11		
L_6	7		
L_7	5		
L_8	5		
L_9	5		
L_{10}	5		

Table 7.1 Calculated Wick Spacing (see Fig. 7.5)

a very heavy, .5 in/hr, rain which lasts less than 20 minutes.

A transient flow analysis is possible using the flow model developed in Chapter 5. Equation (5.28) can be applied to each conductor section separated by wicks; the solution may however have to be obtained numerically. Section 5.4.1.3 discusses drainage after the conductor has been fully saturated and shows that a drainage velocity

$$v_o = \frac{\rho g \alpha K_z}{n_e} = \frac{\rho g \alpha k_c}{\mu} \qquad (7.11)$$

can be used to estimate a drainage time.

CHAPTER 8

CONCLUSIONS AND SUGGESTIONS FOR FUTURE RESEARCH

Any noise reduction method must involve the interference of one of the steps in the acoustic noise generation mechanism as described in Chapter 2. Absorption of surface drops or the use of hydrophobic coatings attempts to remove the potential corona sites; decrease of surface gradient at the sites or imposition of a dc bias attempts to reduce streamer activity; addition of surface active agent attempts to change the electrohydrodynamic behavior; etc. So far, there seems to be little possibility of completely eliminating corona during foul weather although various approaches can provide different degrees of improvement.

In this thesis, the method of capillary absorption was developed and its capability in reducing audible noise was experimentally verified. The effectiveness of the method depends on the type of foul weather. In fog where the water condensation rate is low there is little difficulty in eliminating surface drops which cause corona. In heavy rain, there is little hope of any improvement; but heavy rain occupies only a small portion of foul weather periods, and psychologically audible noise generated then is not as annoying because of the high ambient noise level.

Surface wettability is the single most crucial factor in the absorption scheme. A sufficient degree of wettability has been achieved in the laboratory with a clean hydrated aluminum oxide surface, but the surface showed a natural tendency to become less wetting. Possible causes are contamination from the laboratory atmosphere or a change in the surface chemical structure such as dehydration of the surface molecular layers. Tests of the surface in controlled atmospheres could be made to determine the true cause.

Field observations show that a weathered aluminum surface tends to be wetting, at least after prolonged exposure to humid weather or after rain. This indicates that the surface has a small receding contact angle. But as discussed in section 2.1.2, a large advancing angle will result in surface drop formation in fog or light rain. Hence a quantitative study of the wettability of weathered aluminum surfaces, including perhaps a chemical analysis, is desirable.

If necessary a wetting surface coating probably could be applied in the same way that meat wrapping cellophane is coated with surfactant to prevent fogging. This coating would dissolve at a very slow rate and hence would have a continuously renewed surface that is less susceptible to contamination. Of course the addition of surfactant to the collected water would likely affect the absorbency as well by decreasing the air-water surface tension. This effect will be small since the air-water surface tension does not decrease by much more than a factor of two with most surfactants.

Next to wettability, saturation poses the biggest problem for the absorption method. Estimates show that a reasonable pore volume is sufficient to contain the condensed moisture in fog but is insufficient in light-to-moderate rainfalls. Drainage by wicking can extend the absorption capability of a conductor, but at the cost of having to electrically shield the wicks. By optimizing the conductor channel geometry, the required number of wicks can be kept to a minimum. According to the calculations of section 7.6, about 5 to 7 wicks per span is needed to completely suppress saturation in a continuous, .05 in/hr, rainfall. In addition, the water storage capacity of an absorbent conductor should contribute significantly to its performance in short foul weather periods with high precipitation rates.

The difference in geometry between the stranded conductor of Chapter 3 and the porous-cylinder conductor of Chapter 7 illustrates that the absorption scheme is not much restricted by conductor geometry. The geometry chosen for implementation must satisfy the mechanical and electrical constraints as well as display ease of construction. Cost is of course the ultimate constraint in this, as in any other, noise reduction scheme.

APPENDIX A

BEHAVIOR OF PENDENT DROPS OF LOW SURFACE TENSION UNDER ELECTRIC STRESS

A.1 Discussion

As discussed in Section 2.4, a pendent drop at zero flow rate tends to assume a conical shape if it is electrically stressed beyond the point of instability. For water drops under atmospheric pressure, the electric field intensification at the tip of the cone leads to the formation of corona pulses, and the interaction of the corona with the water surface results in oscillations of the drop tip. The major part of the cone can be quite stationary for wetting pendent drops with dc imposed voltages.

When a water drop of decreased surface tension (with surface active substance added) is electrically stressed beyond instability, a visible jet issues from the cone tip. Corona activity usually accompanies the jet, but the current waveform is quite different from that recorded for the pure water drop. For dc applied voltages, the jet appears to be quite steady, at least for voltage levels not too far above the critical voltage of instability. With no addition of liquid, the initial drop volume steadily decreases while liquid is convected away in the jet; this situation is distinguished from the jet mode (with pure water drops) observed by Hoburg and Melcher where a large imposed flow rate was necessary.

Several factors affect jet formation with these low surface tension drops. Among these are surface tension, liquid conductivity, electric field strength, drop size and shape, and the rate of liquid addition. These factors are usually strongly interrelated so that the variation of one usually leads to the variation of others.

In our laboratory we made observations of the jet modes and investigated the effects of varying surface tension and liquid conductivity. For normal temperatures and pressures, the surface tension of water is not subject to very much change; it can hardly be increased and can be decreased by about a factor of two at most by adding surface active substances(16). The conductivity of water, on the other hand, can be changed by orders of magnitude by the addition of soluble ionic substances such as salt.

A.2 Experimental Setup

As shown in Fig. A.1, a pair of 3" diameter planar electrodes were used with a gap width of about 1", and the drop hung from the upper electrode in a perfectly wetting configuration. The voltage was set at a point slightly above the level of initial drop instability, about 10 kV. A reservoir of liquid was connected to the drop so that the drop size remained essentially constant even with the small continuous loss of liquid.

Alcohol was used to lower the surface tension of the drops and salt was used to increase the water conductivity. The surface tension of the solution used was measured by the capillary rise method(16) while the conductivity was determined using a conductivity cell of dimensions 1/2" dia. x 1/2".

A.3 Drop Behavior as a Function of Surface Tension and Conductivity

A.3.1 Positive dc

Near its normal surface tension, the water drop tip gave off corona without exception for conductivities above 10^{-4} mho/m. Only after the surface tension had been lowered to near 30 dynes/cm did the behavior

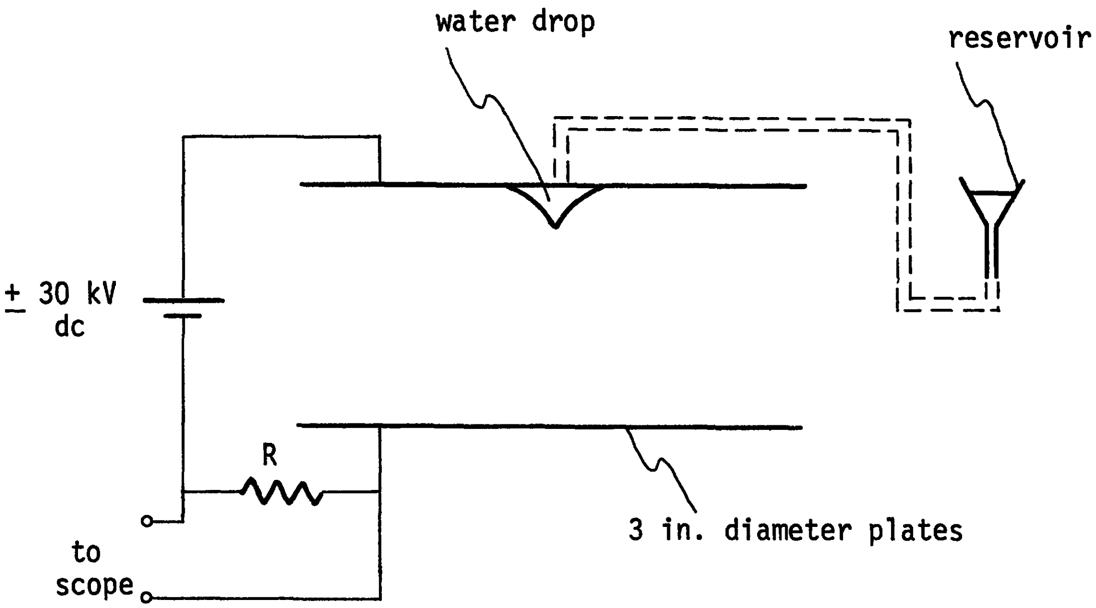

Fig. A.1 Apparatus for observation of jet modes.

change. For conductivities below approximately 10^{-2} mho/m, a thin jet issued from the tip and terminated in a fine conical mist as shown in Fig. A.2a. The length of the jet appeared to have an inverse dependence on the conductivity, changing from about 1 mm at a conductivity of 10^{-4} mho/m to zero length at conductivities above 10^{-2} mho/m. For the high conductivities, the spray cone originated directly from the tip. A mapping of the drop behavior is given in Fig. A.3a.

A.3.2 Negative dc

At low surface tension (30 dynes/cm) and conductivity (10^{-4} mho/m), the drop also exhibited the same jet mode as the positive case. At slightly higher surface tensions and conductivities, a different jet occurred which appeared much thicker and, as illustrated in Fig. A.2b, did not terminate in a spray cone. At a conductivity above 10^{-2} mho/m, the corona mode once again returned as shown in the drop behavior map in Fig. A.3b.

A.4 Description of Jets

A.4.1 Positive Jet

High speed movies, of which three enlarged frames are shown in Fig. A.4, showed that the positive jet was about 40 microns in diameter and that the top of the spray cone apparently consisted of a violently whipping tail of the jet. The exposure time of about .1 msec was too slow to stop-action this whipping motion. A kink instability may well be taking place similar to that observed by Hoburg and Melcher, but the magnitude of the kink appeared to be much larger in this case.

A dc current of about 5μA was measured and could be attributed either to glow corona, as for the Hoburg jet, or to convection of surface charge.

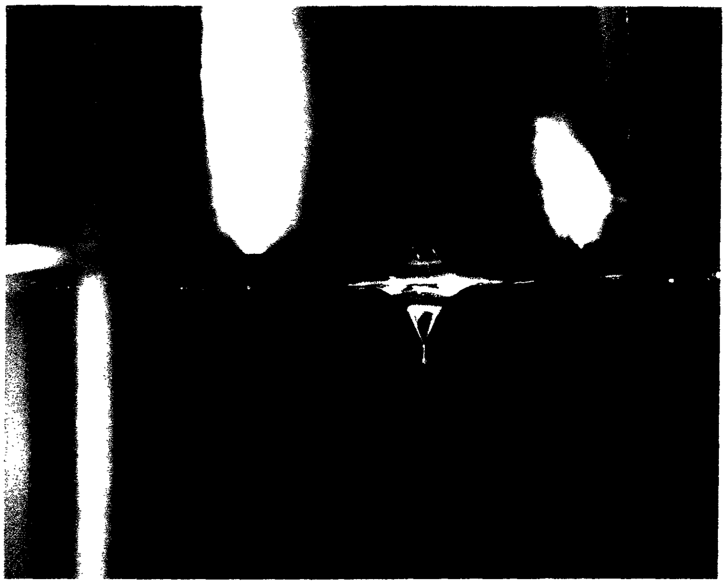

(a)

Steady Jet Under
Positive Applied
Potential

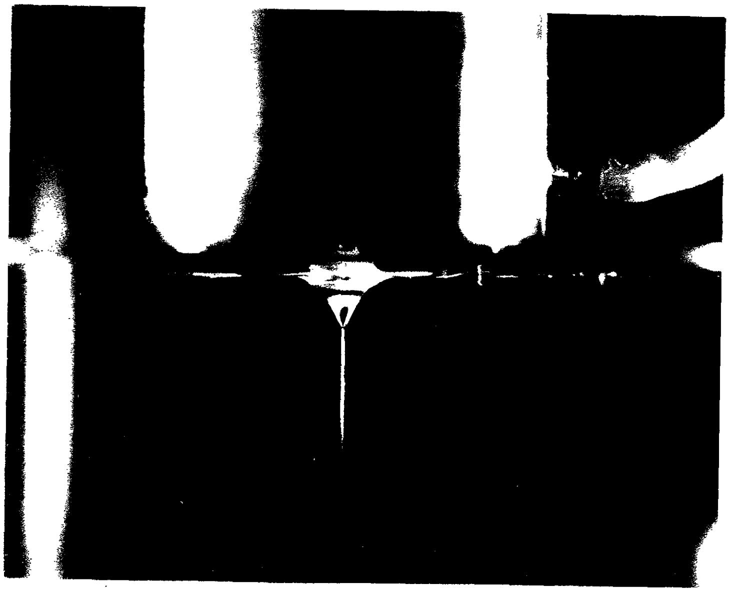

(b)

Unsteady Jet Under
Negative Applied
Potential

Fig. A.2 Visual appearance of steady and unsteady jet modes (1% photoflo)

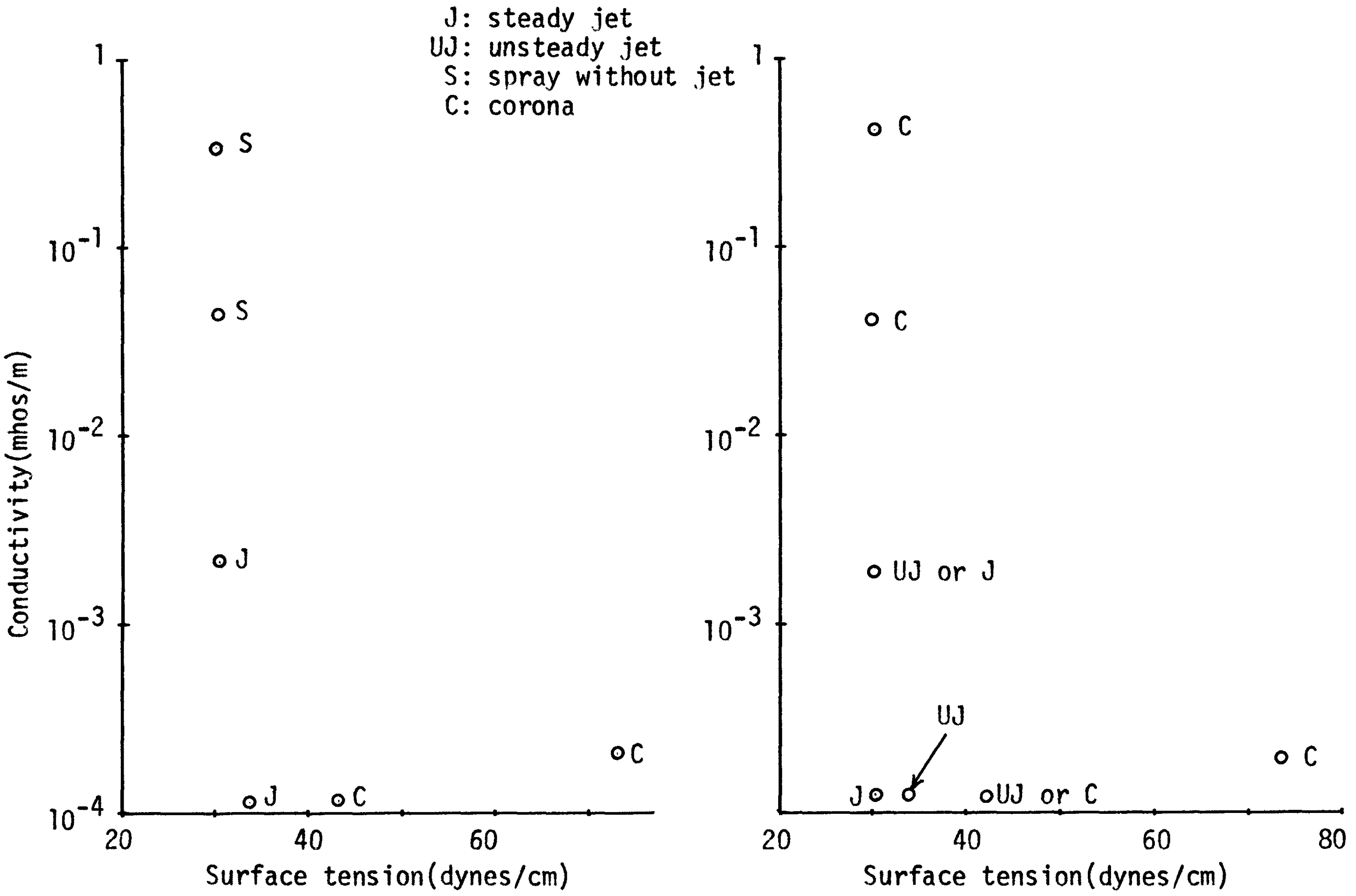

a Positive dc

b Negative dc

Fig. A.3 Dependence of pendent drop behavior on surface tension and conductivity

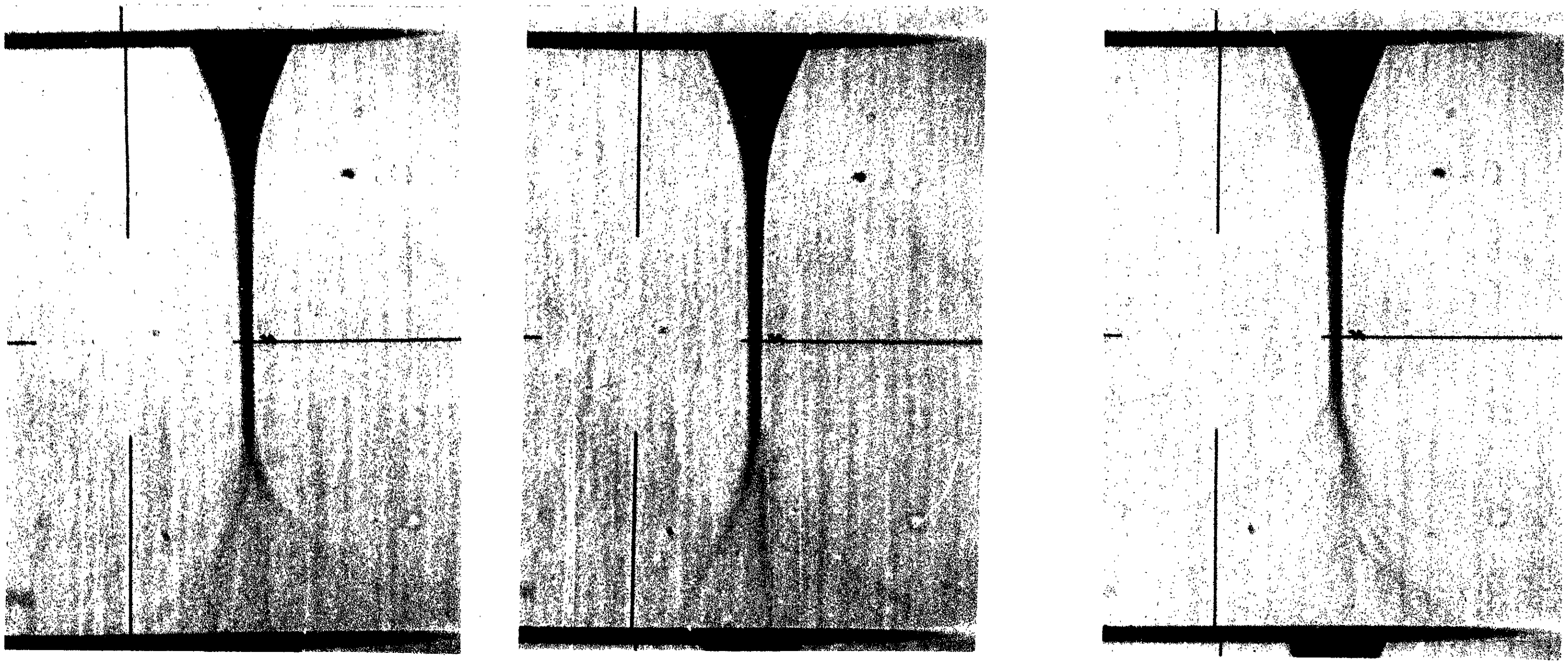

1 2 3

mag.: 53x
film speed: 8000 frames per sec.

solution: 1% photoflo
conductivity: 5.5x10^{-3}mho/m
surface tension: 34 dynes/cm
current: dc at 5μA

Fig. A.4 Three consecutive frames in high speed film of positive jet

The latter case appeared more likely since no luminosity was detected by eye or by time exposure photography.

A.4.2 Negative Jets

The spraying jet found using low surface tension and conductivity drops was identical in appearance to the positive jet and the measured current was again several microamperes dc.

High speed movies showed that the nonspraying jet of Fig. A.2b was actually not continuous, but periodically formed with accompanying Trichel corona and then pinched off. Fig. A.5a shows consecutive frames of the movie covering one cycle of jet formation (about 1 msec). The current trace is shown separately in Fig. A.5b and also superimposed on the movie. From the photographs, the diameter of the jet was measured to be about 40 microns, and the jet tip advanced at an approximate speed of about 130 cm/sec.

Several reasons can be given for the "hump" in the current waveform: 1) capacitive charging in the measurement circuit; 2) occurrence of negative glow corona; and 3) convection of surface charge. The first reason can be ruled out since Trichel pulses from a distilled water drop did not give such a "hump" for the same measurement circuit; and of the two remaining reasons, surface charge convection appears more likely.

A.5 Formation of Jets at High Electric Gradients

Some testing was done with 1% photoflo drops (surface tension at 30 dynes/cm, conductivity at 5×10^{-4} mho/m) to determine the possibility of noise reduction by lowering surface tension. The cylindrical cage electrode, shown in Fig. 4.1, and a 3/4" diameter inner conductor were used. The flow rate was controllable with this setup.

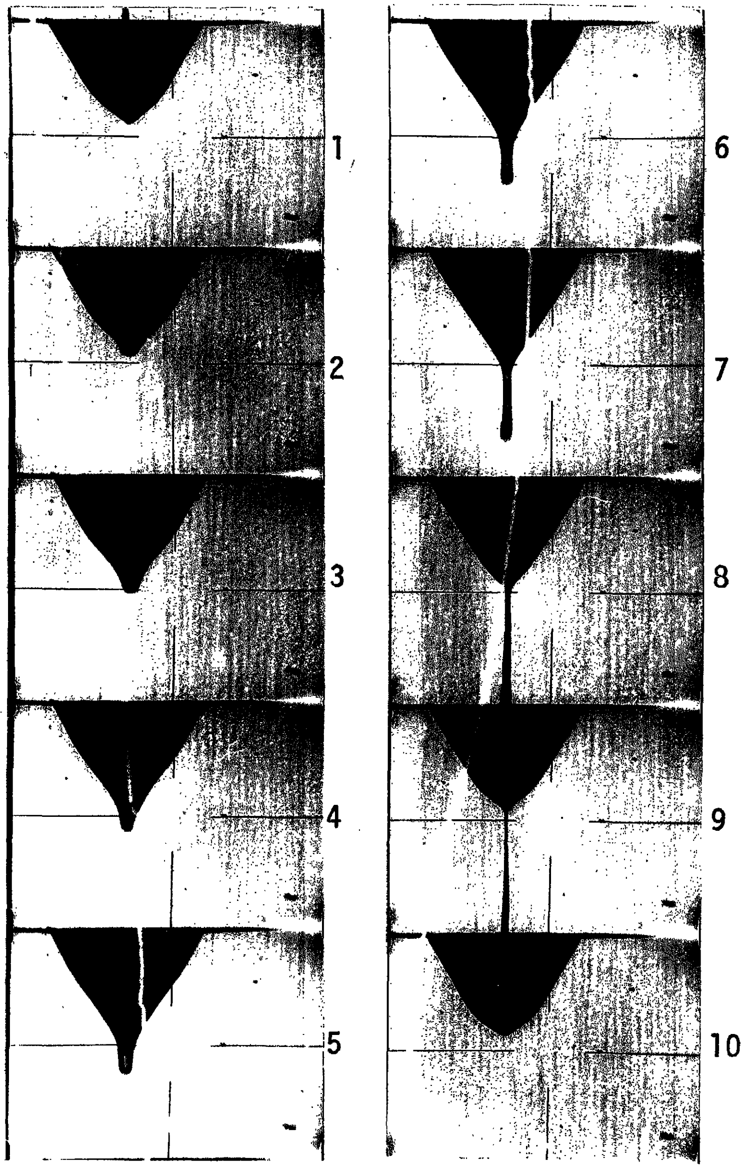

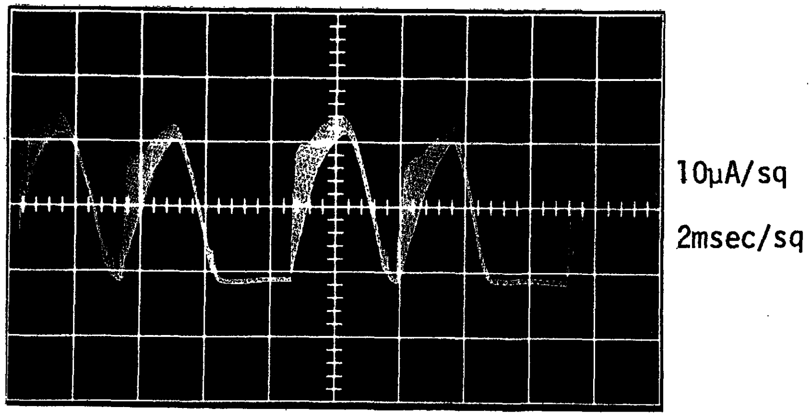

(b)

(a) solution: 1% photoflo
conductivity: 5.2×10^{-3} mho/m
surface tension: 34 dynes/cm

Fig. A.5 a) Consecutive frames in high speed film of negative jet (current trace superimposed)
mag.: 19x film speed: 5000pps

b) Scope current trace

With ac applied voltage, high speed movies of the drop showed that jets formed periodically at 120 Hz, but could not be sustained without using a high flow rate. At a surface gradient of 22 kV rms/cm, positive streamers were quite frequent and noise measurements showed no significant difference between a distilled water drop and a photoflo drop.

At high levels of dc surface gradient (about 27 kV/cm), jet formation with the photoflo drop was found to be erratic, being sometimes replaced by corona activity. Varying the flow rate seemed to have some effect on the process, probably by causing changes in the drop volume. The difference in noise levels betwen the photoflo drop and the distilled water drop was very large or insignificant depending on the occurrence of the jet modes.

APPENDIX B

CALCULATION OF FOG CONDENSATION RATES

There are three mechanisms whereby fog droplets condense on an energized conductor: 1) the settling of the droplets by the action of gravity; 2) the impingement of fog droplets carried by wind; and 3) the electric dipolar attraction of the droplets. As shown in this appendix, all three of these mechanisms depend strongly on the fog droplet size. Hence fog data is quite important in this analysis.

Natural fog droplets range in size from 1 to 100 microns in diameter and occur with a density range of 10 to 1000 per cc. The fractional liquid volume ranges from $.01\text{cc/m}^3$ for a light fog to 1cc/m^3 for a heavy sea fog(34). One can infer from the fractional liquid volume data that large fog droplets must occur with small density and vice versa. For each of the listed mechanisms, the condensation rate will be calculated in this appendix for a typical fog with an average droplet diameter of 10 microns and a density of 200 per cc (fractional liquid volume = $.2\text{cc/m}^3$), and a heavy fog with an average droplet diameter of 50 microns and a density of 25 per cc (fractional liquid volume = 1cc/m^3). The conductor is assumed to have a radius of 1.5cm.

B.1 Condensation by Droplet Settling

A droplet free-fall velocity can be calculated by equating the gravitational acceleration to the Stokes drag(29).

$$4/3\ \pi a^3 \rho g = 6\pi\mu_a a v_s \qquad \text{(B.1)}$$

where a = droplet radius

ρ = density of water

μ_a = viscosity of air = $2\text{x}10^{-4}$ gm/cm-sec

v_s = droplet settling velocity.

The rate of water deposition per unit length of the conductor, Q, is given by

$$Q = 2R_c v_s q_f = \frac{4}{9} \frac{R_c q_f a^2 \rho g}{\mu_a} \tag{B.2}$$

where R_c is the conductor radius and q_f is the fractional liquid volume of the fog. Substituting in the numerical values chosen above,

typical fog

$Q = 1.6 \times 10^{-7}$ cc/cm-sec = 6.0×10^{-4} cc/cm-hr

heavy fog

$Q = 2.0 \times 10^{-5}$ cc/cm-sec = .07 cc/cm-hr

B.2 Droplet Impingement by Wind

When fog droplets carried by wind come upon the conductor, the inertia of the droplets tend to carry them into the conductor surface while the dividing air flow tend to carry them around the conductor as illustrated by Fig. B.1. This mechanism of impact collection has been studied with reference to particle collection by aerosols where a collection efficiency η was derived:(35)

$$\eta = K^2/(K + .7)^2 \tag{B.3}$$

K is an impact parameter given by

$$K = 2v\rho_p a^2/9\mu_a R_c \tag{B.4}$$

where v = relative velocity of particle and collector

ρ_p = particle density

a = particle radius

R_c = radius of collector

μ_a = viscosity of air

As one would expect, the impact parameter depends strongly on the particle (fog droplet) radius; the larger particles (droplets) with greater inertia are more easily collected.

Equations (B.3) and (B.4) can be approximately applied to fog condensation. Using a typical wind velocity of 6 mph,

typical fog

$K = .04$

$\eta = .003$

$Q = 2R_c q_f v\eta = 4.3 \times 10^{-7}$ cc/cm-sec = 1.5×10^{-3} cc/cm-hr

heavy fog

$K = 1.1$

$\eta = .37$

$Q = 2.7 \times 10^{-4}$ cc/cm-sec = .96cc/cm-hr

B.3 Fog Droplet Collection by Electric Dipolar Attraction

The interaction of the applied electric field and the induced dipole fields of the fog droplets results in a net attractive force that is independent of polarity. The possibility of the fog droplets having free charge is ignored since the coulombic force averages approximately to zero in the ac field. In this section, the effects of gravity and wind are ignored.

The fog particles attain a constant velocity toward the conductor as a result of force balance between the electric dipolar attraction and Stokes drag as shown in Fig. B.2. By modeling the fog droplets as noninteracting

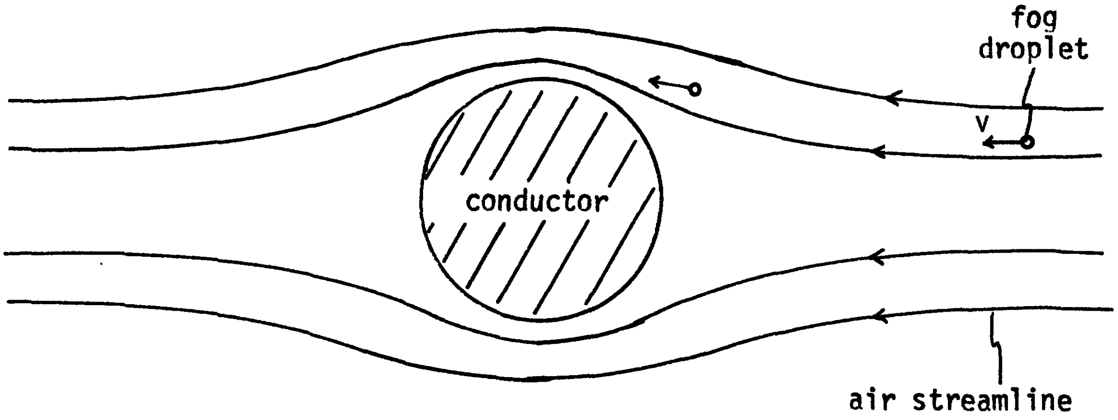

Fig. B.1 Fog condensation by wind

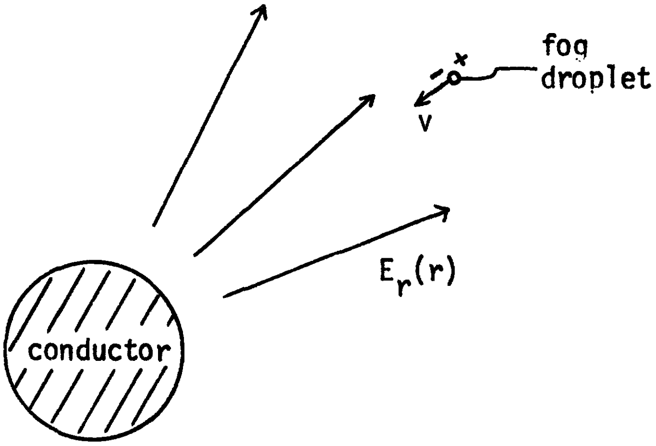

Fig. B.2 Electric dipolar attraction of fog droplets

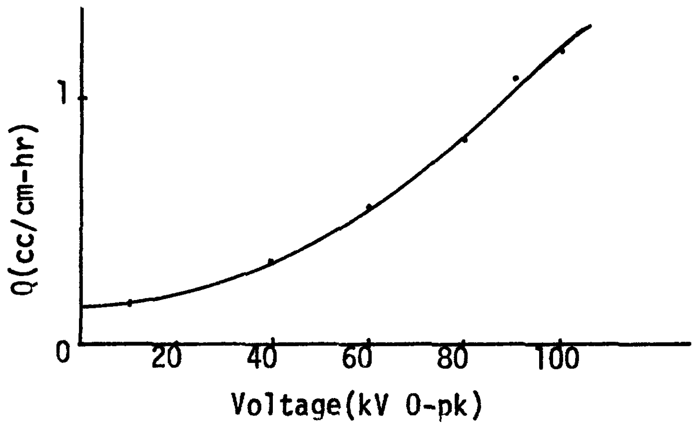

Fig. B.3 Measured fog condensation rates in laboratory chamber dipoles, the electric force on them is given by

$$\bar{P}\cdot\nabla\bar{E} = \alpha\bar{E}\cdot\nabla\bar{E} = \alpha E_r \frac{\partial}{\partial r} E_r \bar{i}_r \tag{B.5}$$

where $\bar{E}$ is the imposed electric field, $\bar{P}$ the induced dipole moment of the fog droplets, and α the polarizability. For a conducting sphere of radius a situated in a uniform field,

$$\alpha = 4\pi\varepsilon_o a^3 \tag{B.6}$$

Equating the Stokes drag on the fog droplets, represented by $6\pi a\mu_a v$, to (B.5) gives the droplet velocity.

$$v = \frac{2\varepsilon_o a^2}{3\mu_a} E_r \frac{\partial}{\partial r} E_r \tag{B.7}$$

where (B.6) has been incorporated. Since $E_r = E_s R_c/r$ where E_s is the conductor surface gradient, the volume flux per unit area is given by

$$J(r) = q_f v = \frac{-2\varepsilon_o a^2 \; q_f \; E_s^2 R_c^2}{3 \; \mu_a \; r^3} \tag{B.8}$$

Assuming that the fog density is fixed at a radius (R_o) of one meter away from the conductor surface and E_s equals 22kV/cm, Eq. (B.8) can be used to estimate a collection rate.

<u>typical fog</u>

$$Q = - 2 \; R_o J(R_o) = \frac{4\pi\varepsilon_o a^2 \; q_f \; E_s^2 R_c^2}{3 \; \mu_a \; R_o^2}$$

$$= 1.0 \times 10^{-9} \text{ cc/cm-sec}$$

$$= 3.6 \times 10^{-6} \text{ cc/cm-hr}$$

<u>heavy fog</u>

$$Q = 1.3 \times 10^{-7} \text{ cc/cm-sec}$$

$= 4.5 \times 10^{-4}$ cc/cm-hr

Table B.1 summarizes the above results and shows the effect of wind being the most significant contributor to liquid collection. Although electric dipolar attraction by itself appears not to be significant, its effect is shown in the next section to be strong when combined with the other collection mechanisms.

Collection Mechanism	Collection Rates (in cc/cm-hr)	
	typical fog	heavy fog
settling of droplets by gravity	6.0×10^{-4}	7.0×10^{-2}
wind induced droplet impingement (6 mph wind speed)	1.5×10^{-3}	.96
electric dipolar attraction (22 kV/cm surface gradient)	3.6×10^{-6}	4.5×10^{-4}

Table B.1

Estimated Fog Collection Rates

B.4 Laboratory Measurements

The dependence of collection rates on the applied voltage was investigated using the fogging chamber illustrated in Fig. 6.1. A 3/4" diameter conductor was used in the tests having a detachable center section that is absorbent. Weighing the center section before and after the fogging period enabled the calculation of a condensation rate. Figure B.3 shows strong dependence of the collection rate on applied voltage. A very dense fog and strong air currents in the chamber led to the large condensation rates. The electric field influence can be explained by the air currents sweeping the fog droplets close by the conductor where the dipolar attraction force is great. In other words, the field can be said to increase the effective area of the conductor.

APPENDIX C

SURFACE TREATMENTS OF THE GROOVED CONDUCTOR

C.1 Electropolishing

After the grooves were cut, the outer strands were deburred by an electropolishing process which selectively etched away rough spots and greatly improved the dry corona performance. No commercial process was locally available; so a process was developed in our laboratory which follows in essence to one described in Ref. 36.

Two epoxy coated stainless steel holders held the 6' aluminum rod suspended in an acid bath of 66% phosphoric acid and 33% ethylene glycol monoethylether contained in a 2"x2"x7' stainless steel tank. A full-wave rectified current with average density about 100 A/ft^2 was passed between the aluminum rod, the anode, and the stainless steel tank. Cold tap water flowing outside the steel tank kept the temperature of the acid bath below 50^oC. At these rather low etching temperatures, a sufficient degree of polishing was achieved in 15-20 min. The acid bath was changed after etching 7-8 rods since prolonged used of the solution resulted in very rough-finish surfaces. A small amount of fumes given off by the process required the use of a hood.

C.2 Anodizing

The anodization process, followed by sealing with water, placed a heavy hydrated oxide coating on the aluminum making it quite wettable. Most of the anodizing in this project was done commercially.

C.3 Maintaining Surface Wettability

The wettability of the aluminum oxide surface was found to degrade in a matter of days in the laboratory although keeping the surface constantly wet, as with daily fog testing, seemed to help in maintaing surface wettability. To restore wettability after degradation, the following procedure was developed:

1) rinsing the rods with dilute NaOH solution (1/2 gm NaOH per liter of distilled water),
2) rinsing with distilled water,
3) rinsing with dilute HNO_3 solution (5% solution),
4) rinsing with distilled water,
5) steaming for about 10 minutes under atmospheric pressure.

The NaOH rinse was quite brief (about 3-4 min.) since the basic solution reacts with aluminum quite readily. The acid rinse was primarily to neutralize any trace amounts of NaOH.

APPENDIX D

REYNOLD'S NUMBER ESTIMATION FOR THE ABSORBENT CONDUCTOR

The water flow being considered takes place in long narrow channels having a small angle of incline to the horizontal. Gravity is the only force which promotes flow, and a characteristic velocity results from the balance between the gravitational force and viscous drag. As discussed in Chapter 3, the absorption requirement limits the characteristics cross-sectional dimension, r_o, of the channels to a maximum of about .5mm. The angle of incline varies from 6° to 0° in a distance of about 150 meters (half a transmission line span). Approximating the channels as cylindrical conduits, a maximum average velocity of 3cm/sec can be easily derived assuming Poiseuille flow; this value will be used as the characteristic velocity V_o below.

The proper Reynold's number, which gives the relative importance of momentum flux to viscous drag, can be derived by scaling the relevant terms in the differential Navier-Stokes equation using characteristic quantities. v_z is expected to be the dominant velocity component, and the magnitude of the momentum term in the steady state is given by

$$|\rho\bar{v}\cdot\nabla\bar{v}| \cong \rho v_z \frac{\partial}{\partial z} v_z = \frac{\rho\, V_o^2}{L} v_z' \frac{\partial v_z'}{\partial z'} \tag{D.1}$$

where ' denotes nondimensionalized quantities, V_o is the characteristic velocity and L a characteristic length for the flow profile. L is conservatively chosen to be 1 meter since any flow variations will likely occur over a longer distance. The magnitude of the viscous term is then given by

$$|\mu\nabla^2\bar{v}| \cong \mu\nabla^2 v_z = \frac{\mu V_o}{r_o^2} \nabla'^2 v_z' \tag{D.2}$$

where r_o is the characteristic length for transverse derivatives. The ratio of the coefficients in (D.1) and (D.2) gives the proper Reynold's number.

$$Re = \frac{\rho V_o r_o}{\mu} \left(\frac{r_o}{L}\right) << 1$$

Note that this inequality holds for L > 1 meter. Thus the momentum term appears negligible when one considers flow on the characteristic length scales of the system.

As to whether laminar or turbulent flow applies, an indicator is again a Reynold's number, but the applicable characteristic length is different from L above. r_o is usually used in calculating this Re.

$$Re = \frac{\rho V_o r_o}{\mu} \simeq 15$$

Since 15 is much below the critical Re for transition to turbulence, which is on the order of 2000(33), laminar flow is expected for the absorbent conductor.

REFERENCES

1. Kolcio, N., Caleca, V., Marmaroff, S.J., Gregary, W.L., "Radio-Influence and Corona-Loss Aspects of AEP 765 kV Line", *IEEE Transactions (PAS)*, Vol. 88, No. 9, September, 1969, pp. 1343-1350.

2. Tsunoda, Y., and Arai, K., "Corona Discharge Phenomena and Noise from Water Drops on a Cylindrical Conductor Surface", *The Journal of the Institute of Electrical Engineers of Japan*, 84, 9, September, 1964, pp. 1430-1439.

3. Akazaki, M., "Corona Phenomena from Water Drops on Smooth Conductors under High Direct Voltage", *IEEE Transactions (PAS)*, Vol. 84, 1, January, 1965, pp. 1-8.

4. Nasser, E., *Fundamentals of Gaseous Ionization and Plasma Electronics*, John Wiley and Sons, Inc., New York, 1971.

5. Boulet, L., and Jakubczyk, B.J., "AC Corona in Foul Weather I - Above Freezing Point", *IEEE Transactions (PAS)*, Vol. 83, May 1964, pp. 508-512.

6. Taylor, E.R., Jr., Chartier, V.L., Rice, D.N., "Audible Noise and Visual Corona From HV and EHV Transmission Line and Substation Conductors-Laboratory Tests", *IEEE Transactions (PAS)*, Vol. 88, May, 1969, pp. 666-679.

7. Pokorny, W.G., Schlomann, R.H., Barnes, H.C., Miller, C.I., Jr., "Investigation of Corona Effects from Wet Bundle Conductors for Application to UHV Configurations", *IEEE Transactions (PAS)*, Vol. 91, January/February, 1972, pp. 211-222.

8. Juette, G.W., Zaffanella, L.E., "Radio Noise, Audible Noise and Corona Loss of EHV and UHV Transmission Lines under Rain: Predetermination based on Cage Tests", *IEEE Transactions (PAS)*, Vol. 89, No. 6, July/August, 1970, pp. 1168-1178.

9. Comber, M.G., and Zafanella, L.E., "Audible Noise Reduction by Bundle Geometry Optimization", *IEEE Transactions (PAS)*, Vol. 92, 5, September, 1973, pp. 1782-1789.

10. Trinh, N.G., Maruvada, P.S., Poirier, B., "A Comparative Study of the Corona Performance of Conductor Bundles for 1200 kV Transmission Lines", *IEEE Transactions (PAS)*, Vol. 93, No. 3, May/June 1974, pp. 940-947.

11. Sforzini, M., Cortina, R., Sacerdote, G., Plazza, R., "Acoustic Noise Caused by AC Corona on Conductors: Results of an Experimental Investigation in the Anechoic Chamber," IEEE Transactions (PAS), Vol. 94, No. 2, March/April, 1975.

12. Hoburg, J.F., Melcher, J.R., "Current-Driven, Corona-Terminated Water Jets as Sources of Charged Droplets and Audible Noise", *IEEE Transactions (PAS)*, Vol. 94, No. 1, January, 1975, pp. 128-136.

13. Ianna, F., Wilson, G.L., Bosack, D.J., "Spectral Characteristics of Acoustic Noise from Metallic Protrusions and Water Droplets in High Electric Fields", IEEE Transactions (PAS), Vol. 93, No. 6, November, 1974, pp. 1787-1796.

14. Bosack, D.J., Unfinished Ph.D. Thesis, MIT.

15. Peek, F.W., Jr., Dielectric Phenomena in High Voltage Engineering, McGraw-Hill, New York, 1929 (3rd edition).

16. Adamson, A.W., Physical Chemistry of Surfaces, Interscience Publishers, New York, 1967.

17. Rayleigh, Lord, "On the Equilibrium of Liquid Conducting Masses Charged with Electricity", Philosophical Magazine, Vol. 14, 1882, pp. 184-186.

18. Zeleny, J., "Instability of Electrified Liquid Surfaces", Physical Review, Vol. X, No. 1, July, 1917.

19. Macky, W.A., "The Deformation of Soap Bubbles in Electric Fields," Cambridge Phil. Soc. Proc., Vol. 26, 1929-30, p. 425.

20. Taylor, G.I., "Disintegration of Water Drops in an Electric Field", Proceedings of the Royal Society of London (series A, 280, 1964, pp. 383-397.

21. Wilson, C.T.R., and Taylor, G.I., "The Bursting of Soap Bubbles in a Uniform Electric Field", Proc. of the Cambridge Phil. Soc., Vol. 26, 1930, pp. 421-428.

22. Dudley, D.M., S.M. Thesis, Dept. of Electrical Engineering, MIT, 1971.

23. English, W.N., "Corona from a Water Drop", Physical Review, Vol. 74, No. 2, July, 1948, pp. 178-189.

24. Dawson, G.A., "Pressure Dependence of Water-Drop Corona Onset and Its Atmospheric Importance," Journal of Geophysical Research, Vol. 74, No. 28, December, 1969.

25. English, W.N., "Positive and Negative Point-to-Plane Corona in Air", Physical Review, Vol. 74, No. 2, July, 1948, pp. 170-178.

26. Lecat, M.A., "Probleme de La Reduction du Bruit Accustique Engendre par l'effect Couronne des Lignes Aeriennes Haute Tension", paper presented in 1972 CIGRE session.

27. Bear, J., Dynamics of Fluids in Porous Media, American Elsevier Publishing Co., New York, 1972, pp. 361-435.

28. Scheidegger, A.E., The Physics of Flow Through Porous Media, MacMillan Co., 1957, p. 68.

29. Batchelor, G.K., An Introduction to Fluid Dynamics, Cambridge University Press, Cambridge, England, 1970.

30. Bressler, R.G., and Wyatt, P.W., "Surface Wetting Through Capillary Grooves", Journal of Heat Transfer, Transactions of the ASME, Series C, Vol. 92, 1970, pp. 126-132.

31. Henderson, F.M., Open Channel Flow, The MacMillan Co., New York, 1966.

32. Baltaks, B.I., Diffusion in Semiconductors, Academic Press, Inc., 1963, pp. 94-96.

33. Rohsenow, W.M., Choi, H.Y., Heat, Mass and Momentum Transfer, Prentice-Hall, Inc., Englewood Cliffs, 1961.

34. Houghton, H.G., and Radford, S.H., "Microscopic Measurement of the Size of Natural Fog Particles", Papers in Phys. Oceanography and Meterology, Vol. VI, No. 4, November, 1938, p. 5.

35. Calvert, S., "Venturi and Other Atomizing Scrubbers-Efficiency and Pressure Drop", AICE Journal, Vol. 16, No. 3, May, 1970, pp. 392-396.

36. Van Horn, K.R., ed., Aluminum-Vol. III Fabrication and Finish, American Society for Metals, Ohio, 1967.

37. Peterson, A., Gross, E.E., Jr., Handbook of Noise Measurements, General Radio Co., West Concord, Mass., 1967.

38. Saums, H.L., Pendleton, W.W., Materials for Electrical Insulating and Dielectric Functions, Hayden Book Co., New Jersey, 1973.

39. Transmission Line Reference Book-345 kV and Above (Draft), Project UHV and AC Transmission Studies, General Electric Co.

BIOGRAPHICAL SKETCH

Born in Shanghai, China in 1947, the author immigrated with his family to the United States in 1959. He graduated summa cum laude from the University of Pennsylvania in 1968 and received the degree of Bachelor of Science in Electrical Engineering.

After working for a year in the Aerospace Instrument Business Section of General Electric Co. as a design engineer, he began graduate studies at the Massachusetts Institute of Technology where he received the Master Degree in 1971 and the Electrical Engineer Degree in 1972.

The author was coauthor in the following papers:

"Interferometric Density Measurements in the Arc of a Pulsed Plasma Thruster" by K.I. Thomassen and D. Tong, Journal of Spacecraft and Rockets, Vol. 10, No. 3, March 1973.

"Effects of Surface Wettability on Audible Noise and Capillary Absorption as a Noise Reduction Scheme" by D. Tong, G.L. Wilson, and I. Johansen, to presented in the 1975 IEEE Summer Power Meeting.

His professional interests are in applied physics research in power systems.